2019

Investigation Of Ferroelectric Perovskite Oxides For Photovoltaic Applications

Liyan Wu
University of Pennsylvania

Recommended Citation

Wu, Liyan, "Investigation Of Ferroelectric Perovskite Oxides For Photovoltaic Applications" (2019). *Publicly Accessible Penn Dissertations*. 3481.
https://repository.upenn.edu/edissertations/3481

Investigation Of Ferroelectric Perovskite Oxides For Photovoltaic Applications

Abstract

Ferroelectric materials have been demonstrated to be promising in developing emerging photovoltaic technologies because of the various mechanisms that allow above-bandgap photovoltages and higher efficiencies. However, the wide bandgaps of conventional ferroelectric oxides limit their utilization of the solar spectrum. This thesis focused on the identification of chemical substituents capable of reducing the bandgap of ferroelectric perovskite oxides, while retaining a robust polarization. Building upon the discovery of (1−x)KNbO3-xBa(Ni1/2Nb1/2)O2.75 solid solutions which have bandgaps compatible with traditional semiconductors, new families of Ni- and Ni/Nb-substituted BaTiO3 were fabricated through solid state methods. The oxygen vacancies accompanying the Ni and Ni-Nb substitutions significantly lower the optical bandgap of BaTiO3 to ~1.5 eV. Although effective in reducing the bandgap, the loss of the ferroelectric polarization in KNbO3 and BaTiO3 at relatively small concentrations (≤ ~10%) of Ni and Ni/Nb prevent access to a wide range of polar solid solutions. To mitigate this issue, bandgap reduction was explored in systems with a more robust ferroelectric order, namely the tetragonally-enhanced PbTiO3-BiFeO3 system where the A site is completely occupied by ferroelectrically active Pb/Bi cations. A morphotropic-phase-boundary (MPB) additive, Bi(Ni1/2Ti1/2)O3, was found to simultaneously lower the bandgap and retain the ferroelectric order of a wide range of compositions in the PbTiO3-BiFeO3-Bi(Ni1/2Ti1/2)O3 ternary system. MPB compositions showed a switchable photovoltaic effect with an open-circuit voltage (Voc) of 6 V. Under AM1.5G illumination the short-circuit photocurrent (jsc) of these systems increased by an order of magnitude as Eg was lowered from 2.85 to 2.25 eV. The dependence of the photovoltaic response on the ferroelectric polarization, device configuration, temperature and defects were investigated in 0.5PbTiO3-0.5Bi(Ni1/2Ti1/2)O3, a tetragonal composition close to the MPB. A direct correlation between the polarization and the photovoltaic response was established. The PV properties of 0.5PbTiO3-0.5Bi(Ni1/2Ti1/2)O3 showed strong temperature dependence with Voc increasing and jsc decreasing at lower temperature; a Voc above 100 V was obtained for a 250 μm thick sample below 160 K. Temperature dependent measurements of dielectric and mechanical responses showed the photovoltaic properties are influenced by thermal depolarization and a re-entrant relaxor phase transition, and are also mediated by the polaron hopping mechanism. Post-annealing in atmospheres with different pO2's allowed modification of the carrier concentration, which in turn was used to control the dielectric, mechanical and photovoltaic properties.

Degree Type

Dissertation

Degree Name

Doctor of Philosophy (PhD)

Graduate Group

Materials Science & Engineering

First Advisor

Peter K. Davies

Keywords

Ceramic, Ferroelectric, Perovskite oxide, Photovoltaic

Subject Categories

Mechanics of Materials

INVESTIGATION OF FERROELECTRIC PEROVSKITE OXIDES FOR PHOTOVOLTAIC APPLICATIONS

Liyan Wu

A DISSERTATION

in

Materials Science and Engineering

Presented to the Faculties of the University of Pennsylvania

in

Partial Fulfillment of the Requirements for the

Degree of Doctor of Philosophy

2019

Supervisor of Dissertation

____

Dr. Peter K. Davies, Professor, Materials Science and Engineering

Graduate Group Chairperson

____

Dr. I-Wei Chen, Professor, Materials Science and Engineering

Dissertation Committee

Dr. Cherie R. Kagan, Professor, Electrical and System Engineering

Dr. Andrew M. Rappe, Professor, Chemistry

Dr. Jonathan E. Spanier, Professor, Materials Science and Engineering, Drexel University

INVESTIGATION OF FERROELECTRIC PEROVKSITE OXIDES FOR PHOTOVOLATIC APPLICATIONS

To my parents for their endless love

ACKNOWLEDGMENT

This journey would not have been possible without the support and help from many people. Six years of Ph.D. student life seems intimidating, but every moment is memorable not because of my scientific achievement (if there is any) but the experience shared with my family, friends and colleagues.

I feel extremely grateful for pursuing my doctoral degree at the University of Pennsylvania, where I worked with the best scientists and mentors one could imagine. My deepest thanks go to my advisor, Professor Peter K. Davies, who does not only guide me throughout the highs and lows of this process, patiently and encouragingly, but also always inspires me as a role model. I am indebted to his wealth of knowledge and devotion to education.

I would also like to thank the committee members Prof. Cherie Kagan, Prof. Andrew Rappe and Prof. Jonathan Spanier for their valuable guidance and participation in this dissertation.

Special thanks go to the research group of Prof. Jonathan Spanier at Drexel, with whom I have collaborated on various projects. I had great experience closely working with all the current and many former members in the group. In particular, I would like to thank Andrew Bennett-Jackson for his great help on my whole research work; Anthony Ruffino for introducing me to the Raman measurement; Aleksandr Plokhikh for the XPS; Dr. Adrian Podpirka for helping me on photolithography and electrode fabrication; Drs. Andrew Akabeshev, Dominic Imbrenda, Matthias Falmbigl and Zongquan Gu for many useful discussions and giving me countless help.

I am also grateful to be part of the Penn MSE community. I would like to first thank Vicky Lee, Pat Overend and Irene Clements who make the department a warm and welcoming place. I am immensely grateful to Steve Szewczyk who devotes to help student with his expertise in engineering and maintains all kinds of equipment greatly. Without Steve, many of my experiments would not have been possible. I would also like to thank my amazing fellow MSE graduates and alumni whose talent and diligence always inspire me. Thanks go to Dr. Jian Han, Dr. Yanhao Dong and Zhurun Ji for many illuminating discussions and advice on research; Dr. Hye-Na Kim for encouraging me and giving me career advice; Dr. Mark Licurse for guiding me when I just joined the group.

I want to further express my gratitude to my friends Yuze Sun, Xi Yao, Junran Yang, Junyuan Feng, Jing Liu, Lucas Secco, Ya Xu, Zhe Liu and Dr. Gerui Liu who make Philadelphia a place I would call my second hometown. A big thank you to Yuze Sun and Xi Yao for throwing many unforgettable parties and cooking so many dinners for all of us.

At last, I would like to thank my family for the support and the joy you bring to me. Especially, I want to say thank you to Yimei Zhang for loving and believing in me.

ABSTRACT

INVESTIGATION OF FERROELECTRIC PEROVKSITE OXIDES FOR PHOTOVOLTAIC APPLICATIONS

Liyan Wu

Peter K. Davies

Ferroelectric materials have been demonstrated to be promising in developing emerging photovoltaic technologies because of the various mechanisms that allow above-bandgap photovoltages and higher efficiencies. However, the wide bandgaps of conventional ferroelectric oxides limit their utilization of the solar spectrum. This thesis focused on the identification of chemical substituents capable of reducing the bandgap of ferroelectric perovskite oxides, while retaining a robust polarization. Building upon the discovery of $(1-x)KNbO_3$-$xBa(Ni_{1/2}Nb_{1/2})O_{2.75}$ solid solutions which have bandgaps compatible with traditional semiconductors, new families of Ni- and Ni/Nb-substituted $BaTiO_3$ were fabricated through solid state methods. The oxygen vacancies accompanying the Ni and Ni-Nb substitutions significantly lower the optical bandgap of $BaTiO_3$ to ~1.5 eV. Although effective in reducing the bandgap, the loss of the ferroelectric polarization in $KNbO_3$ and $BaTiO_3$ at relatively small concentrations (≤ ~10%) of Ni and Ni/Nb prevent access to a wide range of polar solid solutions. To mitigate this issue, bandgap reduction was explored in systems with a more robust ferroelectric order, namely the tetragonally-enhanced $PbTiO_3$-$BiFeO_3$ system where the *A* site is completely occupied by ferroelectrically active

Pb/Bi cations. A morphotropic-phase-boundary (MPB) additive, $Bi(Ni_{1/2}Ti_{1/2})O_3$, was found to simultaneously lower the bandgap and retain the ferroelectric order of a wide range of compositions in the $PbTiO_3$-$BiFeO_3$-$Bi(Ni_{1/2}Ti_{1/2})O_3$ ternary system. MPB compositions showed a switchable photovoltaic effect with an open-circuit voltage (V_{oc}) of 6 V. Under AM1.5G illumination the short-circuit photocurrent (j_{sc}) of these systems increased by an order of magnitude as E_{g} was lowered from 2.85 to 2.25 eV. The dependence of the photovoltaic response on the ferroelectric polarization, device configuration, temperature and defects were investigated in $0.5PbTiO_3$-$0.5Bi(Ni_{1/2}Ti_{1/2})O_3$, a tetragonal composition close to the MPB. A direct correlation between the polarization and the photovoltaic response was established. The PV properties of $0.5PbTiO_3$-$0.5Bi(Ni_{1/2}Ti_{1/2})O_3$ showed strong temperature dependence with V_{oc} increasing and j_{sc} decreasing at lower temperature; a V_{oc} above 100 V was obtained for a 250 µm thick sample below 160 K. Temperature dependent measurements of dielectric and mechanical responses showed the photovoltaic properties are influenced by thermal depolarization and a re-entrant relaxor phase transition, and are also mediated by the polaron hopping mechanism. Post-annealing in atmospheres with different pO_2's allowed modification of the carrier concentration, which in turn was used to control the dielectric, mechanical and photovoltaic properties.

TABLE OF CONTENTS

LIST OF TABLES

LIST OF ILLUSTRATIONS

Chapter 1 Introduction

1.1 Motivation: Ferroelectric Materials for Solar Energy Conversion

Access to sustainable and clean energy sources has been a long-standing challenge to human society since the industrial revolution. Global energy consumption has tripled in the last half century and is projected to increase by 27% from 2017 to 2040.[1] According to the International Energy Agency, fossil fuels such as coal, gas and oil contribute to 80% of the global energy demand and are responsible for the record high of 33.1 billion metric tons of CO_2 emissions in 2018.[2] Innovation and technology developments are essential for increased efficiency and a transition to renewable sources of energy.

Solar energy from the radiation of the sun is a sustainable and clean energy source which can be directly converted into usable electric power through the photovoltaic (PV) effect. Since the first application of semiconductor based photovoltaic solar cells in satellites in the 1950s, fundamental and applied research and development has dramatically reduced their cost and for many applications they are now the most economical power supply.[3] However, the theoretical limit of efficiency in conventional photovoltaic solar cells and the high environmental impact from traditional semiconductor manufacturing still limit their share in the current energy supply market. More opportunities may lie in emerging photovoltaic technologies and low-cost manufacturing techniques such as hybrid perovskite cells where rapid increases of power conversion efficiency from single digit to a certified 24.2% have been achieved within the last six years.[4]

PV technologies that rely on charge carrier separation at PN junctions or other semiconductor interfaces are subject to the Shockley-Queisser limit which takes into account the spectrum losses, recombination, and black body radiation.[5] For silicon, this limit is ~32%, far from an effective utilization of the solar energy. However, for crystals that lack inversion symmetry, there is an alternate PV mechanism which, in contrast to PN junctions, does not require internal electric fields.[6] This mechanism originates from the breaking of inversion symmetry and because it is effective throughout the entire crystal, is named as the “bulk photovoltaic effect” (BPVE). The potential advantages of BPVE-based solar cells include above-bandgap open-circuit voltages that surpass the Shockley-Queisser limit and a simplified device architecture that allows for a cost-effective fabrication process. Ferroelectric materials, which have polar crystal structures, show BPVE responses under unpolarized light[7] and can also induce conventional PV carrier generation from the polarization-induced electric fields at domain walls, grain boundaries, and electrode interfaces.[8] High efficiency solar energy conversion is therefore feasible in ferroelectric materials if the combination of BPVE and conventional PV effects can be engineered to work in a synergistic way.

Although theoretically promising, many obstacles remain in fabricating a ferroelectric PV material with a performance capable of matching a conventional semiconductor solar cell. A key challenge, and the motivation for this thesis, is the engineering of ferroelectric materials with bandgaps suited to the solar spectrum. The tuning of the bandgap in these systems could potentially be approached through chemical alloying, quantum size effects, and/or lattice mismatch or superlattice formation; however, the alteration of the gap must be achieved without the loss of the bulk ferroelectric response. This dissertation focuses on schemes for engineering the bandgaps of ferroelectric perovskite oxides through chemical substitution and evaluation of the PV performance of the resultant ceramic alloys. The successful identification of effective bandgap lowering strategies for bulk ceramics also provides a platform for optimization of their PV performance in thin film or single crystal configurations.

1.2 A Brief Overview of Photovoltaic Response in Ferroelectric Materials

1.2.1 Conventional PV Effect

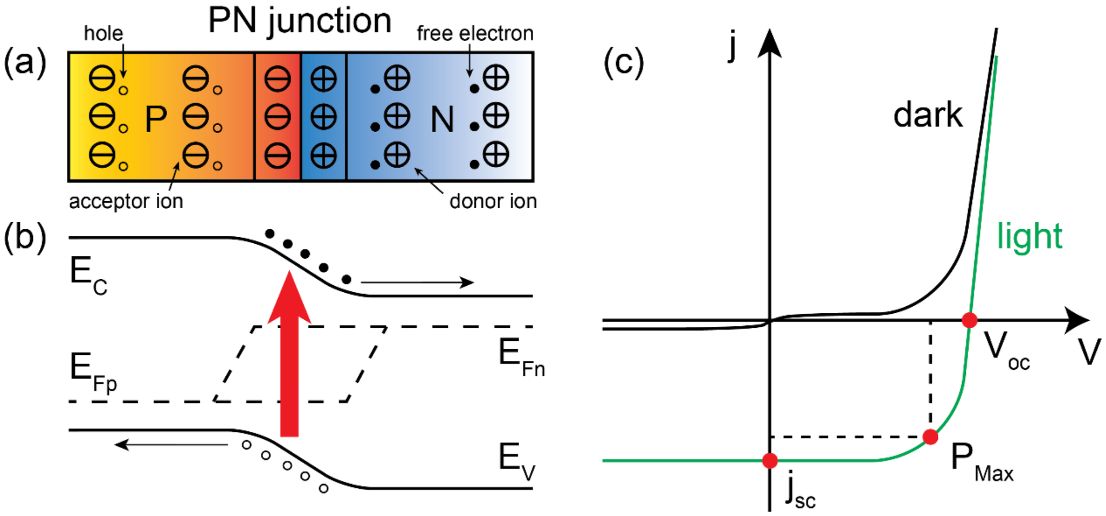

Figure 1.1 Schematics of the PV mechanism in a PN junction. (a) A PN junction diode. (b) Band diagram of a PN junction under illumination. (c) Typical *IV* characteristics of the PN junction in the dark and under light.

The conventional PV effect requires an internal electric field to separate the photogenerated charge carriers. This internal electric field can result from the doping of different regions, contacts or surfaces. The mechanism of the internal electric field effect can be illustrated by a typical PN junction diode shown in **Figure 1.1**. At equilibrium, a depletion region is formed at the interface where free electrons from the N type side diffuse across the junction filling the holes in the P type region. The immobile ions left at the interface induce a built-in electric field which bends the energy bands. Under above-bandgap illumination, the electrons are promoted to the conduction band, leaving holes in the valence band; the carriers generated at the interface are further separated by the built-in electric field and eventually flow into the external circuit. The carrier generation from the absorbing photons changes the equilibrium population of the electrons and holes, leading to a splitting of the Fermi level into electron and hole quasi-Fermi levels (i.e. E_{Fn} and E_{Fp} respectively). The open-circuit voltage V_{oc} of a PN junction solar cell is given by the difference of E_{Fn} and E_{Fp}, which is limited by the bandgap of the semiconductor absorber. The typical *IV* response of a PN junction exhibits diode-like behavior in the dark and under illumination as shown in **Figure 1.1**c. The maximum power P_{max} can be expressed as $P_{\mathrm{max}} = j_{\mathrm{sc}} \times V_{\mathrm{oc}} \times FF$, where FF is the fill factor of the solar cell. This working principle of the PV effect also applies to metal-semiconductor contacts (i.e. Schottky barriers) in which the built-in electric field originates from the different work functions of the semiconductor and the metal contact.

1.2.2 PV Effects in Ferroelectrics

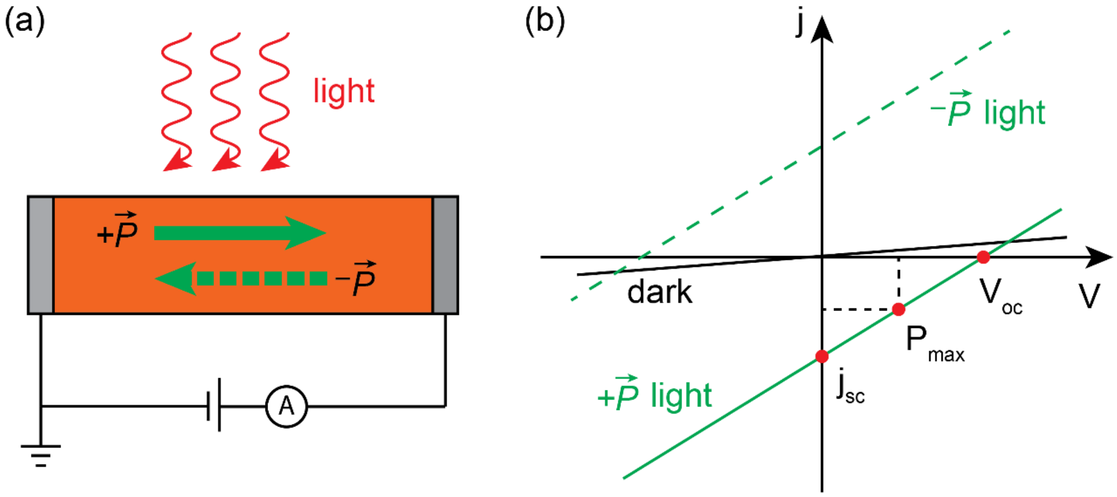

Figure 1.2 Schematics of PV effect in ferroelectric materials. (a) Ferroelectric crystal with two possible polarization states opposite to each other. (b) Typical *IV* characteristics of ferroelectric crystal in the dark and under light.

- Phenomenology

Regardless of the microscopic mechanisms, the experimentally observed PV responses of ferroelectric materials share several common features. The ideal set-up for measurement of the PV response of a single-phase bulk ferroelectric material (monodomain crystal or a poled ceramic) typically comprises a device configuration with symmetrical electrodes, **Figure 1.2**a. The ferroelectric layer has two polarization states ($+\vec{P}$ and $-\vec{P}$ as indicated by the green arrows) which can be switched by applying an external field. The *IV* response is normally collected along the direction of the ferroelectric polarization, $\vec{P}$, with illumination on the sample surface. In contrast to the diode-like behavior of PN junctions, the typical *IV* response of a ferroelectric material is linear, **Figure 1.2**b, and often described by the following relation

$$j = j_{\mathrm{sc}} - \frac{V}{L}\left(\sigma_{\mathrm{d}} + \sigma_{\mathrm{ph}}\right)$$

where L is the sample thickness, and σ_{d} and σ_{ph} are the dark and photo conductivities respectively. The PV effect in ferroelectric materials also shows polarity in accordance with the ferroelectric polarization with the sign of the photovoltage (and current) being reversed when the direction of $\vec{P}$ is switched.

The V_{oc} of ferroelectric materials is not limited by the magnitude of the bandgap and scales linearly with the sample thickness. Observations of high V_{oc} have been reported in several bulk and thin film ferroelectric materials.[9–16] The magnitude of the photovoltaic current (experimentally measured as j_{sc}) is typically linearly dependent on the light intensity and therefore on the photogeneration rate.[17–19] The photovoltaic currents in ferroelectrics also show tensorial properties and are sinusoidally dependent on the light polarization angle, especially for single crystals and thin films with preferred orientations.[12,19–22] The tensor relation of j_{sc} can be expressed as

$$j_{sc-i} = G_{ijk} e_j e_i^* I$$

where e_j and e_j are components of the light polarization vector; G_{ijk} is the BPVE tensor, and I is the incident light intensity.[23] These features are not always observed in one material due to the BPVE's superposition with other PV effects and its susceptibility to defects and sample microstructures.

- Microscopic Models

A PV response with a linear *IV* and an above-bandgap V_{oc} is generally referred to as a “BPVE” regardless of the actual microscopic mechanism. Two types of mechanisms are used to describe the BPVE in ferroelectric materials. The first is the “shift current mechanism”, a nonlinear optical process taking into account the nondiagonal element of the density matrix. The shift current originates from the coherent evolution of the electron and hole wavefunctions and can be interpreted as the shift of electron positions in real space following the carrier inter-band transitions.[7,23–25] This mechanism is a hot carrier effect that does not require a built-in electric field, therefore the energy dissipation of carrier thermalization can be avoided. The second mechanism is the ballistic current which arises from the asymmetric momentum distribution of the non-thermalized photogenerated carriers in the conduction band, illustrated in **Figure 1.3**.[26,27] For a centrosymmetric crystal, the photogenerated carriers have a symmetric distribution of momenta, leading to zero net current. However, in a non-centrosymmetric crystal, optical transitions of both impurity to band or band to band (see **Figure 1.3**b) result in an imbalance of carriers moving in one direction before relaxation to the band bottom over a free path l_0. In $BaTiO_3$ single crystals, the magnitude of l_0 is estimated to lie in the range of 10 to 100 nm.[17] In contrast to the shift current, ballistic currents involve a transport mechanism which allows the observation of a Hall effect. Recent experiments have been conducted to separate the shift and ballistic currents from the observed overall BPVE current through a photo-Hall measurement or the ultrafast terahertz emission spectroscopy.[28,29]

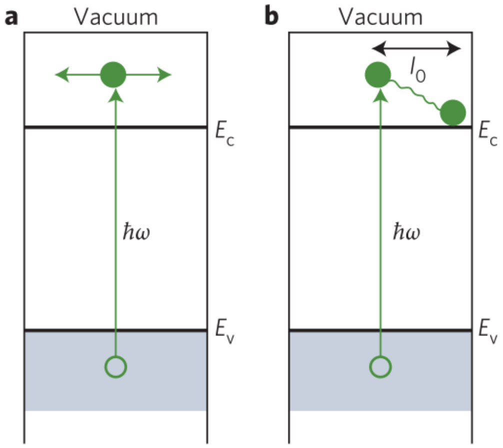

Figure 1.3 Schematic of photoexitation process in (a) centrosymmetric crystal and (b) non-centrosymmetric crystal. [Adapted by permission from reference [26]. Copyright 2016 Springer Nature].

- Domain wall (DW) models and other interfacial effects

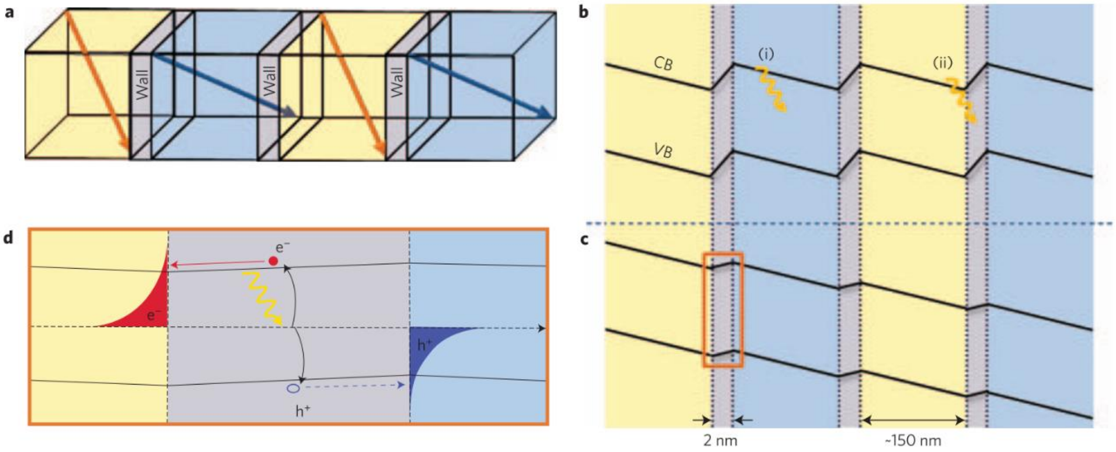

Figure 1.4 Schematic illustration of domain wall model for above-bandgap open-circuit voltage in epitaxial BiFeO$_3$ films. (a) 71° domain wall configuration. (b) Corresponding band diagram showing the valence band and conduction band across these domains and domain walls in the dark. (c) Evolution of band structure upon illumination of the domain wall array. (d) Detailed picture of the build-up of photo excited charges at a domain wall. [Adapted by permission from reference [9]. Copyright 2009 Springer Nature].

To understand the frequently observed above-bandgap V_{oc} in ferroelectric materials, another model, based on a study of epitaxial $BiFeO_3$ thin films with periodic domain structures, was proposed involving the role of domain walls (DW). The DW model is analogous to a multijunction tandem solar cell where the photovoltages of each junction are additive with an above-bandgap V_{oc} being obtained across the entire device. In epitaxial $BiFeO_3$ films 71° and 109° domain walls, where the polarization discontinuity causes electrostatic potential steps, induce strong electric fields that can separate the photogenerated charge carriers over the narrow DW region, see **Figure 1.4**. The above-bandgap V_{oc} was only observed when the electrodes were parallel to the DWs and was not detected for perpendicular electrode configurations.[9] However, subsequent investigations revealed that at sufficiently low temperatures an above-bandgap V_{oc} could be observed in $BiFeO_3$ epitaxial films regardless of the DW and electrode configurations, emphasizing again the role of the BPVE.[12,20] In more recent studies, the role of DWs and BPVE were reconciled by quantifying the contribution from each effect in $BiFeO_3$ thin films and $BaTiO_3$ single crystals and the effect of the DWs superimposed on the BPVE were found to significantly enhance the overall PV responses.[21,30]

Other PV mechanisms that are driven by the internal electric fields are also present in ferroelectric systems. For example, the formation of Schottky barriers at the electrode-ferroelectric contacts have been found to enhance the overall PV performance,[31] and depolarization fields from the unscreened charges at the surface of the ferroelectric can also facilitate charge carrier separation.[32,33] Very recently it was shown the BPVE can also be enhanced by using nanoscale electrode geometries, which enable strong local electric fields at the interface to help collect the hot carriers of ballistic currents.[13,26] By judicious selection of electrode materials and geometries, further enhancements of the overall PV performance in ferroelectric materials can be expected.

This thesis focuses on the PV responses of ferroelectric ceramics with the goal of improving the V_{oc} and j_{sc} through engineering the bandgaps and polarizations of perovskite oxides. Ferroelectric ceramics are more complex compared to single crystals and epitaxial films due to the presence of grain boundaries and the randomness of the grain (and domain boundary) orientations. Therefore, quantitative analyses of contributions from the different PV mechanisms is challenging and has led to many different, and inconsistent, reports on the working mechanisms of the observed PV effects in ceramic ferroelectric systems.[14,16,31,34–37]

1.3 A Brief Overview of Ferroelectric Perovskite Oxides

1.3.1 General ABO_3 Perovskite Structure

Perovskite oxides with a general chemical formula ABO_3, where A and B represent metal cations, have been the focus of numerous fundamental and applied investigations. This structure offers a broad platform for the survey of chemistry, structure and property relationships and finds applications in a wide range of electronic and optical devices. The importance is associated with the chemical and structural flexibility of the ABO_3 structure and the corresponding wealth of resultant properties. It is well-known perovskites can accommodate over 90% of the natural metallic elements in the periodic table.[38] Co-substitutions of one or more elements on the A and/or B sites further broaden the spectrum of perovskite isomorphs and resultant properties.

The ideal structure of a perovskite oxide can be represented as a simple cubic structure with large A-cations at the corners of the unit cell, a small B-cation at the center and the oxygen anions occupying the face-centered positions as illustrated in **Figure 1.5**a. However, the real structures of most perovskites deviate from the ideal simple cubic cells by adopting lower symmetries induced through rotations/tilts and/or distortions of the BO_6 oxygen octahedra. The Goldschmidt tolerance factor, a simple chemical descriptor for perovskite stability, is defined by

$$t = \frac{r_{\mathrm{A}} + r_{\mathrm{O}}}{\sqrt{2} \times (r_{\mathrm{B}} + r_{\mathrm{O}})}$$

where r_{A}, r_{B}, and r_{O} are the radii of 12-coordinate A cation, 6-coordinate B cation, and 6-coordinate O^{2-} respectively. For $t \approx 1$, the ideal cubic structure is adopted as exemplified by $SrTiO_3$ (**Figure 1.5**c); for $t < 1$, orthorhombic or rhombohedral structures are formed depending on the oxygen octahedral rotation patterns (the example of orthorhombic $CaTiO_3$ is shown in **Figure 1.5**b); for $t > 1$, tetragonal or hexagonal structures can be stabilized (the example of tetragonal $PbTiO_3$ shown in **Figure 1.5**d). Some of these lowered symmetries enable the formation of polar structures such as tetragonal $PbTiO_3$, rhombohedral $BiFeO_3$ and orthorhombic $KNbO_3$ which are among the most common ferroelectric materials. Solid solutions formed between polar/polar or polar/non-polar structures can also exhibit a so called “morphotropic phase boundary” (MPB) at which the ferroelectric and piezoelectric properties are greatly enhanced.

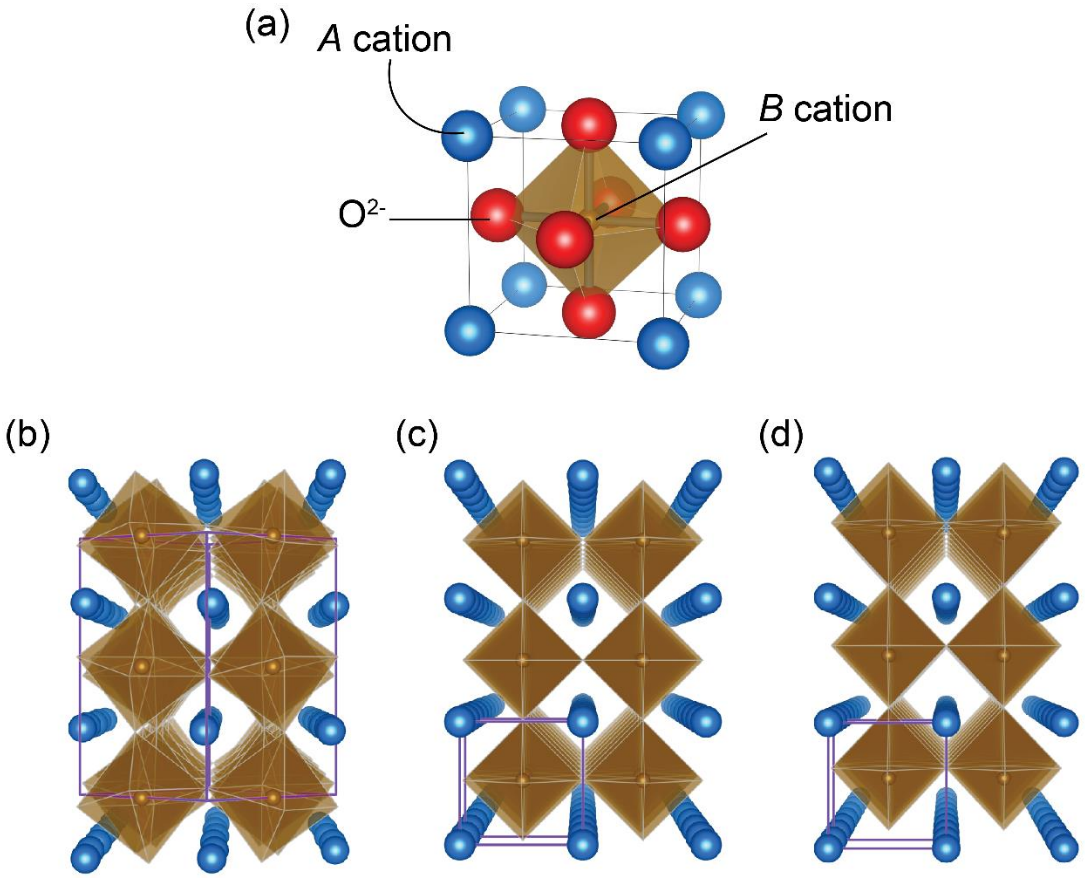

Figure 1.5 Typical crystal structures of perovskite oxides. (a) Ideal cubic perovskite unit cell. (b) $CaTiO_3$ structure: $t < 1$; orthorhombic. (c) $SrTiO_3$ structure: $t = 1$; cubic. (d) $PbTiO_3$ structure: $t > 1$; tetragonal. (oxygen anions were omitted for clarity in b, c, and d; the purple line represents the unit cell)

1.3.2 Ferroelectricity

Ferroelectric materials are characterized by their switchable spontaneous polarization which enables important technological applications such as dielectric capacitors, piezoelectric sensors/actuators, and ferroelectric random-access memories.[39] As described in the previous section, certain structural distortions in perovskite oxides can lead to polar correlations and ferroelectricity. Indeed, perovskite oxides contribute almost all of the known technologically important ferroelectric compounds.[39] Some of the atomistic mechanisms responsible for stabilizing ferroelectric order are as follows:

- Second-order Jahn-Teller distortion (SOJT)

The most common origin of ferroelectricity in perovskite oxides is due to collective ionic displacements driven by off-centering of the A and/or B site cations via a SOJT effect. This effect is associated with the movement of cation species with d^0 configuration on the B site (e.g. Ti^{4+}, Nb^{5+}, Ta^{5+}) and/or $6s^2$ lone-pair configuration on the A site (e.g. Pb^{2+}, Bi^{3+}), which form strong covalent bonds with the surrounding oxygen anions. Examples include B-site driven ferroelectric $BaTiO_3$ and $KNbO_3$, A-site driven $BiFeO_3$ and $BiMnO_3$,[40] and $PbTiO_3$ and $Bi(Zn_{1/2}Ti_{1/2})O_3$ where both the A-site and B-site cations are capable of off-centering. Although these SOJT active ferroelectric perovskites have large polarizations, they typically also have wide bandgaps (3-5 eV). The ferroelectric response is very sensitive to the introduction of bandgap-changing d^n substituents and the loss of the collective polarization at relatively small levels of doping provides a major challenge in adopting these systems for application as solar PV materials.

- Mechanisms of ferroelectricity in multiferroics

The strict chemical requirements for conventional ferroelectrics also limit the formation of simultaneous magnetic order, systems which are termed “multiferroic”. This research area has attracted considerable attention due to the potential applications of devices that involve a coupling of the ferroelectric and magnetic response and has resulted in the identification of new mechanisms for supporting ferroelectricity. Examples include "geometric ferroelectricity" which is typically found in hexagonal manganites (*e.g.* $YMnO_3$) and is driven by the titling of MnO_5 polyhedra;[41] ferroelectricity driven by "spiral magnetic ordering" (*e.g.* $TbMnO_3$);[42] "hybrid improper ferroelectricity" where the polarization can arise from the coupling of two nonpolar BO_6 rotation modes (*e.g.* Ruddlesden-Popper phases);[43,44] and "charge ordering induced ferroelectricity" (*e.g.* $(Pr,Ca)MnO_3$).[45] It is possible these novel mechanisms of ferroelectric ordering could also offer new approaches for the design of narrow bandgap ferroelectric oxides.

1.3.3 Bandgap Engineering of Ferroelectric Perovskite Oxides

For practical photovoltaic applications, ferroelectric materials must have bandgaps compatible with the solar spectrum. The optimal bandgap for PN junction based solar cells is around 1.3 eV according to the calculated maximum efficiency from the Shockley-Queisser limit; ferroelectric materials should have similar values regardless of the PV mechanisms or even narrower bandgaps if hot carriers could be collected. A sizable polarization is also desirable for manipulating the polarity of the BPVE and enhancing the interfacial electric fields. Therefore, systems with a tunable and narrow E_g and a large remnant polarization (P_r) are of interest in providing a platform for and understanding and harnessing the BPVE.

As mentioned in the previous section, conventional ferroelectrics have wide bandgaps, with one exception, $BiFeO_3$, where the relatively low E_g (2.7 eV) has stimulated many studies of its application as a photovoltaic. Several efforts have been made to tailor the properties of other ferroelectric oxides for PV applications by lowering their bandgaps through chemical substitution[16,46–49] and/or introducing cation ordering.[50–53] A summary of the literature data for these systems is provided in **Table 1-1** and the observed P_r is plotted with respect to the E_g in **Figure 1.6**. Multiferroic oxides such as hexagonal manganites/ferrites[54–56] and the non-perovskite phase $KBiFe_2O_5$[10,57] have also been shown to have bandgaps suited to photovoltaic applications; however, the polarization of those systems is quite small (≤ 5 μC/cm^2).[41,58] Most systems show a clear empirical trend of a reduction in P_r with the narrowing of E_g (see the enclosed region in **Figure 1.6**). Although $Bi_4Ti_3O_{12}$-$LaCoO_3$ superlattices and $PbTiO_3$-$Bi(Ni_{2/3}Nb_{1/3})O_3$ solid solutions are examples where a substantial polarization (15 and 33 μC/cm^2 respectively) is retained, the chemical substitution only produces a very limited reduction in E_g.[16,47] The ability to induce a continuous variation in E_g, while retaining a bulk polarization, is also important in designing multilayer solar cells that could utilize the entire solar spectrum; this has been successfully achieved in $Bi(Fe_{1/2}Cr_{1/2})O_3$ epitaxial thin films through processing-induced B-site ordering.[51] However, the P_r in this system also drops significantly, from 45 to 5 μC/cm^2, as the E_g is reduced.

Table 1-1 Literature data of ferroelectric oxides studied for photovoltaic application (s.c. = single crystal, t.f. = thin film, b.c. = bulk ceramic)

	E_g (eV)	P_r (μC/cm^2)	E_g tunability (eV)	T_C (K)	Thin film or bulk	Structure	Ref.
$BiFeO_3$	2.7	60	N/A	1100	s.c. and t.f.	Rhmb. prvsk.	[59], [60], [61], [62]
$LiNbO_3$	3.78	71	N/A	1483	s.c.	$LiNbO_3$-type	[63]
$KBiFe_2O_5$	1.6	3.73	N/A	780	s.c.	Brownmillerite phase	[10],[57]
$BaTiO_3$	3.3	25	N/A	400	s.c. and t.f.	Tetra. prvsk.	[17], [28],[33]
La-doped $BiFeO_3$ (La-BF)	2.32	60	N/A	713	t.f.	Rhmb. prvsk.	[64]
$Bi(Fe_{1-x}Co_xO)_3$ (Co-BF)	2.3	60	0.4	N/A	t.f.	Rhmb. prvsk.	[65]
$Bi_{0.925}Sm_{0.075}Fe_{0.95}Co_{0.05}O_3$ (Sm,Co-BF)	2.27	60	N/A	N/A	t.f.	Tetra. prvsk.	[66]
$Bi_4Ti_3O_{12}$-$LaCoO_3$ superlattice (BiT-LC)	2.65-3.55	15	0.9	N/A	t.f.	Aurivillius phase	[47]
$Bi_5FeTi_3O_{15}$	2.68	10-15	N/A	1030	t.f.	Aurivillius phase	[67]
$Bi(Fe_{1/2}Cr_{1/2})O_3$ (BFCO)	1.4-2.3	5 - 45	0.9	N/A	t.f.	Double prvsk.	[51]
(Co,Fe)-doped $Bi_{3.25}La_{0.75}Ti_3O_{12}$ (BLCFT)	2.48	2.6	N/A	N/A	t.f.	Aurivillius phase	[68]
$LuMnO_3$	1.55	5	N/A	N/A	t.f.	Hexagonal manganite	[54]
$YbFeO_3$	2	4	N/A	N/A	t.f.	Hexagonal ferrites	[56]
$(Pb_{0.97}La_{0.03})(Zr_{0.52}Ti_{0.48})O_3$ (PLZT3/52/48)	3.4	35-45	N/A	N/A	b.c.	Tetra. prvsk.	[31],[69]
$Ba_{1-x}(Bi_{0.5}Li_{0.5})_xTiO_3$ (BBLT)	3.2	8	N/A	352	b.c.	Tetra. prvsk.	[70]
$0.9BaTiO_3$-$0.1Ba(Ni_{1/2}Nb_{1/2})O_{3-\delta}$ (BTNN)	1.5	4	N/A	N/A	b.c.	Tetra. prvsk.	[49]
$BaTi_{0.925}(Mn_{1/2}Nb_{1/2})_{0.075}O_3$ (BTMN)	1.66	15	N/A	345	b.c.	Tetra. prvsk.	[71]
$(1-x)KNbO_3$-$xBa(Ni_{1/2}Nb_{1/2})O_{3-\delta}$ (KBNN)	1.1-3.8	0-5 (at 77K)	2.7	736	b.c.	Orth. prvsk.	[46],[72]
$PbTiO_3$-$Bi(Ni_{2/3+x}Nb_{1/3-x})O_{3-\delta}$ (PT-BNN)	2.9-3.0	33	0.1	533	b.c.	Tetra. prvsk.	[16]
$(1-x)(Na_{1/2}K_{1/2})NbO_3$-$xBa(Ni_{1/2}Nb_{1/2})O_{3-\delta}$ (KNBNN)	1.50-1.63	0-11	0.13	N/A	b.c.	Orth. prvsk.	[73]
$Sr_{1-x}Bi_{2+x}Nb_{2-x}Ni_xO_{9-x}$ (SBNN)	2.25-2.7	1.1-2.7	0.45	N/A	b.c	Aurivillius phase	[48]

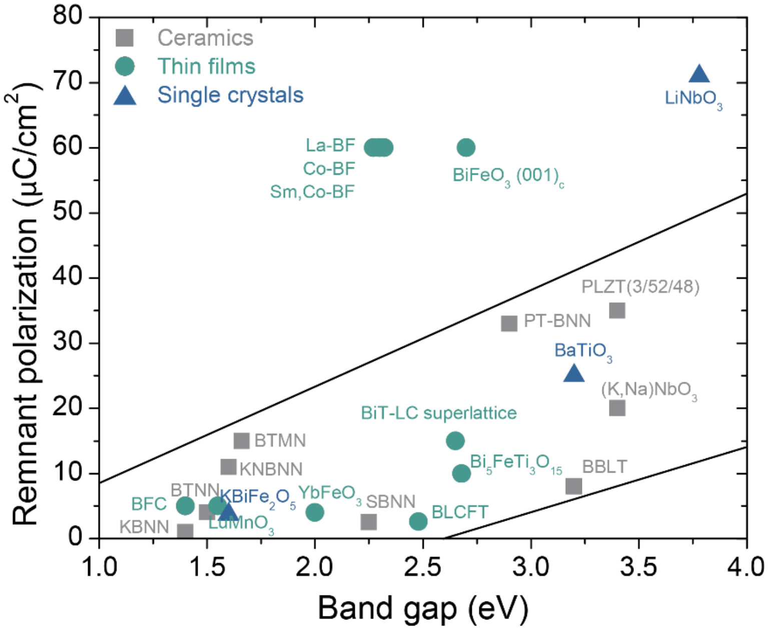

Figure 1.6 Summary of experimentally measured bandgaps and remanent polarization of ferroelectric oxides designed for photovoltaic applications. References are summarized in **Table 1-1**

1.4 This Dissertation

The aims of this dissertation are two-fold: (a) to identify chemical substituents capable of reducing and tuning the bandgap of ferroelectric perovskite oxides, while retaining a robust polarization; (b) to understand the dependence of the PV response of ceramic ferroelectrics on their polarization, device configuration, temperature and defects. The research builds upon the discovery of a significant reduction in the bandgap of a conventional ferroelectric oxide, $KNbO_3$, through the chemical substitution of a Ni^{2+} containing end-member, $Ba(Ni_{1/2}Nb_{1/2})O_{3-\delta}$.[46] The E_g values (1.4-1.6 eV, **Table 1-1**) of the resultant ferroelectric "KBNNO" solid solutions were comparable to traditional semiconductors; however, their P_r values are significantly inferior to the undoped end-member due to the replacement of the ferroelectrically active d^0 cations by the inactive

Ni^{2+} cations.[49] As a Masters student at Penn I participated in that study by fabricating some of the samples of KBNNO; that work is *not* included in this thesis. My Ph.D. research began by optimizing the synthesis techniques and studying the phase stability and dielectric properties of KBNNO, work that contributed to the final stages of the study published in reference [46]. The rationale for the investigation of KBNNO and the studies made as part of my Ph.D. dissertation are described in Chapter 3.

Guided by the results for KBNNO and first principles calculations conducted in Professor Rappe's group (Department of Chemistry, UPenn), attempts were also made to lower the bandgap of the titanate ferroelectric, $BaTiO_3$, through a combination of Ni^{2+} B-site substitutions and the introduction of oxygen vacancies. The phase stabilities, optical absorption, and dielectric/ferroelectric properties of these systems are explored in Chapter 4.

Chapter 5 describes a different approach to the formation of low E_g / high P_r materials through the chemical modification of tetragonally-enhanced $PbTiO_3$-$BiFeO_3$ with an MPB-forming additive, $Bi(Ni_{1/2}Ti_{1/2})O_3$, to simultaneously lower the bandgap and retain the ferroelectric order. The complete occupancy of the A-site by ferroelectrically active Pb/Bi cations increased the tolerance of the long-range polarization to the d^n transition metal substitution and enabled the formation of an extensive range of reduced bandgap, high P_r materials. The phase stability, optical and ferroelectric properties of this ternary system were mapped and the PV performance of selected MPB compositions with narrow E_g and large P_r are explored in detail.

In Chapter 6, correlations are established between the PV response and the ferroelectric-polarization switching and retention in MPB compositions of $PbTiO_3$-$Bi(Ni_{1/2}Ti_{1/2})O_3$. The PV properties could be altered by changing the polarization, device configuration, temperature and oxygen vacancy concentration. The temperature dependence of the dielectric, mechanical and photoconduction properties of tetragonal $0.5PbTiO_3$-$0.5Bi(Ni_{1/3}Ti_{1/2})O_3$ was related to a low temperature relaxor phase transition and mediated by small changes in the defect chemistry induced through annealing under controlled oxygen pressures.

The dissertation concludes in Chapter 7 by summarizing the important results of the previous chapters, suggesting future studies to improve the understanding of PV effects in ferroelectric systems, and proposing alternative avenues for the discovery of new narrow bandgap ferroelectric oxides.

Chapter 2 Experimental Methods

This chapter provides general overview of the experimental methods used throughout the dissertation. Additional details on the specific details of the techniques employed for the different chemical systems are given in each individual chapter.

2.1 Sample Synthesis

All of the materials were prepared by conventional solid-state synthesis methods using the starting carbonate and oxide powders listed in **Table 2-1**. All reactants were dried for 24 hours at the indicated temperatures and then stored in a desiccator before weighing, except K_2CO_3 which was kept at 300 °C until being used. Stoichiometric amounts of the starting reactants were weighed according to the target compositions and mixed by ball milling for 6 hours in ethanol with yttria-stabilized zirconia grinding media (Inframat Advanced Materials). After drying, depending on the specific system, the mixtures were calcined on platinum foil in an alumina crucible at temperatures ranging from 650 °C to 1100 °C, which are specified in the corresponding chapters. Multiple firings with intermediate grinding were typically required to promote homogeneity prior to final sintering. For subsequent characterization measurements, the calcined powders were pressed into 3-mm thick, 8-mm diameter or 5-mm thick, 25-mm diameter pellets in a uniaxial press at 50000 psi. For sintering, the green bodies were placed in a platinum crucible and surrounded by sacrificial powders of the same composition to prevent volatilization of K, Na, Pb or Bi. The actual sintering temperatures and times are described in each chapter. The sintered pellets were cut into slices using a diamond saw or crushed into a powder, depending on the characterization method being used.

Table 2-1 Reactants used in the synthesis of materials investigated in this work

Reactant	Supplier and Grade	Drying Temperature
K_2CO_3	J.T. Baker, 100.2%	Kept at 300 °C before weighing
Na_2CO_3	J.T. Baker, 99.8%	450 °C
$BaCO_3$	Cerac, 99.9%	450 °C
PbO	Alfa Aesar, 99.999%	550 °C
Bi_2O_3	Alfa Aesar, 99.9995%	550 °C
Nb_2O_5	Cerac, 99.95%	800 °C
NiO	Alfa Aesar, 99.998%	450 °C
TiO_2	Alfa Aesar, 99.995%	450 °C
Fe_2O_3	Alfa Aesar, 99.998%	800 °C

2.2 Sample Characterization

2.2.1 Powder X-ray Diffraction (XRD)

XRD was used to determine the phase content and structure of the powder and pellet samples. XRD patterns were collected on an X-ray diffractometer (Rigaku GiegerFlex D/Max-B) using Cu Kα radiation generated at 45 kV and 30 mA. Data obtained at a slow scan speed of 0.2° min^{-1} and a step size of 0.01° was used for calculating lattice parameters and revealing small peaks induced by B-site ordering. Si powder was used as an internal standard for the calibration of the peak positions.

2.2.2 Microstructures

The microstructures of selected compositions were examined using a scanning electron microscope (SEM, Quanta 600, FEI) equipped with an energy-dispersive X-ray spectrometer (EDS), and an optical microscope (Olympus BH-2 BF/DF/DIC/Pol).

2.2.3 UV-vis Diffuse Reflectance Spectroscopy (DRS)

The optical absorption properties of powder samples were characterized by UV-vis DRS. Diffuse reflectance measurements of fine powders are considered more accurate than transmission measurements in characterizing the optical absorption of solid samples when transparent single crystals or free-standing ultra-thin ceramic lamellae are unavailable. The DRS of powder samples were collected using a powdered MgO standard on a Cary 5000 UV-vis spectrophotometer equipped with a “Praying Mantis” diffuse reflectance accessory (Harrick Scientific Products Inc.) in Prof. Kagan’s laboratory (Department of Electrical and System Engineering, UPenn). The measured reflectance was transformed to absorption spectra according to the Kubelka-Munk (K-M) function defined as:

$$\mathrm{F}(R) = \frac{(1-R)^2}{2R}$$

where R is the reflectance. The optical transitions were modeled through Tauc’s law:

$$\alpha h\nu = A(h\nu - E_{\mathrm{g}})^n$$

where α = absorption coefficient, $h\nu$ = photon energy, A is a scaling constant, and n represents the transition type (n = ½ for direct transition and 2 for indirect transition). In DRS, α is replaced by the K-M function F(R). The corresponding direct and indirect optical gaps E_g were obtained by extrapolation of the linear region for $[\mathrm{F}(R)h\nu]^{\frac{1}{n}}$ to the photon energy axis.

The morphology of the samples was controlled by hand grinding the powders in a mortar under ethanol and then drying at 120 °C for 30 mins before the measurement. The validity and accuracy of using the K-M function and Tauc plots was confirmed by comparing the DRS obtained from powder samples of known materials to the absorption coefficients of their single crystals in the literature. For example, the profiles of F(R) for green NiO and $BiFeO_3$ powders in **Figure 2.1**a and b are both consistent with their reported absorption coefficients of single crystals.[61,74] It should be noted that both DRS and absorption coefficient measurements are sensitive to low energy transitions, especially localized *d*-*d* transitions. The optical bandgaps of conventional ferroelectric oxides $PbTiO_3$ and $BaTiO_3$ calculated from the Tauc plots in **Figure 2.1**c, were also in agreement with the well-accepted literature values.[75]

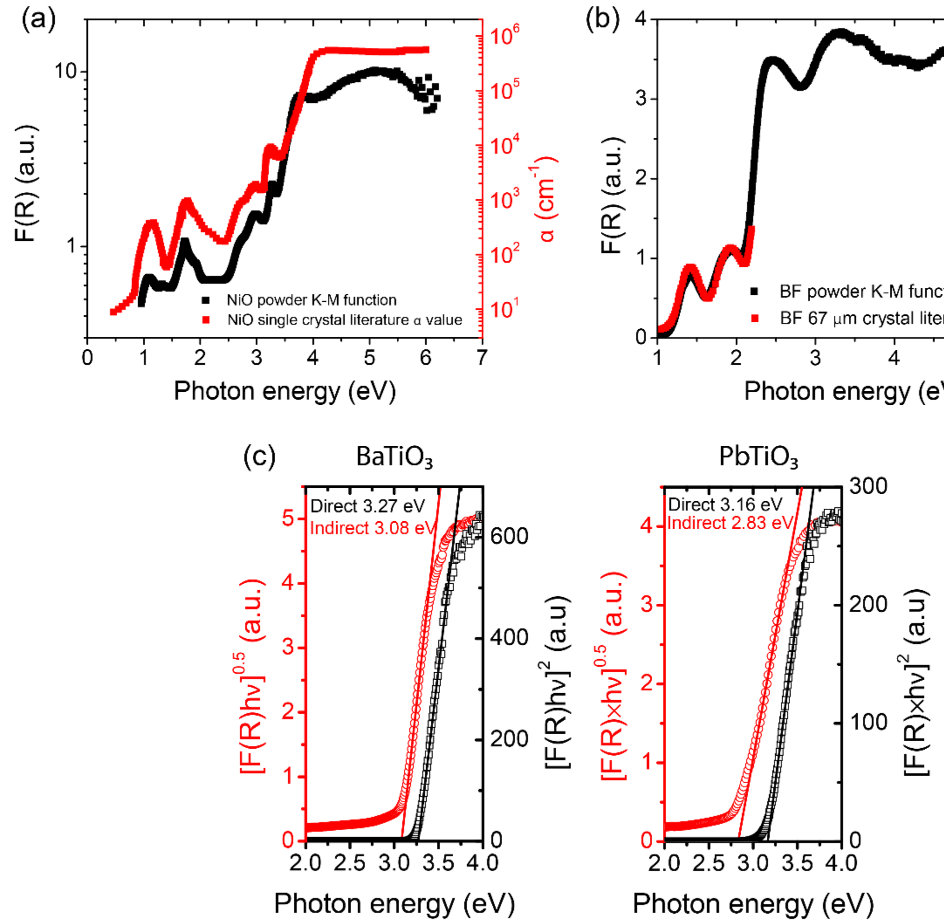

Figure 2.1 UV-vis diffuse reflectance spectrum of known materials. (a) F(*R*) of NiO powder and absorption coefficient of NiO single crystal (adapted from reference *[74]*). (b) F(*R*) of $BiFeO_3$ powder and absorption coefficient of $BiFeO_3$ single crystal (adapted from reference *[61]*). (c) Tauc plots of $BaTiO_3$ and $PbTiO_3$.

2.2.4 Thermal Analysis

- Thermogravimetric Analysis (TGA)

The Ni oxidation state in the $KNbO_3$-based systems was determined using TGA (SDT-Q600, TA Instruments). Approximately 20 mg of the sample was heated from 25 °C to 1100 °C at a rate of 5°/min, during which the weight loss percentage was monitored.

Three different purge gases (*e.g.* air, argon, and forming gas - 5% H_2 + 95% N_2) were used to control the oxygen partial pressure; the purge flow was set to 100 ml/min

- Differential Scanning Calorimetry (DSC)

Samples of the $BaTiO_3$-based systems were analyzed by DSC (DSC-Q2000, TA Instruments) to identify the thermal signatures of any ferroelectric to paraelectric transitions. The DSC was calibrated using an indium standard and the measurements were conducted under dry helium by heating from 150 to 550 K at 10°/min.

- Dynamic Mechanical Analysis (DMA)

DMA (RSA III, TA Instrument) was employed to measure the storage modulus E' and mechanical loss tan(δ) of $PbTiO_3$-$Bi(Ni_{1/2}Ti_{1/2})O_3$ as a function of temperature (-150 °C to 450 °C) under different frequencies. The sample was cut into a thin ceramic bar with dimensions of $16 \times 4.5 \times 0.355$ mm^3 to accommodate the 3-point bending geometry as shown in **Figure 2.2**. A dynamic force at frequencies between 0.5 Hz to 16 Hz on top of a static force of 70 g was applied on the sample to generate a strain of 0.8%. These parameters were chosen to yield the largest strain without causing plastic deformation.

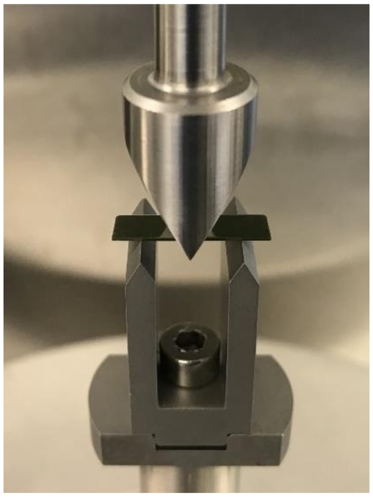

Figure 2.2 3-point bending setup of DMA

2.2.5 Electric Measurements

- Dielectric Properties

The permittivity ε_r and dielectric loss tan(δ) were measured with a precision *LRC* meter (4284A, Hewlett Packard) as a function of temperature and frequency. The sintered 8 mm diameter pellets were polished to 0.5 mm thickness and both surfaces were coated with silver paste (Heraeus ST601-14) to provide electrical contacts. The measurements were carried out in a parallel-plate capacitor configuration in a temperature-controlled chamber (-150 °C to 750 °C).

- Ferroelectric Properties

For the ferroelectric measurements, the samples were processed in the same manner as those for the dielectric characterization. The ferroelectric switching and hysteresis loops were measured at different frequencies (1 Hz to 10 Hz) using a commercial testing system with a high voltage interface and amplifier (Precision LCII Ferroelectric Test System, Radiant Technologies) located in Prof. Spanier's group at Drexel University. The samples were immersed in silicone oil in a Teflon sample fixture to prevent the electrical breakdown of air during ferroelectric testing.

2.2.6 Photovoltaic Measurements in the Probe Station

Two types of devices were fabricated for PV measurement. For the first device silver electrodes were coated on the two lateral sides of the samples (**Figure 2.3**a); the spacing between two electrodes was ~250 μm and the top surface was polished to a roughness below 10 nm. The second was a ~35 μm thick vertical device with a Si/Ag/Ferroelectric layer (~35 μm)/ITO architecture (**Figure 2.3**b). Both devices were polished using a precision polisher (MultiPrep Polishing System, Allied High Tech Products Inc.) with diamond lapping films. For the thinner vertical device, the 8 mm diameter pellet was first mounted on a Si wafer with silver epoxy (EPO-TEK H20E, Epoxy Technology) which served as the bottom electrode. The top surface of the sample was further polished until the sample thickness reached ~35 μm as monitored by a micrometer. The top electrodes of the vertical device comprised arrays of transparent, 150 nm thick pads of ITO patterned by photolithography and evaporated on the top surface at temperatures below 373 K. The temperature dependent PV measurements were carried out in a probe station (Model TTP4, Lakeshore Crayotronics) connected with a semiconductor parameter analyzer (Model 4200-SCS, Keithley) and the ferroelectric testing system (**Figure 2.3**e). The testing conditions for the lateral and vertical devices in the probe station are shown in **Figure 2.3**c and d respectively. The light sources include 405 nm, 450 nm, 532 nm, 635 nm lasers (Laser Diode Modules, Thorlabs) and an AM1.5 light source (LCS-100 Solar Simulator, Oriel Instruments).

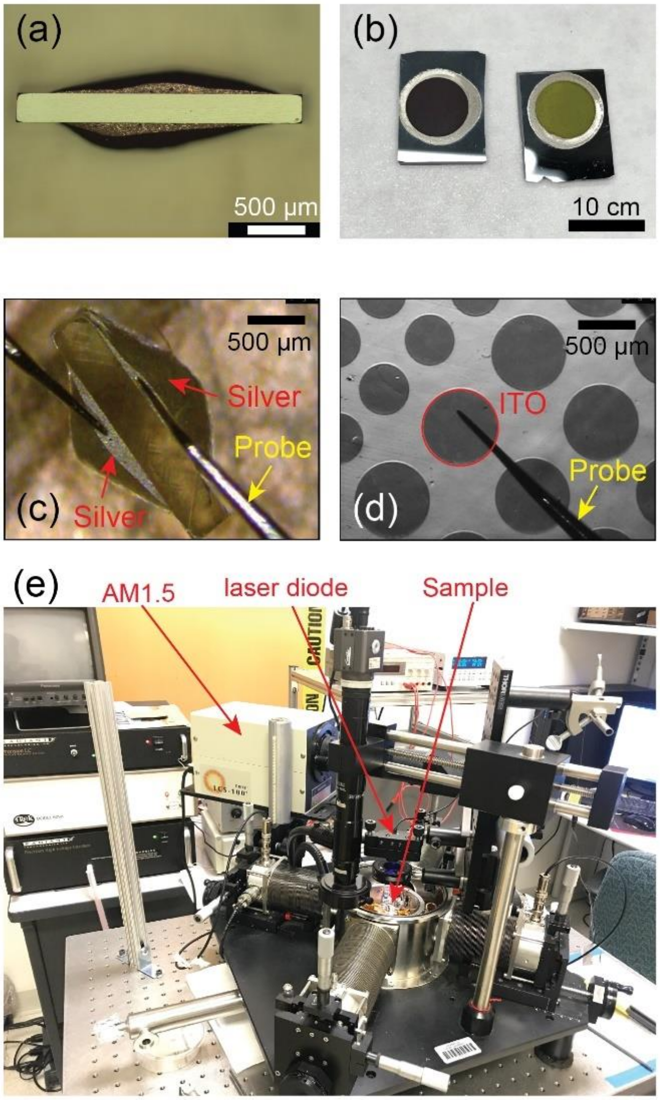

Figure 2.3 Experimental setup for PV measurements in the probe station. (a) Lateral device with Ag electrodes on two sides of the sample. (b) Vertical device with Ag bottom electrode and ITO top electrodes. (c) Lateral device in probe station with probes on two side electrodes. (d) Vertical device in probe station with a probe on one of the ITO top electrodes. (e) Probe station setup with light sources.

Chapter 3 Perovskite Niobates: Ni^{2+}, Oxygen Vacancy Substitutions

3.1 Introduction

The study of photovoltaic effects in ferroelectrics has a long history dating back to 1960s when photoinduced currents were first observed in $LiNbO_3$ and $BaTiO_3$ single crystals and later attributed to their lack of inversion symmetry. These effects fundamentally differ to PN junction-based photovoltaics and were named the bulk photovoltaic effect (BPVE). In the following decades, most research on the photovoltaic response of ferroelectrics focused on the physical mechanism of BPVE and less attention was paid to the material chemistry and application for energy conversion until the successful growth of $BiFeO_3$ epitaxial films.[9,59] The relatively narrow bandgap (2.7 eV) and domain-wall-generated anomalous photovoltages in thin film $BiFeO_3$ revealed their potential for high efficiency solar energy conversion. However, the most obvious obstacle to the application as photovoltaic materials is the wide bandgap and the corresponding limited visible light absorption of most conventional ferroelectric compounds (*e.g.* $BaTiO_3$, $KNbO_3$, $PbTiO_3$, etc.).

To overcome this barrier efforts were made to design narrow gap systems; bandgap tunable $Bi_4Ti_3O_{12}$-$LaCoO_3$ superlattice films, where the smallest bandgap is ~2.65 eV, and a weakly ferroelectric $KBiFe_2O_5$ single crystals (1.6 eV) were reported.[10,47] Using first principles methods, theoretical calculations indicated that Ni^{2+}-oxygen vacancy substitutions into $PbTiO_3$ would also result a decreased bandgap while enhancing the polarization of the parent ferroelectric end-member.[58] While experimental attempts to prepare Ni-substituted $PbTiO_3$ (*i.e.* $PbTi_{1-x}Ni_xO_{3-\delta}$) bulk ceramics were unsuccessful, this theoretical work inspired the discovery of new Ni-substituted oxide solid solutions, $(1-x)KNbO_3-(x)Ba(Ni_{1/2}Nb_{1/2})O_{2.75}$ (KBNNO), that combined ferroelectricity and direct bandgaps ranging from 1.1 to 3.8 eV.[46] Following the publication of that work, many other studies of KBNNO and other ferroelectric compounds have been reported with the goal of further lowering the bandgap and realizing the application of ferroelectric materials in photovoltaic devices.

In KBNNO, the two end-members $KNbO_3$ and $Ba(Ni_{1/2}Nb_{1/2})O_{2.75}$ were chosen to promote ferroelectricity and induce an E_g in the visible range, respectively. More specifically, the d^0 Nb^{5+} cations on the B-site provide ferroelectrically active, off-centered distortions and polarization through a second-order Jahn-Teller effect and with the combination of Ni^{2+} and oxygen vacancies giving rise to electronic states in the gap. The choice of $KNbO_3$ instead of $PbTiO_3$ as the ferroelectric end-member was made based on the higher tolerance of niobite perovskites for the formation of oxygen vacancies.

A part of the work conducted at the beginning of this Ph.D. thesis research, in particular optimization of the synthesis techniques and studies of the phase stability and dielectric properties, contributed to the final stages of the original published study of KBNNO in reference [46]. While the thesis ultimately focused on other substituted perovskite ferroelectric oxides, additional investigations of KBNNO were made and these are documented in this chapter. The work included here includes: (a) the phase stability and optical properties of the $Ba(Ni_{1/2}Nb_{1/2})O_{2.75}$ end member to establish a reference for the analysis of the properties of KBNNO; (b) more detailed studies of the phase stabilities of KBNNO from $x = 0$ to 0.5 to identify the trace impurities and to seek evidence for a nickel redox reaction using TGA; (c) additional studies of the dielectric response of KBNNO.

3.2 Synthesis Details

Solid solutions investigated in this chapter were synthesized by the standard procedures described in Section 2.1. For nonstoichiometric $Ba(Ni_{1/3}Nb_{2/3})O_3$, the raw mixtures were first calcined at 900 °C for 12 hrs. Multiple subsequent firings were carried out to achieve single phase purity prior to sintering. Green bodies were sintered for 12 hrs at temperatures between 1350 to 1450 °C according to the composition. For $(1\text{-}x)KNbO_3\text{-}(x)Ba(Ni_{1/2}Nb_{1/2})O_{2.75}$ and $(1\text{-}x)(K_{0.5}Na_{0.5})NbO_3\text{-}(x)Ba(Ni_{1/2}Nb_{1/2})O_{2.75}$, the raw mixtures were first calcined at 700 °C for 6 hrs and then sintered for 2 hrs at temperatures between 1135 to 1225 °C according to the compositions; higher concentration of $Ba(Ni_{1/2}Nb_{1/2})O_{2.75}$ requires higher sintering temperature.

3.3 Nonstoichiometric $Ba(Ni_{1/3}Nb_{2/3})O_3$

$Ba(Ni_{1/3}Nb_{2/3})O_3$ is a well-known “1:2” ordered perovskite which shows low dielectric loss and good photocatalytic properties.[76,77] It has been reported that small deviations in the stoichiometry of the B-site cations in $Ba(Ni_{1/3}Nb_{2/3})O_3$ and other related ordered perovskites have a profound effect on their ordering and dielectric properties.[78,79] $Ba(Ni_{1/2}Nb_{1/2})O_{2.75}$, which was used as the Ni-containing end-member in the original studies of KBNNO, can be re-written as the $x = 0.25$ composition in along the $(1\text{-}x)Ba(Ni_{1/3}Nb_{2/3})O_3\text{-}(x)BaNiO_2$ pseudobinary; this non-stoichiometric solid solution,

$Ba(Ni_{(1+2x)/3}Nb_{(2-2x)/3})O_{3-x}$, is designated as "BNN" in the following text. To clarify the exact range of stability in BNN samples and examine the effect of any non-stoichiometry on the optical response, compositions along this tie-lie were explored for $0 \leq x \leq 0.25$.

3.3.1 Phase Stability

Figure 3.1a shows the XRD patterns collected from different samples of BNN for $x = 0$ to 0.25; the samples are single-phase perovskites for $x < 0.1$, where peaks from trace amounts of NiO are present. At $x = 0.25$ (*e.g.* $Ba(Ni_{1/2}Nb_{1/2})O_{2.75}$), the amounts of NiO become more significant and are accompanied by other, unknown, impurities. Slower scans of the single-phase $x = 0.0$ - 0.0625 compositions from 15° to 45° two theta, **Figure 3.1**b, indicate that the peaks associated with the 1:2 B-site ordering are only present in $x = 0$ and the other nonstoichiometric samples are completely disordered. The slower scans also show trace amounts of NiO can also be discerned at $x = 0.0625$.

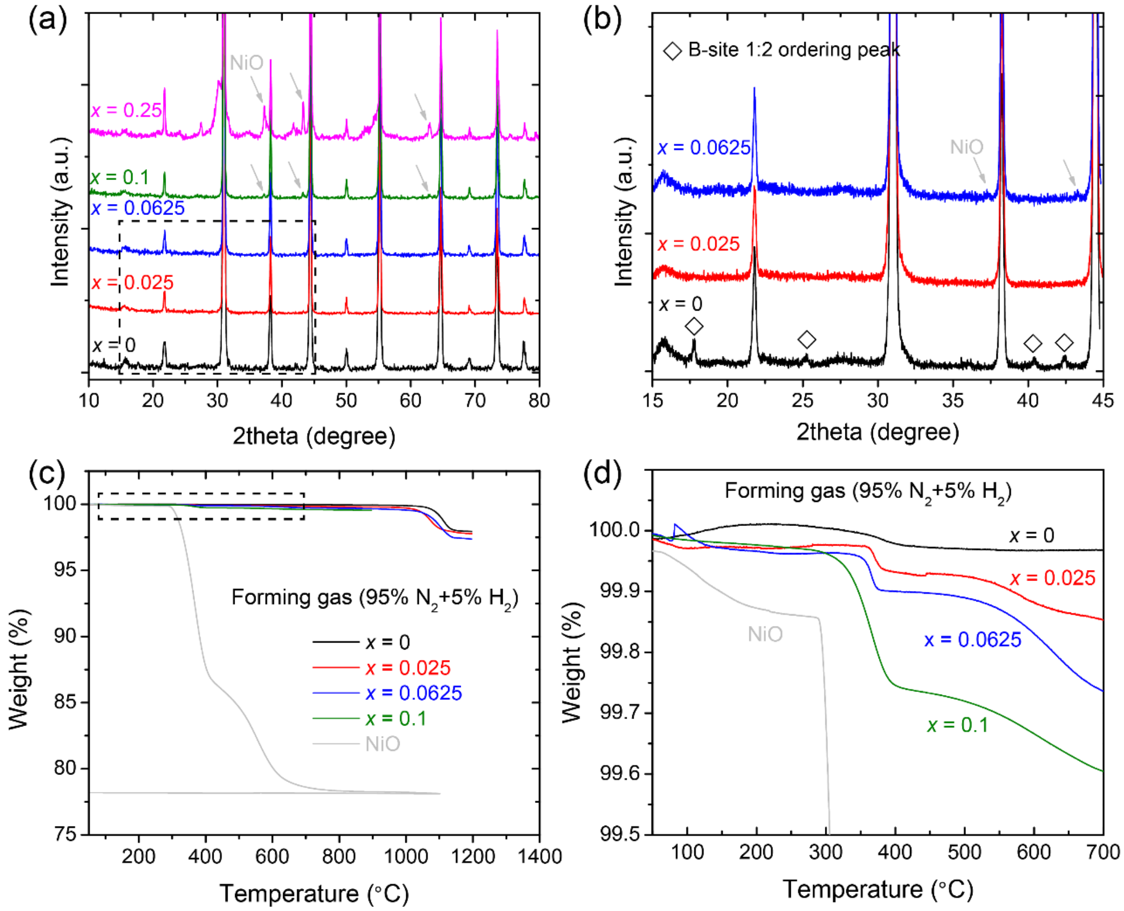

Figure 3.1 (a) XRD patterns of (1-x)Ba($Ni_{1/3}Nb_{2/3}$)O_3-(x)$BaNiO_2$ powders; (b) Slow scans of the 15° to 45° region for x = 0 to 0.0625, showing B-site 1:2 ordering peaks; (c) TGA signals of (1-x)Ba($Ni_{1/3}Nb_{2/3}$)O_3-(x)$BaNiO_2$ powders in forming gas (pure NiO is also included as a reference); (d) Zoom-in region of the TGA signals, showing weight loss transitions associated with the reduction of NiO.

TGA was also used to characterize the phase stability of BNN. Compositions were heated from 25 °C to 1200 °C at 5 °C/min in forming gas (*i.e.* 95% N_2 + 5% H_2) to monitor the weight loss during the subsequent decomposition of the samples when all of the Ni cations are reduced to nickel metal. Pure NiO was used as a standard to calculate the actual pO_2 and for comparison to the response of the BNN samples. Pure NiO, **Figure 3.1**c, shows a weight loss from 300 °C - 700 °C; the total loss, 21.74%, is close to the theoretical value

21.42% expected for reduction to Ni. Using the 300 °C onset temperature the oxygen pressure in the gas, calculated from the Ellingham diagram, is 10^{-34} atm.[80]

For the BNN compositions the weight loss does not begin until ~1100 °C, **Figure 3.1**c, consistent with the higher stability of Ni in the perovskites compared to NiO. The magnitude of the expected weight loss (η) is related to the stoichiometry of the BNN sample through the following equation:

$$\eta = \frac{16_{\mathrm{O}} \times (\frac{1}{3} + \frac{2}{3}x)}{137.3_{\mathrm{Ba}} + 58.7_{\mathrm{Ni}} \times (\frac{1}{3} + \frac{2}{3}x) + 92.9_{\mathrm{Nb}} \times (\frac{2}{3} - \frac{2}{3}x) + 16_{\mathrm{O}} \times (3 - x)}$$

For $x = 0$, the measured weight loss, $\eta = 1.977\%$, is close to the theoretical value (1.999%). For $x = 0.025$ and 0.0625, the weight losses are higher, $\eta = 2.063\%$ and $\eta = 2.263\%$ respectively, consistent with the formation of a perovskite enriched in Ni. The values of x calculated from the weight losses are 0.015 (nominal 0.025) and 0.06 (nominal 0.0625) which are both slightly smaller than the nominal values. The standard free energy difference ΔG° of the redox reaction $\frac{6}{1+2x}\mathrm{BaNi_{(1+2x)/3}Nb_{(2-2x)/3}O_{3-x}} \leftrightarrow 2\mathrm{Ni}(s) + \mathrm{O_2(g)} + \frac{2-8x}{1+2x}\mathrm{Ba_3Nb_2O_3} + \frac{6x}{1+2x}\mathrm{Ba_4Nb_2O_3}$ at 1100 °C can be calculated by $\Delta G^{\circ} = RT\ln(p\mathrm{O_2}) = -900$ kJ where R is the gas constant.

Detailed inspection of the BNN TGA data shows evidence for an additional very small weight loss at ~350°C (**Figure 3.1**d); the temperature of this mass loss is essentially the same as pure NiO and can be assigned to the reduction of trace amounts of unreacted NiO in the BNN samples. This small amount of unreacted NiO will cause a deviation from the designated Ni:Nb stoichiometry and is consistent with the slightly smaller x values calculated from the TGA data compared to the nominal values.

In summary, the (1-x)Ba($Ni_{1/3}Nb_{2/3}$)O_3-(x)$BaNiO_2$ pseudobinary has a solubility limit at $x \sim 0.1$, and Ba($Ni_{1/2}Nb_{1/2}$)$O_{2.75}$ is not a stable single-phase compound. The largest Ni:Nb ratio confirmed by TGA is $x = 0.06$ (*e.g.* Ba($Ni_{0.373}Nb_{0.627}$)$O_{2.94}$) which has 3% oxygen vacancies; none of the nonstoichiometric compositions have 1:2 B-site ordering.

Since a detectable amount of NiO is present in all nonstoichiometric compositions of BNN, it is arguably that the NiO can cause the destabilization of the B-site ordering. The effects of excess and deficient NiO on the B-site ordering are studied by making (1-x)Ba($Ni_{1/3}Nb_{2/3}$)O_3-(x)NiO and (1-x)Ba($Ni_{1/3}Nb_{2/3}$)O_3-(x)$BaNb_{2/3}O_{8/3}$ respectively where positive x represents the former and negative x represents the latter compositional line. In **Figure 3.2**, on the NiO-excess side, the B-site 1:2 ordering peak of $x = +0.06$ has similar magnitude compared to the stoichiometric $x = 0$ sample while on the NiO-deficient side, the ordering peak of $x = -0.02$ is strongly reduced. The NiO-excess (1-x)Ba($Ni_{1/3}Nb_{2/3}$)O_3-(x)NiO can also be represented as Ba_{1-x}($Ni_{(1+2x)/3}Nb_{(2-2x)/3}$)$O_{3-2x}$ which is very close to the previously discussed Ba($Ni_{(1+2x)/3}Nb_{(2-2x)/3}$)$O_{3-x}$ that is completely disordered. The maintained ordering in NiO-excess compositions is therefore attributed to the presence of both Ba vacancies and extra oxygen vacancies. This observation is also in agreement with the equivalent nonstoichiometric Ba($Zn_{1/3}Nb_{2/3}$)O_3 systems.[79]

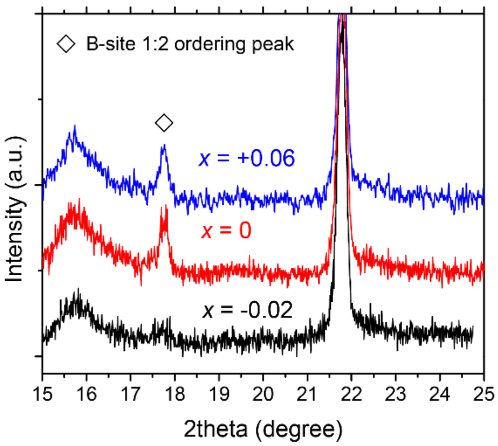

Figure 3.2 XRD patterns of NiO-excess (positive *x*) and NiO-deficient (negative *x*) $Ba(Ni_{1/3}Nb_{2/3})O_3$.

3.3.2 Optical Properties

The optical absorption properties of $(1-x)Ba(Ni_{1/3}Nb_{2/3})O_3-(x)BaNiO_2$ powders were characterized by diffuse reflectance spectroscopy; data collected from $x = 0$ to 0.25 are shown in **Figure 3.3**a . Stoichiometric $x = 0$ powders show high reflectance above 300 nm with several absorption peaks; the nonstoichiometric compositions show strong absorption over a broad range of wavelengths. The Kubelka-Munk transformations F(*R*) of are plotted in **Figure 3.3**b. The $x = 0$ sample has a sharp absorption edge at 3.5 eV - 4 eV associated with the O 2*p* to the Nb 4*d* charge transfer and two weak peaks at 1.6 eV and 2.8 eV which originate from *d*-*d* transitions of octahedral Ni^{2+}.[77] The F(*R*) for $x = 0.25$ shows the same absorption edge but with an overall enhancement of absorption below 3.5 eV and very weak peaks from *d*-*d* transitions; however, this composition is beyond the solubility limit and contains a significant fraction of impurity phases which could account for the overall increase of the absorption.

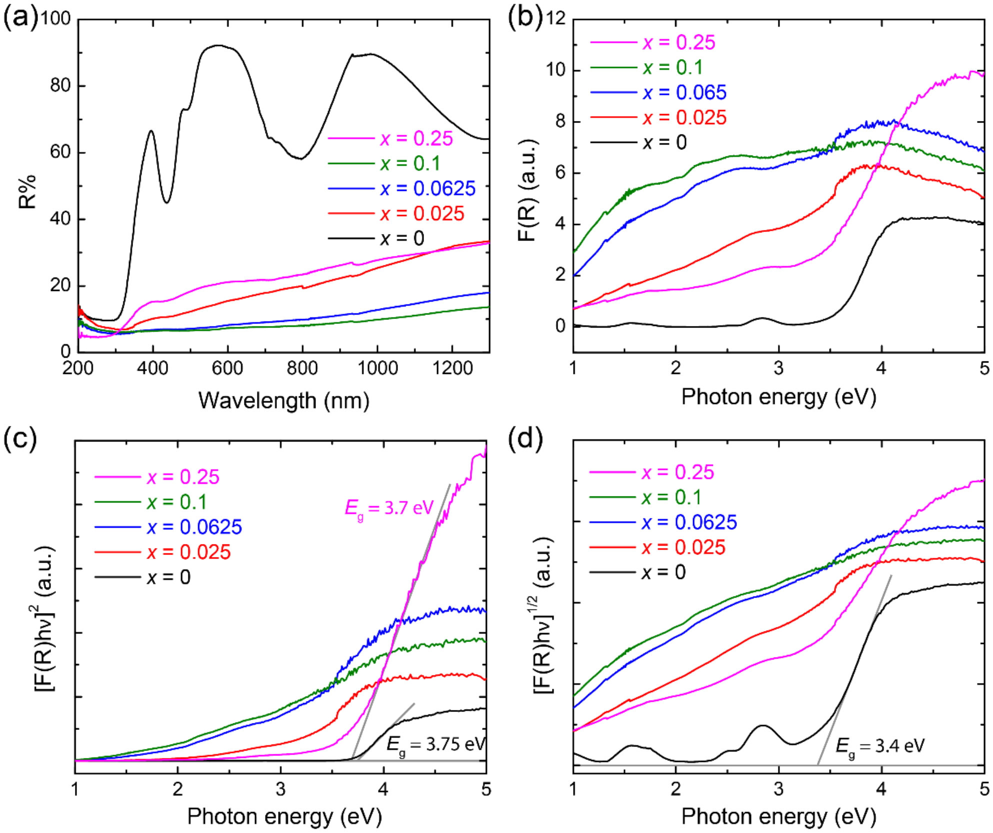

Figure 3.3 Optical absorption properties of (1-*x*)Ba($Ni_{1/3}Nb_{2/3}$)O_3-(*x*)$BaNiO_2$ powders: (a) UV-vis diffuse reflectence spectra; (b) Kubelka-Munk spectra; (c) Tauc plots for direct bandgap; (d) Tauc plots for indirect bandgap.

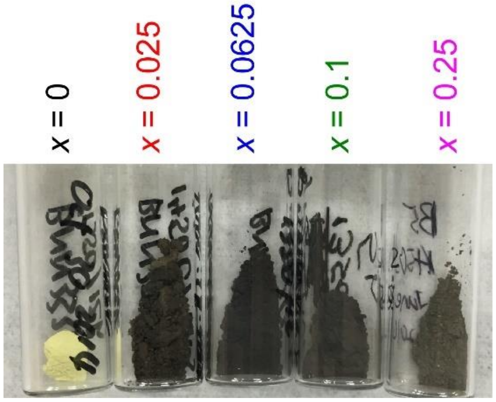

Figure 3.4 Picture of (1-*x*)Ba($Ni_{1/3}Nb_{2/3}$)O_3-(*x*)$BaNiO_2$ powders.

Compositions with x = 0.025 to 0.1, which lie within the solubility limit with an increased Ni:Nb ratio compensated by oxygen vacancies, have distinctly different absorption profiles. As x increases within this range, the absorption edge is shifted to lower energy for x = 0.025 and then gradually disappears at x = 0.0625 and 0.1; also for these compositions there is no clear evidence of peaks from *d-d* transitions. It should be noted that an absorption edge does appear to be present below 1 eV for x = 0.1, which may have the highest Ni:Nb ratio and oxygen vacancy concentration of all the compositions. Direct and indirect bandgaps were calculated from the Tauc plots, **Figure 3.3**c and d; x = 0 and 0.25 have essentially the same direct bandgap, ~3.7 eV, in agreement with previous reports.[77] An indirect bandgap of 3.4 eV can also be obtained for the x = 0 sample. Bandgaps for nonstoichiometric compositions within the solubility limit could not be obtained due to the absence of any well-defined linear region in the Tauc plot. The images of the BNN samples in **Figure 3.4** show the abrupt change in color that accompany the nonstoichiometry. From the study of the optical absorption of $(1\text{-}x)\mathrm{Ba(Ni_{1/3}Nb_{2/3})O_3}\text{-}x\mathrm{BaNiO_2}$, it can be concluded the nonstoichiometry induced by the additional $\mathrm{Ni^{2+}}$ content and oxygen vacancies increases the visible light absorption and potentially lowers the bandgap of the stoichiometric niobate.

3.4 $(1\text{-}x)\mathrm{KNbO_3}\text{-}(x)\mathrm{Ba(Ni_{1/2}Nb_{1/2})O_{2.75}}$

Although $\mathrm{Ba(Ni_{1/2}Nb_{1/2})O_{2.75}}$ is not a stable end-member by itself, it was used to examine the effect of small amounts of $\mathrm{Ni^{2+}}$ and oxygen vacancies on the optical absorption of ferroelectric $\mathrm{KNbO_3}$. Samples of $(1\text{-}x)\mathrm{KNbO_3}\text{-}(x)\mathrm{Ba(Ni_{1/2}Nb_{1/2})O_{2.75}}$ (KBNNO) were prepared with x = 0 to 0.5 and their phase stability and optical absorption was compared to nonstoichiometric BNN. The dielectric properties of KBNNO were also measured to characterize the ferroelectric phase transitions.

3.4.1 Phase Stability

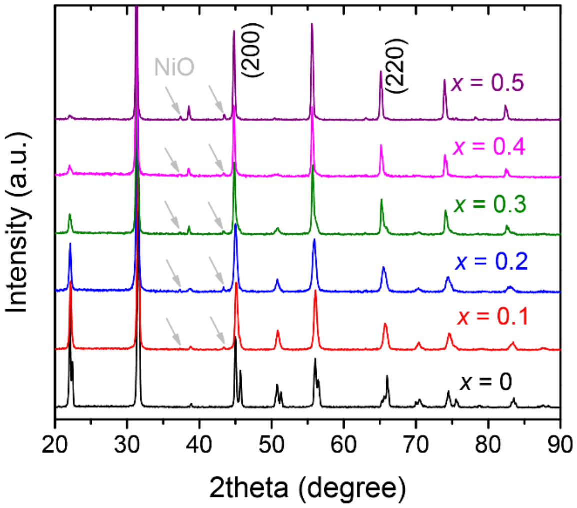

Figure 3.5 XRD patterns of (1-x)$KNbO_3$-(x)$Ba(Ni_{1/2}Nb_{1/2})O_{2.75}$ powders.

The XRD patterns of KBNNO (**Figure 3.5**) indicate the formation of perovskite solid solutions up to $x = 0.5$. Trace amounts of unreacted NiO, marked by arrows, are present in all KBNNO compositions. For x =0.1 to 0.3, the (200) and (220) pesudocubic reflections show clear broadening with a small shoulder on the right side of the peaks, indicating a slightly distorted orthorhombic structure. For $x = 0.4$ and 0.5 the structure transitions to cubic symmetry. A gradual shift of the peak positions to lower 2θ with increasing x was observed, **Figure 3.5**, consistent with the lattice expansion caused by the substitution of Nb^{5+} (0.64 Å) by the larger Ni^{2+} cation (0.69 Å).

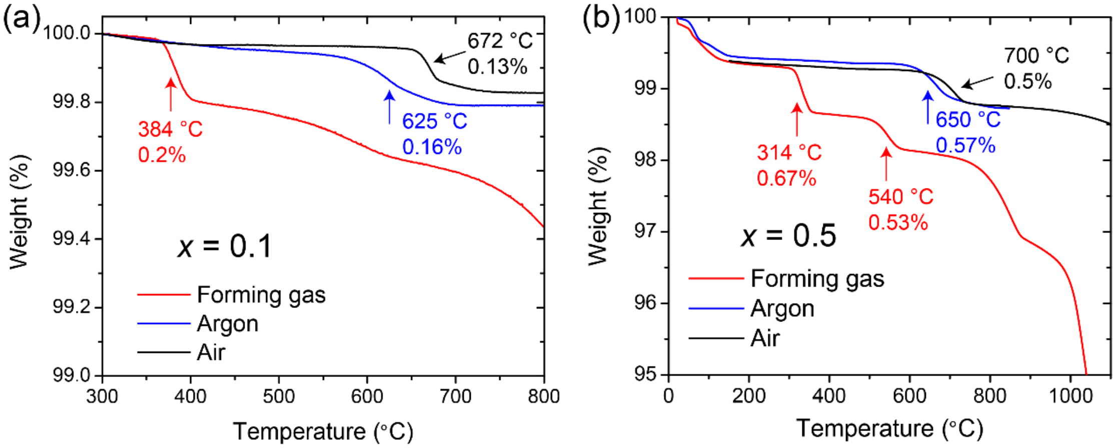

Figure 3.6 TGA of (a) $x = 0.1$ and (b) $x = 0.5$ KBNNO in air, argon and forming gases.

TGA analyses of $x = 0.1$ and 0.5 were conducted under forming gas, argon and air ($\log(pO_2) = -34$, -3 and -0.68 atm respectively). In forming gas, $x = 0.1$ has a sharp 0.2% weight loss at 384 °C associated with the reduction of the unreacted NiO (**Figure 3.6**a). Above 400 °C, the weight continues a gradual decrease from a series of transitions associated with the reduction and decomposition of KBNNO in forming gas; reliable quantification of the weight loss was not possible due to the continuous decreasing signal which could also have contributions from the volatilization of potassium. Under argon, a weight loss of 0.16% occurred at 625 °C with no additional change at higher temperature. A similar transition was present in air with slightly higher temperature (672 °C) and smaller weight loss (0.13%). This loss was found to be reversible when cooling in air (results are not plotted). NiO is stable above 1300 °C in air and argon, therefore these transitions are not associated with any decompositions of unreacted NiO and are likely associated with a Ni^{3+} to Ni^{2+} redox reaction in the perovskite phase. The formation of small amounts of Ni^{3+} in KBNNO is made possible by the refilling of oxygen vacancies during cooling after high temperature sintering.

The TGA results for x = 0.5, **Figure 3.6**b, are similar to those for x = 0.1 but with higher weight loss percentages, 0.5% - 0.6%, that allow better quantification of the redox chemistry. A transition of weight loss between associated with the reduction of Ni^{3+} to Ni^{2+} in the perovskite occurred around 540 °C in forming gas, 650 °C in argon and 700°C in air; the ΔG° of this redox reaction $4\mathrm{Ni}^{3+}_{\mathrm{B-site}} + 2\mathrm{O}^{2-} \leftrightarrow 4\mathrm{Ni}^{2+}_{\mathrm{B-site}} + \mathrm{O}_2(\mathrm{g})$ at these three temperatures can be calculated as -520 kJ, -56 kJ and -13 kJ respectively according to $\Delta G^{\circ} = RT\ln(\mathrm{pO}_2)$. The actual stoichiometry of the perovskite phase of x = 0.5 KBNNO could not be calculated from TGA in a similar manner as the previous BNN study because the weight loss for the reduction of Ni^{2+} in the perovskite phase occurs at the same temperature where severe K volatilization starts, making the dissociation of two reactions impossible. Ignoring the unreacted NiO impurity, the nominal composition of x = 0.5 is $K_{0.5}Ba_{0.5}Ni_{0.25}Nb_{0.75}O_{2.875+\delta}$ where the δ represents the extra oxygen introduced by oxidation to Ni^{3+}. For a 0.5% weight loss from reduction of Ni^{3+} to Ni^{2+}, δ can be calculated as 0.07, indicating Ni^{3+}: Ni^{2+} ≈ 1: 4.

3.4.2 Optical Properties

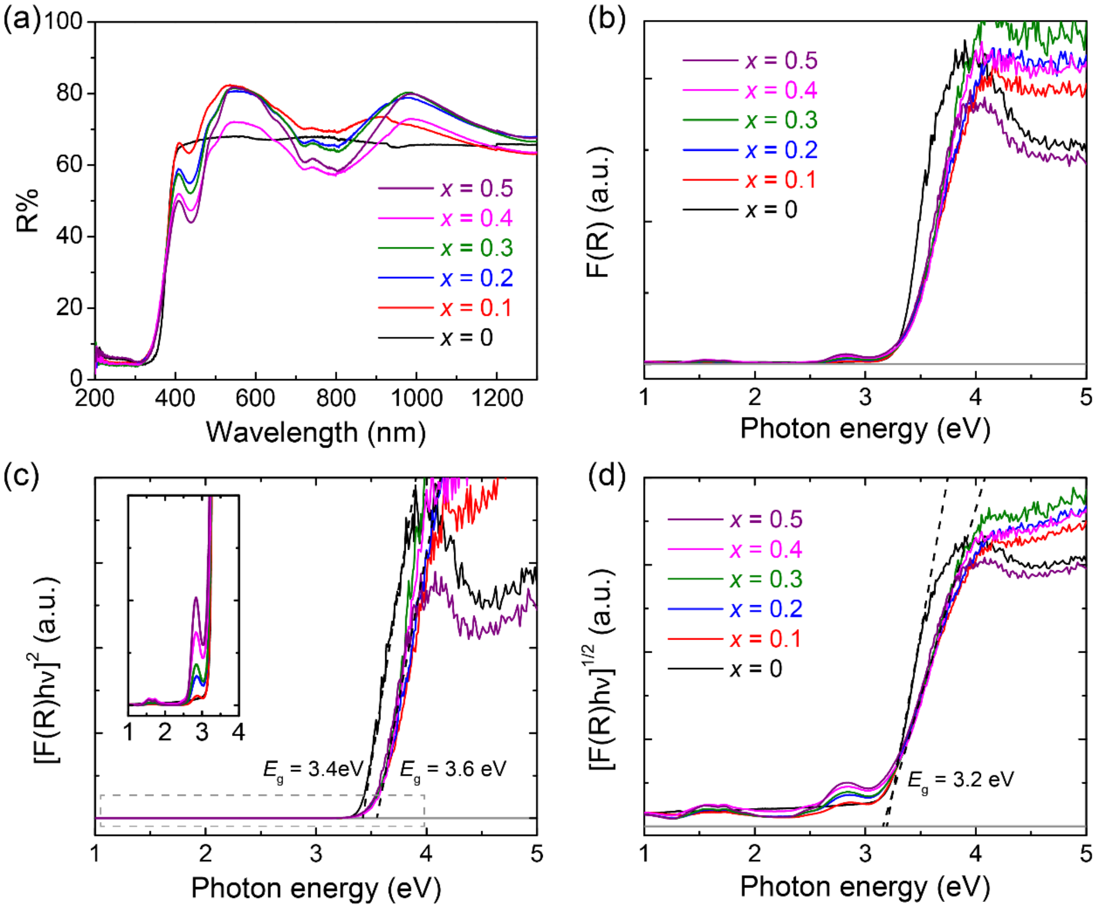

Figure 3.7 Optical absorption properties of (1-*x*)KNbO$_3$-(*x*)Ba(Ni$_{1/2}$Nb$_{1/2}$)O$_{2.75}$ powders: (a) UV-vis diffuse reflectence spectra; (b) Kubelka-Munk spectra; (c) Tauc plots for direct bandgap; (d) Tauc plots for indirect bandgap.

The optical absorption of KBNNO were characterized by measuring the diffuse reflectance spectra of ground powders of the $x = 0$ to 0.5 ceramics. In **Figure 3.7**a, $x = 0$ (KNbO$_3$) shows constant high reflectance up to the absorption edge (350 nm to 400 nm). The spectroscopic features of the $x > 0$ powders are similar to stoichiometric Ba(Ni$_{1/3}$Nb$_{2/3}$)O$_3$ where the *d*-*d* transitions of Ni^{2+} are responsible for the absorption peaks above 400 nm. The strength of these peaks increases as *x* increases. The Kubelka-Munk transformations F(R) of $x = 0$ and $x > 0$, **Figure 3.7**b, exhibit different absorption edges with $x > 0$ at a slightly higher energy; the small *d-d* transition peaks at 1.6 eV and 2.8 eV are similar to $Ba(Ni_{1/3}Nb_{2/3})O_3$. The bandgaps estimated from extrapolation of the linear parts of the Tauc plots, **Figure 3.7**c, yield direct gap energies of 3.4 eV for $x = 0$ and 3.6 eV for all $x > 0$ samples close to the 3.7 eV gap of $Ba(Ni_{1/3}Nb_{2/3})O_3$. The *d-d* transitions do not contribute to the band to band absorption and are only visible when scale is greatly expanded (see inset **Figure 3.7**c); the indirect gap is 3.2 eV for all samples (**Figure 3.7**d).

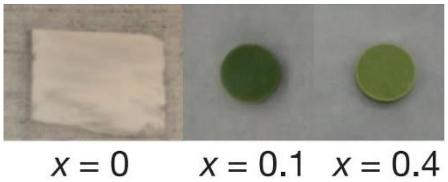

Figure 3.8 Picture of $(1\text{-}x)KNbO_3\text{-}(x)Ba(Ni_{1/2}Nb_{1/2})O_{2.75}$ samples.

The sintered KBNNO ceramics with $x > 0$ have a distinct green color compared to the $x = 0$ sample as shown in **Figure 3.8**. The color change originates from the *d-d* transitions rather than from the small bandgap difference. There are other extrinsic factors such as grain boundary and pore scattering that can affect the color of the ceramic samples and produce spectroscopic responses different to the powder samples. It is possible the 1.4 eV bandgap of KBNNO obtained from ellipsometry measurements on bulk ceramics is associated with these extrinsic optical responses.[46]

The response of the optical absorption of BNN and KBNNO to nonstoichiometry are clearly different. Although B-site Ni and oxygen vacancies are present in both cases, the shift of the absorption edge to lower energy and the strong increase of visible light absorption in nonstoichiometric $Ba(Ni_{1/3}Nb_{2/3})O_3$ was not observed in KBNNO. Moreover, the characteristic optical absorption from *d*-*d* transitions in BNN disappears immediately with small amounts of nonstoichiometry, while in KBNNO it was enhanced as the Ni concentration increases. In BNN the concentration of Ni on the B-sites exceeds 33.3%, in KBNNO the highest concentration, at x = 0.5, is 25%. It is possible the smaller Ni concentrations in KBNNO and the associated lower probability for the formation of Ni^{2+}-$V_O^{\bullet\bullet}$-Ni^{2+} or Ni^{2+}-$V_O^{\bullet\bullet}$-Nb^{5+} linkages are crucial in the mediating the response of the bandgap.

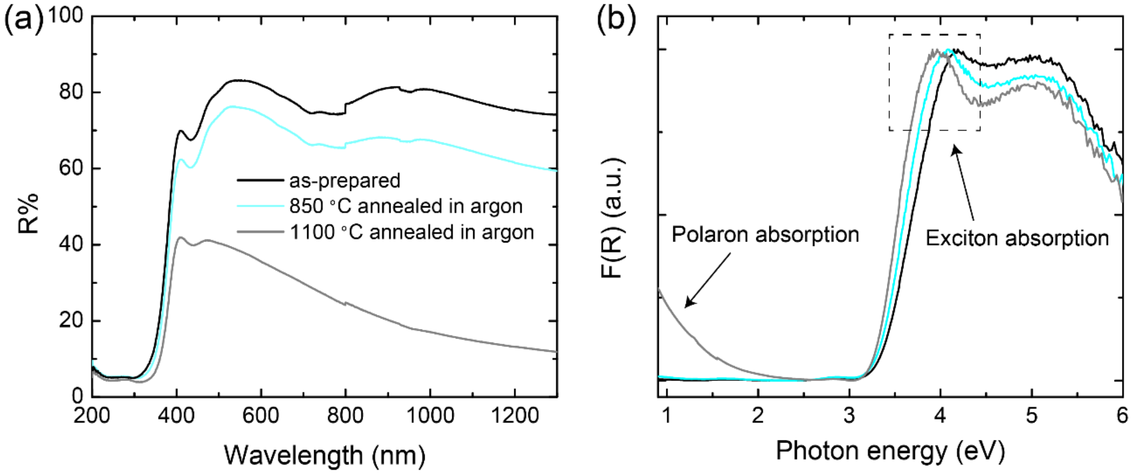

Figure 3.9 Optical absorption properties of x = 0.1 KBNNO powders anneald in argon: (a) UV-vis diffuse reflectence spectra; (b) Kubelka-Munk spectra.

To study the effect of oxygen vacancies on the optical absorption, samples of x = 0.1 KBNNO were annealed in argon at 850 °C and 1100 °C for 30 mins, temperatures where the TGA results indicated any Ni^{3+} is reduced to Ni^{2+}, and rapidly quenched to 25 °C to preserve the oxygen stoichiometry. The diffuse reflectance spectra collected after 850 °C and 1100 °C argon-annealing are compared to the as-prepared x = 0.1 KBNNO sample in **Figure 3.9**a. The 850 °C anneal slightly reduces the reflectance in the 400 nm to 1300 nm region, while the 1100 °C treated sample shows a more significant decrease in this range. The Kubelka-Munk transformations F(R) of three samples, **Figure 3.9**b, show two spectroscopic features are affected by the annealing history. The first is an absorption band extending from 2 eV into the near infrared region, which is most prominent after the 1100 °C heat treatment. This feature is associated with light-induced polaron motion between equivalent trapping sites and has been widely reported in other reduced titanates and niobates.[81,82] Here the 1100 °C annealing enables the formation of electrons which can be self-trapped at Nb^{5+} as polarons to compensate the extra oxygen vacancies. In contrast for the 850 °C anneal the oxygen vacancies are ionically compensated by Ni^{2+} and the optical absorption from polaronic motion is absent. The second feature is the strengthening of an absorption peak superimposed on the absorption edge as the oxygen vacancy concentration increases; this peak is likely related to the excitonic absorption. The width of this peak, ~0.5 eV, is consistent with the calculated binding energy of excitons in $KNbO_3$.[83] After the 1100 °C anneal a coexistence of oxygen vacancies and self-trapped electrons can form defect complexes of Ni^{2+}-$V_O^{\bullet\bullet}$ and Nb^{4+}-O^{2-} respectively. The photo-excited electrons can be easily trapped by the Ni^{2+}-$V_O^{\bullet\bullet}$ centers and the holes by Nb^{4+}-O^{2-} centers, leading to the formation of excitons. This simple defect model explains the observed enhancement of the excitonic absorption peak in the 1100 °C sample.

In summary, the effect of oxygen vacancies on the optical absorption of KBNNO is governed by the defect chemistry through polaron and exciton formations. However, there is no clear evidence of change in the fundamental gap of KBNNO with the increase of the oxygen vacancy concentration.

3.4.3 Dielectric Response

To investigate the effect of alloying BNN on the ferroelectric phase transitions of $KNbO_3$, the dielectric permittivity and loss of $x = 0.1$ and 0.2 KBNNO samples were measured as a function of temperature and frequency. Composition $x = 0.1$ shows dielectric anomalies at 410 °C and 260 °C (see **Figure 3.10**a); although the anomalies are broad, these temperatures are similar to the sharp ferroelectric transitions in pure $KNbO_3$. The diffuseness of the ferroelectric phase transition was also observed in temperature dependent Raman scattering measurements of the samples and explained by the observation of a distribution of Nb displacements in DFT calculations of the local structure.[72] The absence of any frequency dependence indicates normal as opposed to relaxor type ferroelectric behavior. **Figure 3.10**b shows a comparison of dielectric responses of $x = 0.1$ and 0.2 measured at 1 MHz; the heating and cooling cycles show a small thermal hysteresis for the transitions in $x = 0.1$. For $x = 0.2$, no dielectric anomalies were observed, indicating the gradual loss of ferroelectricity as x increases.

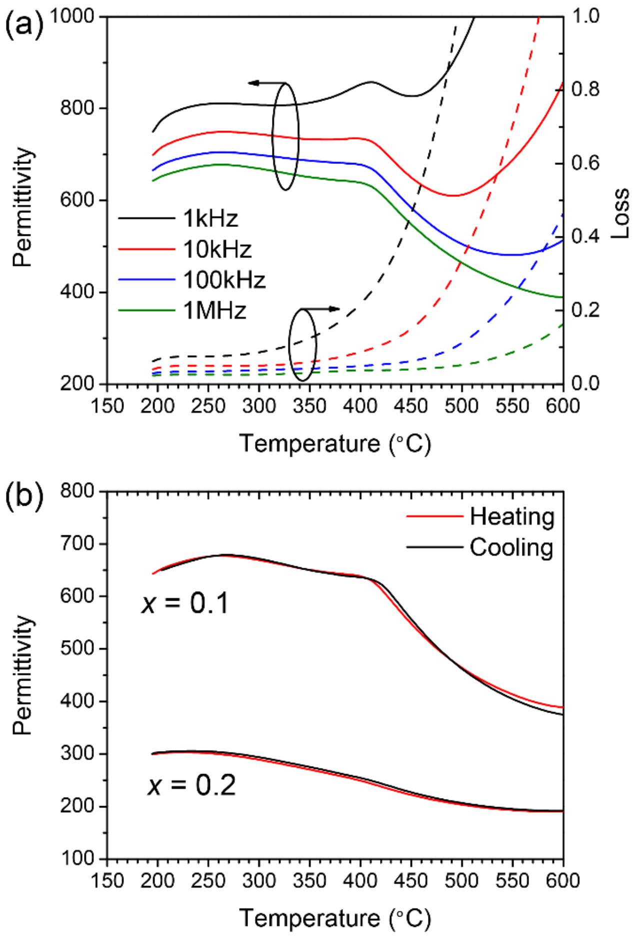

Figure 3.10 Dielectric properties of KBNNO. (a) Tempearture dependence of permittivity and dielectric loss of x = 0.1 for various frequencies. (b) Dielectric response of heating and cooling cycles for x = 0.1 and 0.2 samples measured at 1 MHz.

3.5 Sodium Substitution: (1-x)($K_{0.5}Na_{0.5}$)NbO_3-(x)Ba($Ni_{1/2}Nb_{1/2}$)$O_{2.75}$

3.5.1 Phase Stabilities and Optical Properties

BNN substitutions were also applied to a ferroelectric MPB end-member, ($K_{0.5}Na_{0.5}$)NbO_3. **Figure 3.11** shows the XRD patterns and diffuse reflectance spectra of (1-x)($K_{0.5}Na_{0.5}$)NbO_3-(x)Ba($Ni_{1/2}Nb_{1/2}$)$O_{2.75}$ (KNBNNO) solid solutions with x = 0 to 0.4. Essentially single-phase perovsites were obtained at all compositions with trace amounts of unreacted NiO. As *x* increases, the perovksite peaks shift slightly to lower angles indicating an expansion of the unit cell from the subsitution of Nb^{5+} (0.64 Å) by Ni^{2+} (0.69 Å) and K^+(1.64 Å)/Na^+(1.39 Å) by Ba^{2+} (1.61 Å). Peak broadening due to the distortion of the unit cell is present up to $x = 0.3$, above which the structure is cubic and the response of the structure is similar to KBNNO.

The optical absorption of KNBNNO, **Figure 3.11**b also resembles that of KBNNO. The substitution of BNN introduces peaks from *d-d* transitions that strenghten with increasing *x*. No significant changes are observed in the posotion of the fundamental absorption edge.

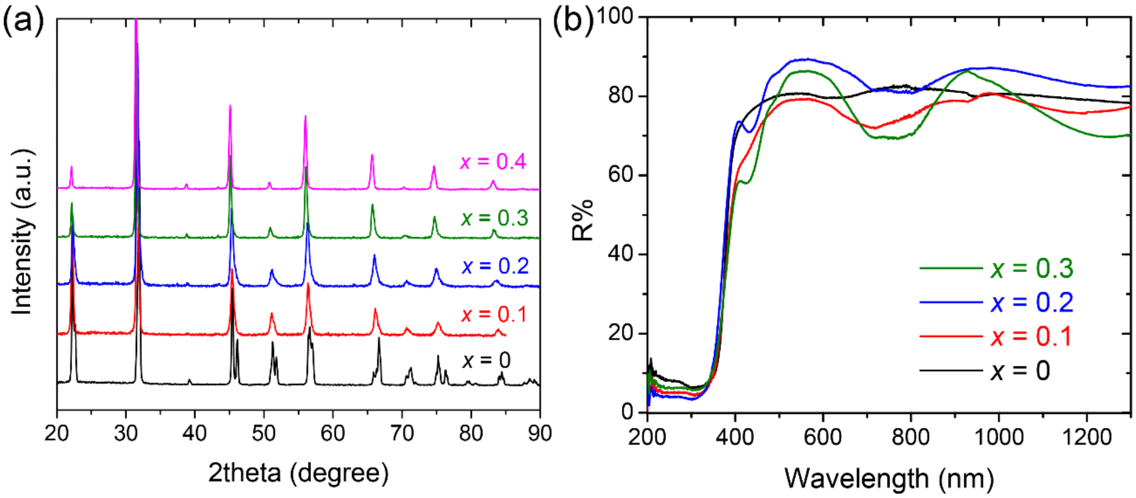

Figure 3.11 (a) XRD patterns and (b) diffuse reflectance spectra of KNBNNO powders.

3.5.2 Dielectric Response

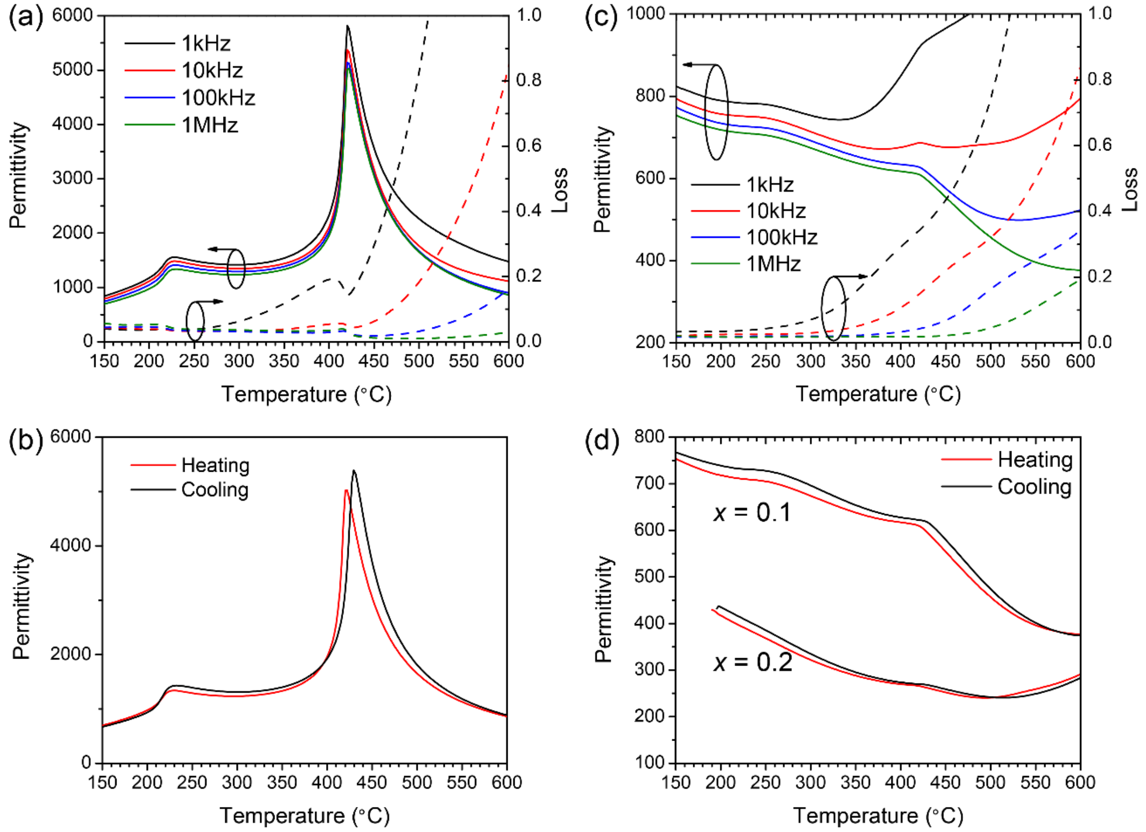

Figure 3.12 Dielectric properties of KNBNNO. (a) Temperautre dependence of permittivity and dielectric loss of $(K_{0.5}Na_{0.5})NbO_3$ for various frequencies. (b) Dielectric response of heating and cooling cycles for $(K_{0.5}Na_{0.5})NbO_3$ measured at 1 MHz. (c) Temperautre dependence of permittivity and dielectric loss of $x = 0.1$ sample for various frequencies. (d) Dielectric response of heating and cooling cycles for $x = 0.1$ and 0.2 samples measured at 1 MHz.

A reason for utilizing an MPB composition $(K_{0.5}Na_{0.5})NbO_3$ as the ferroelectric end-member is the enhanced piezoelectric property and small energy barrier for ferroelectric switching which were found to be beneficial to the photovoltaic performance and for multi-source energy harvesting applications.[73] High quality $(K_{0.5}Na_{0.5})NbO_3$-based ceramics are also easier to fabricate as the MPB composition can accommodate the strains induced by the ferroelectric phase transition, preventing microcracks during sintering and cooling. The $x = 0$ KNBNNO sample shows sharp cubic to tetragonal and tetragonal to orthorhombic phase transitions at 420 °C and 220 °C respectively (see **Figure 3.12**a and b); the small frequency dispersion and losses indicate the sample is an excellent insulator. For $x = 0.1$ sample the transition peaks broaden and remain at temperatures as the $x = 0$ sample (see **Figure 3.12**c). The dielectric response of KNBNNO is very similar as KBNNO except the frequency dispersion and losses are smaller below 300 °C. **Figure 3.12**d shows the dielectric response of $x = 0.1$ and 0.2 at 1 MHz during heating and cooling. The $x = 0.2$ sample is barely ferroelectric evidenced by an extremely weak and broad transition around 420 °C, which is consistent with the broadened peaks observed in XRD.

3.6 Conclusions

In this chapter the response of the phase stability, optical absorption and dielectric properties of niobate based perovskites to Ni^{2+}-oxygen vacancy substitutions were studied in three systems: $Ba(Ni_{1/3}Nb_{2/3})O_3$ $KNbO_3$ and $(K_{0.5}Na_{0.5})NbO_3$. Solid solutions were formed between non-ferroelectric $Ba(Ni_{1/3}Nb_{2/3})O_3$ and $BaNiO_2$; a 10% solubility limit was found along with the destabilization of the B-site ordering. The change in the Ni:Nb ratio has a large impact on the optical absorption of this system; stoichiometric $Ba(Ni_{1/3}Nb_{2/3})O_3$ has a 3.7 eV direct bandgap with Ni^{2+} *d-d* transitions peaks at 1.6 eV and 2.8 eV, the solid solutions show enhanced visible light absorption without characteristics from *d-d* transitions.

Ferroelectric $KNbO_3$ and $(K_{0.5}Na_{0.5})NbO_3$ have similar responses to the introduction of Ni and oxygen vacancies. Solid solutions of KBNNO and KNBNNO were formed up to $x = 0.5$ through alloying with $Ba(Ni_{1/2}Nb_{1/2})O_{2.75}$. The Ni ions in as-prepared KBNNO were shown to adopt both 3+ and 2+ valence states. The substitution of Ni in KBNNO and KNBNNO also introduces *d-d* transitions at 1.6 eV and 2.8 eV, however the fundamental gap of the solid solutions (3.6 eV) is insensitive to the dopants. The optical absorption of KBNNO is also influenced by polaron and exciton formation when substantial amounts of oxygen vacancies are present. Dielectric measurements show broad and weak ferroelectric phase transitions for $x = 0.1$ KBNNO and KNBNNO at 420 °C and 220 °C.

Chapter 4 Light-absorbing $BaTiO_3$-based Ferroelectric Photovoltaics

4.1 Introduction

This chapter focuses on the bandgap engineering of ferroelectric $BaTO_3$ through the chemical substitution of Ni and Ni/Nb additives. This work was recently published in *Journal of the American Ceramic Society*, 102(7), 4188 – 4199 (2019) [reprinted with permission from Wiley]; aside from the general introduction, the text of that paper is used for this chapter.

As one of the most extensively studied ferroelectric oxides, $BaTiO_3$ has been the subject of numerous investigations. Recent measurements of the mesoscopic mean free path, high mobility non-thermalized carriers and nanoscale tip-enhanced bulk photovoltaic effects[17,26] highlight the potential of $BaTiO_3$ for emerging photovoltaic technologies. However, any practical $BaTiO_3$-based photovoltaic device with a competitive collection efficiency would require a significant lowering of the bandgap to promote visible-light absorption. In this paper the efficacy of the Ni^{2+}-$V_O^{\bullet\bullet}$ substitution schemes used to reduce the bandgap of $PbTiO_3$ and $KNbO_3$ are explored for $BaTiO_3$.[16,46]

$BaTiO_3$ is well known to accommodate the substitutional replacement of Ti^{4+} on the B-site by small concentrations of 3*d* transition metal acceptors (*e.g.* Cr^{3+}, Fe^{3+}, Mn^{3+}, Co^{3+}/Co^{2+}, Ni^{2+}).[84–88] However, the compensating $V_O^{\bullet\bullet}$ that accompany these substitutions stabilize a hexagonal 6H polymorph of $BaTiO_3$ that is paraelectric at room temperature. The transition from 3C cubic stacking to the 6H polymorph with an {..ABCBAC..} arrangement of the BaO_3 layers, is well-known in pure $BaTiO_3$ where the partial reduction of Ti and accompanying $V_O^{\bullet\bullet}$ stabilize the hexagonal structure above 1460 °C. In some acceptor-doped $BaTiO_3$ systems it is possible to selectively quench the hexagonal 6H form, stabilize the lower temperature 3C polymorph, or produce a mixture of the two by carefully controlling the annealing and cooling conditions.[85] The phase formation is not only dependent on the dopant level, but also on kinetics. For Mn-doped $BaTiO_3$ as-fired samples with Mn concentrations between 0.5 and 1.7 mol % form a mixture of the tetragonal (3C stacked) and hexagonal phases; by post-annealing under oxidizing or reducing atmospheres pure tetragonal phases with up to ~1.6 mol % Mn could be produced.[86] Partial stabilization of the 3C polymorph was also reported in a non-stoichiometric solid solution of $BaTiO_3$ + 0.04BaO + 0.001NiO after Ar- and O_2-annealing.[89] The impact of 3*d* transition metal acceptors on the band structure and enhancement of the optical absorption of $BaTiO_3$ has also been explored for Fe- and Cr-doped $BaTiO_3$.[84,88] In both cases absorption observed below the bandgap of undoped $BaTiO_3$ was associated with charge transfer processes mediated by mid-gap defect states.

Here the phase stability, optical, ferroelectric and photovoltaic responses of Ni- and (Ni-Nb)-substituted $BaTiO_3$ ceramics are explored. The choice of these substituents was guided by first principles calculations that predicted their potential in yielding low bandgap, photovoltaic materials in other ferroelectric hosts.[58,90,91]

4.2 Synthesis Details

Ceramic samples with the target compositions $Ba(Ti_{1-x}Ni_x)O_{3-x}$ and $(1-x)BaTiO_3$-$(x)[(1-y)Ba(Ni_{1/3}Nb_{2/3})O_3$-$(y)$"$BaNiO_2$"] were synthesized by the standard procedures described in Section 2.1. The stoichiometric raw mixtures were first calcined at 1100 °C for 12 hours and multiple subsequent firings were carried out to achieve single phase purity prior to sintering. Green bodies were sintered for 2 hrs at temperatures between 1350 to 1450 °C according to the composition. After sintering certain compositions were annealed, at temperatures specified later, for 24 hrs to promote equilibrium. Specific sample processing and testing procedures for temperature-dependent ferroelectric and PV measurements used in this chapter are described in the relevant sections.

4.3 Ba(Ti$_{1-x}$Ni$_x$)O$_{3-x}$ Solid Solutions

4.3.1Phase Stability and Ferroelectric Response

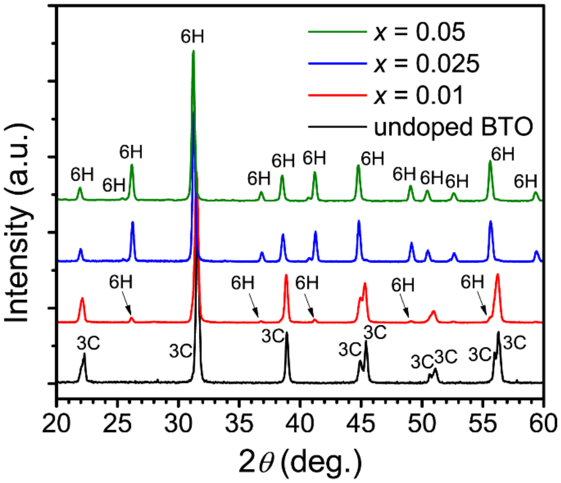

Figure 4.1 XRD patterns of the 1400 °C-sintered Ba(Ti$_{1-x}$Ni$_x$)O$_{3-x}$ powders (collected at room temperature)

The phase stabilities of Ba(Ti$_{1-x}$Ni$_x$)O$_{3-x}$ were investigated for $0.0 \leq x \leq 0.05$. **Figure 4.1** shows the XRD patterns of the samples prepared at 1400 °C (24 h) with x = 0.01, 0.025 and 0.05; the pattern of undoped BaTiO$_3$ is included for comparison. The x = 0.01 sample shows a coexistence of a tetragonal main phase with 3C stacking and a small amount of a secondary hexagonal 6H phase whose peaks are marked by arrows. For x =

0.025 and 0.05 the XRD patterns indicate the samples transform to a single phase hexagonal 6H structure.

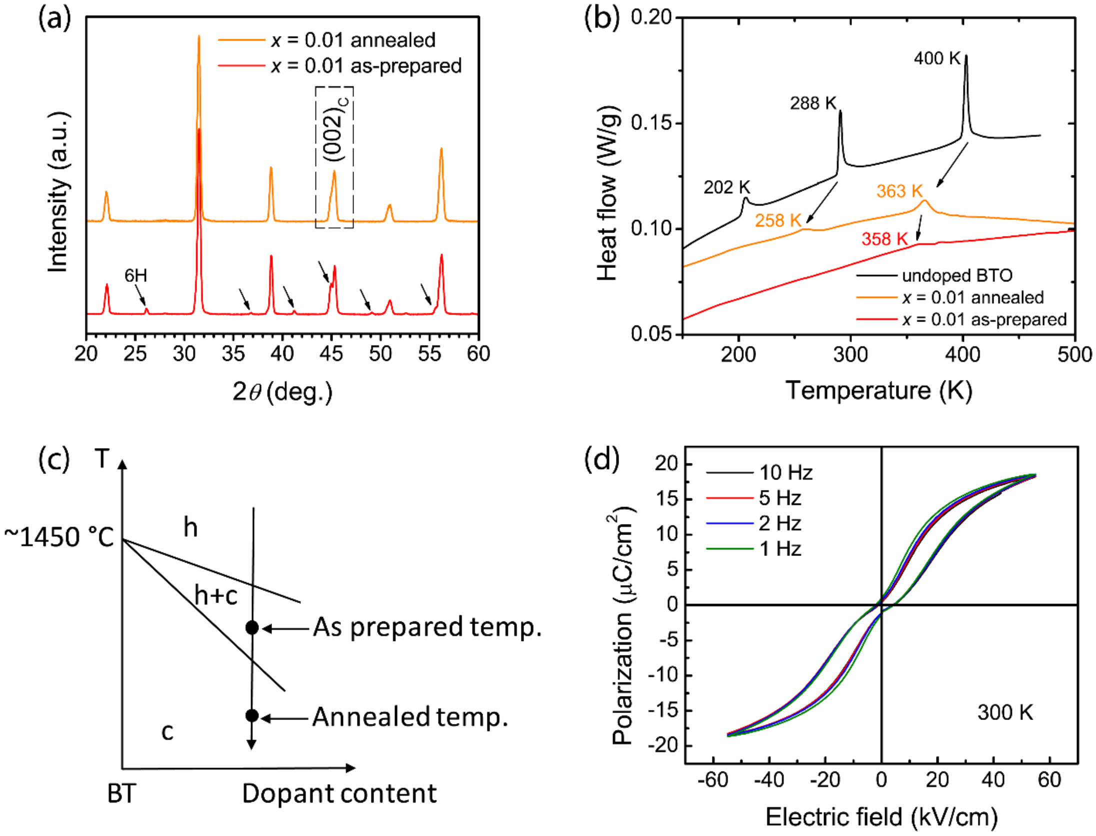

Figure 4.2 (a) XRD patterns of as-prepared and 1245°C annealed x = 0.01; (b) DSC scans from 150 to 500 K of as-prepared and 1245 °C annealed x = 0.01 (undoped $BaTiO_3$ included for comparison), showing endothermic peaks; (c) Schematic high-temperature phase diagram of Ni doped $BaTiO_3$, h = 6H phase, c =3C polymorph; (d) Ferroelectric P-E hysteresis loops of 1245°C annealed x = 0.01 collected at room temperature at different frequencies.

The phase stability at lower temperature was investigated through a series of annealing and quenching treatments of the x = 0.01 and 0.025 compositions. For example, the as-prepared x = 0.01 sample was re-annealed at 1245 °C for 24 hours and air-quenched to room temperature; the XRD pattern is compared to the as-prepared specimen in **Figure**

4.2a. The annealing eliminated the secondary 6H phase and all the peaks in the pattern could be indexed in terms of a single-phase tetragonal 3C-type structure. This indicates the 6H to 3C transition lies between 1245 and 1400 °C, a reduced temperature compared to the undoped system (**Figure 4.2**c), and confirms the room temperature stability of the 3C phase for $x = 0.01$. The broadening of the $(200)_c$ peak indicates the annealed $x = 0.01$ sample also undergoes a transition to a tetragonal ferroelectric phase, however the tetragonality is decreased compared to pure $BaTiO_3$.

The as-prepared and 1245 °C annealed $x = 0.01$ samples were investigated by DSC to seek evidence for thermal signatures associated with any phase transitions by constant rate heating; $BaTiO_3$ was used as a standard for comparison. A very small endothermic peak was identified in the as-prepared sample at ~358 K, more prominent endothermic peaks at 363 K and 258 K are evident in the scans of the single-phase, annealed $x = 0.01$ powders, see **Figure 4.2**b. The transition temperatures of the $x = 0.01$ sample are displaced to lower temperatures compared to $BaTiO_3$, with the cubic to tetragonal transition reduced from 398 K to 363 K and the tetragonal to orthorhombic transition from 288 K to 258 K. Thermal signals of a potential lower temperature orthorhombic to rhombohedral transition were not detected.

The single phase 3C-type $x = 0.01$ powder was sintered into a pellet at 1350 °C and the polarization versus electric field (P-E) hysteresis loops were collected to confirm its room temperature ferroelectricity, see **Figure 4.2**d. The loops show a pinched region close to the origin, a characteristic that has been observed in several aged acceptor-doped ferroelectrics[92–94] The constriction of the loop is associated with coupling between the local polarization and the acceptor-oxygen vacancy defect dipoles which can exert a restoring force and switch the domain back to its original state.[95] The observation of constriction is consistent with the presence of significant concentrations of oxygen vacancies in the sample, which are a potential source of ferroelectric degradation.[96–98] The morphology of the loop is independent of frequency indicating minimum contributions from leakage currents.

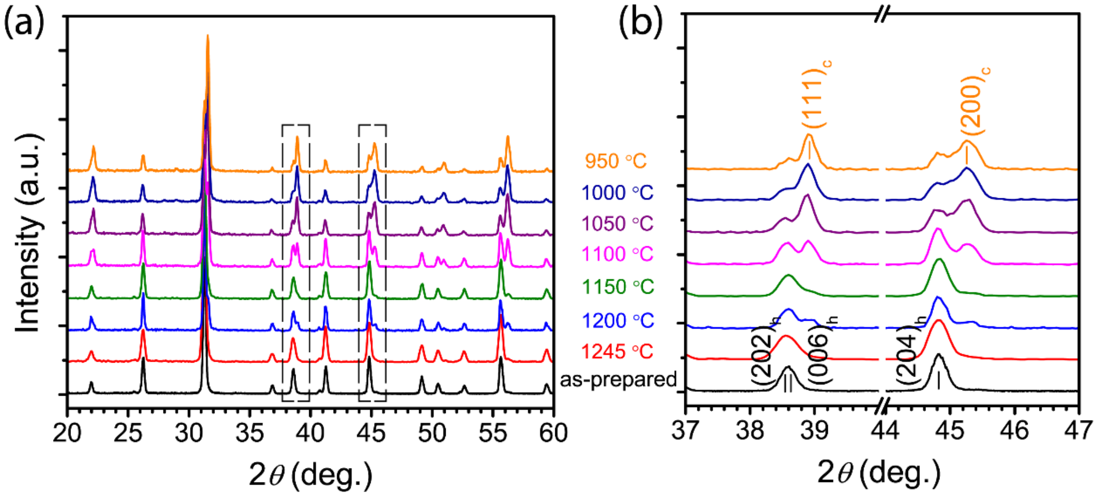

Figure 4.3 (a) XRD patterns of x = 0.025 annealed at different temperatures; (b) Expansion of 37°-40° and 44°-47° regions to highlight the change in phase content with annealing temperature

Annealing treatments were also carried out for x = 0.025, **Figure 4.3**a. As-prepared x = 0.025 has a single-phase hexagonal 6H structure; after annealing at 1245 °C for 24 hours, which promoted formation of a 3C polymorph for x = 0.01, the XRD pattern was unchanged. However, samples reheated at 1200 °C showed evidence for the formation of a 3C phase with the amount increasing as the annealing temperature was reduced to 1050 °C. The development of the patterns with decreasing annealing temperature, where the hexagonal $(202)_h$, $(006)_h$ and $(204)_h$ and pseudocubic $(111)_c$ and $(200)_c$ peaks were chosen to identify the respective 6H and 3C structures, is shown in **Figure 4.3**b. No further changes were observed after annealing at 1000 °C and a mixture of hexagonal and cubic phases was obtained. In contrast to $x = 0.01$, the $x = 0.025$ samples could only be partially converted to a 3C phase, presumably due to a relatively low transition temperature and associated slow kinetics.

4.3.2 Optical Properties

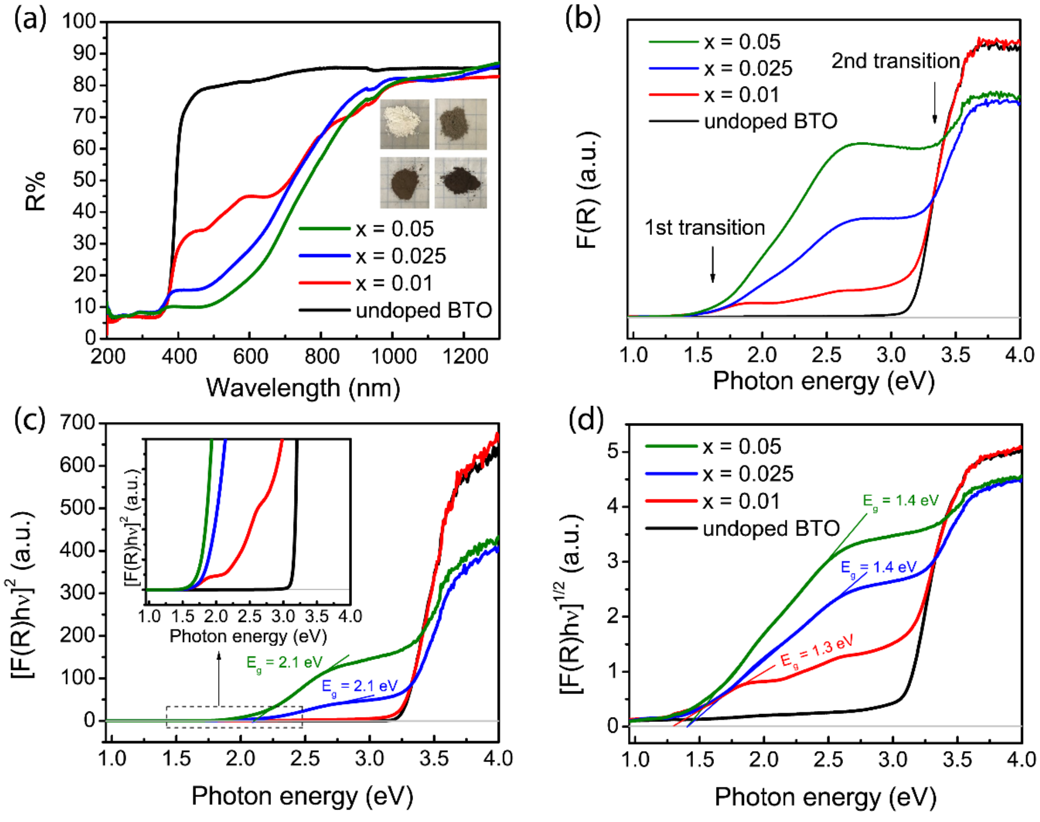

Figure 4.4 (a) UV-vis diffuse reflectance spectra of $BaTi_{1-x}Ni_xO_{3-x}$ powders with x = 0, 0.01, 0.025 and 0.05; (b) K-M transformed function F(R); (c) Tauc plots for direct bandgap; (d) Tauc plots for indirect bandgap.

The optical absorption spectra of the as-prepared Ba(Ti$_{1-x}$Ni$_x$)O$_{3-x}$ powders were collected by measuring the diffuse reflectance; the raw reflectance data, together with an image of each sample, is shown in **Figure 4.4**a. The x = 0.01 sample was primarily a 3C phase with a trace amount of 6H; x = 0.025 and 0.05 were single phase 6H. As the color changes from white for x = 0, to dark red for x = 0.05 the reflectance data show the incorporation of Ni induces a strong absorption starting at ~950 nm. The x > 0.0 samples all exhibit two absorption edges located at ~1.5 eV and 3.2 eV as shown in the Kubelka-Munk transformed absorption spectra in **Figure 4.4**b. As x increases, the first absorption edge at 1.5 eV becomes sharper and the absorption edge at 3.2 eV gradually broadens. This is strong evidence the substitution of Ni^{2+} and $V_O^{\bullet\bullet}$ introduces new mid-gap electronic states with a resultant optical gap of 1.5 eV. This implies that as the concentration of Ni^{2+} increases the states evolve from localized defects, which can introduce an Urbach tail,[99] to a new band that causes a lower energy transition. Tauc plots were used to estimate the magnitude of the direct bandgap ($[F(R)h\nu]^2$ versus photon energy hv, see **Figure 4.4**c. For x = 0.025 and x = 0.05 two linear regions can be resolved suggesting two electronic transitions; the line fit of the first transition yields a direct gap of 2.1 eV with the second at a value similar to the 3.2 eV gap of undoped BaTiO$_3$. The Tauc plot for x = 0.01 shows a 3.2 eV direct bandgap with a Urbach tail extending to 1.5 eV (see inset in **Figure 4.4**c). The Tauc plot for an indirect bandgap, ($[F(R)h\nu]^{1/2}$ versus photon energy hv, shows an absorption edge at 1.4 eV for x = 0.025 and x = 0.05 with a well-defined linear slope, **Figure 4.4**d. The x = 0.01 sample also exhibits an absorption onset around 1.3 eV; however, the extrapolation is not based on a well-defined linear region due to the localized nature of the defect states at such a level of substitution. The optical response of post-annealed *x* = 0.01, where the small amounts of 6H are converted to a phase pure 3C structure, was identical to the as-prepared sample.

4.3.3 Photoresponse

Measurements of the photoresponse of the annealed *x* = 0.01 ceramic were conducted at 300 K using a Au(~100 nm)/FE-layer(110 µm)/Ag architecture with a 400 µm diameter, 100 nm thick, Au top electrode. The sample was poled at 300 K using a 20 sec, 385 V (35 kV/cm) pulse before measurement of the photoresponse. The sign of the measured current is defined as positive for a flow from the top to bottom electrode through the sample. **Figure 4.5** shows the time dependence of the photocurrent at zero bias under dark and AM1.5 G illuminated conditions after positive (**Figure 4.5**a) and negative (**Figure 4.5**b) poling. A schematic of the polarization states after different poling is also shown in **Figure 4.5**. After positive poling, an initial transient dark current (–10 pA) was detected, **Figure 4.5**(a), with a decay to –5 pA within 200 s; the transient could be associated with a relaxation of mobile defects and charge carriers after the high voltage poling. The illumination induced a negative spike (–20 pA) which immediately dropped to –10 pA and gradually decayed to –8 pA after 200 s. When the light was switched off a positive spike was observed followed by a slowly decaying dark current of –4 pA. Re-illumination of the sample yielded the same photoresponse pattern which was reproducible in the subsequent light on/off modulations. The value of the steady-state photocurrent was ~ –3 pA. The sample exhibited a switchable photoresponse; the sign of the current was reversed after negative poling, **Figure 4.5**b. The switchable photoresponse provides evidence for a ferroelectric-induced photovoltaic effect; however, the steady state current is small and could be impacted by some light blockage by the Au top electrode and/or the low conductivity of the sample.

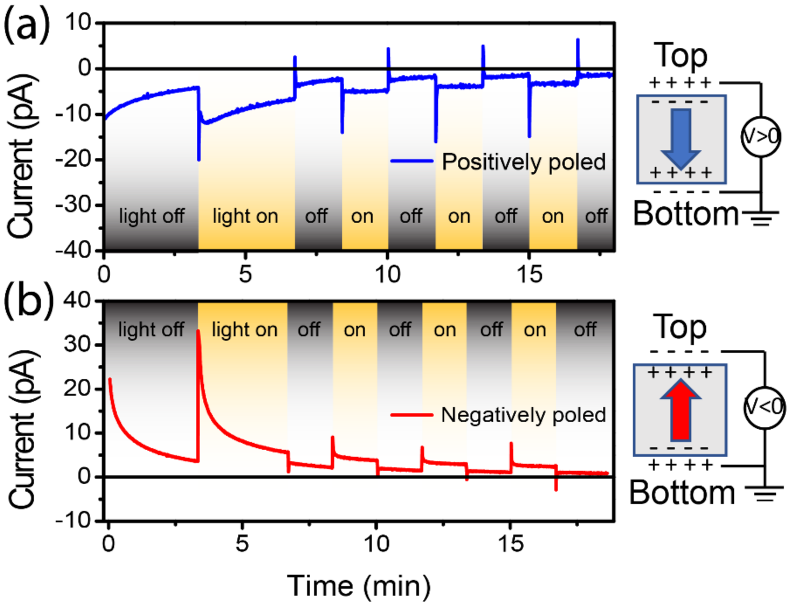

Figure 4.5 Photoresponses of (a) positively poled and (b) negatively poled of 1245 °C-annealed $x = 0.01$ sample measured under AM1.5 at 300 K.

4.4 Ni-Nb substituted BaTiO$_3$ Solid Solutions

When Ni retains a 2+ valence state the substitution of Ti in BaTiO$_3$ is charge compensated by the formation of an equal concentration of oxygen vacancies; in turn the vacancies promote formation of the 6H phase which was the only stable polymorph prepared for the Ba(Ti$_{1-x}$Ni$_x$)O$_{3-x}$ solid solutions $x = 0.05$. To isolate the impact of the concentration of Ni^{2+} and the $V_O^{\bullet\bullet}$ on the phase stability and optical absorption, a series of co-doped Ni-Nb BaTiO$_3$ solid solutions were prepared with varying ratios of Ni:Nb and $V_O^{\bullet\bullet}$. Previous first principles calculations and experimental studies of Ni-Nb substituted KNbO$_3$ photovoltaics focused on using Ba(Ni$_{1/2}$Nb$_{1/2}$)O$_{2.75}$ as the Ni^{2+}-$V_O^{\bullet\bullet}$ containing additive.[46] $Ba(Ni_{1/2}Nb_{1/2})O_{2.75}$, which is not a stable phase by itself, lies at a composition $y = 0.25$ within the $(1 - y)Ba(Ni_{1/3}Nb_{2/3})O_3$-$(y)$"$BaNiO_2$" (BNN) pseudo-binary system. With the assumption that Ni retains a 2+ valence state in the solid solution, the nominal $V_O^{\bullet\bullet}$ content (y) in the BNN end-member can be controlled by changing the ratio of Ni:Nb $= (1 + 2y)/2(1 - y)$ of BNN. For example, for $y = 0$ the end-member is a vacancy-free composition $Ba(Ni_{1/3}Nb_{2/3})O_3$; for $y = 1$ ("$BaNiO_2$") all of the Ni is compensated by vacancies and the resultant solid solutions with $BaTiO_3$ are identical to those described above as $Ba(Ti_{1-x}Ni_x)O_{3-x}$.

A series of $(1 - x)BaTiO_3$-(x)BNN compositions were prepared where the concentration of Ni $[= x(1 + 2y)/3]$ on the B-site was kept constant at 5% and the value of y in the BNN end-member was varied from $0.0 \leq y \leq 1.0$; the actual compositions investigated are summarized in **Table 4-1**.

Table 4-1 Compositions of BNN-substituted $BaTiO_3$ $(1\text{-}x)BaTiO_3$-$(x)[(1 - y)Ba(Ni_{1/3}Nb_{2/3})O_3$-$(y)$"$BaNiO_2$"] Sample

Sample label	Solid solution composition	x	y	% Ni on B-site	[Ni/(Ni+Nb)]	Oxygen vacancy concentration
A	$Ba(Ti_{0.85}Ni_{0.05}Nb_{0.1})O_3$	0.15	0	5%	33%	0%
B	$Ba(Ti_{0.857}Ni_{0.05}Nb_{0.093})O_{2.99643}$	0.143	0.025	5%	35%	0.12%
C	$Ba(Ti_{0.8667}Ni_{0.05}Nb_{0.0833})O_{2.99167}$	0.1333	0.0625	5%	37.5%	0.28%
D	$Ba(Ti_{0.875}Ni_{0.05}Nb_{0.075})O_{2.9875}$	0.125	0.1	5%	40%	0.42%
E	$Ba(Ti_{0.9}Ni_{0.05}Nb_{0.05})O_{2.975}$	0.1	0.25	5%	50%	0.83%
F	$Ba(Ti_{0.95}Ni_{0.05})O_{2.95}$	0.05	1	5%	100%	1.67%

4.4.1 Phase Stability

The XRD patterns collected from samples with 5% Ni on the B-site and $0 \leq [V_O^{\bullet\bullet}] \leq 1.67\%$ are compared to undoped $BaTiO_3$ in **Figure 4.6**a. Consistent with the results described earlier, the sample with the maximum concentration of vacancies ($y = 1$, $[V_O^{\bullet\bullet}] = 1.67\%$) has a single phase 6H hexagonal structure, while all the other patterns can be indexed in terms of a pure 3C phase. The patterns shown for samples A-D ($0.0 \leq [V_O^{\bullet\bullet}] \leq 0.42\%$) were collected from as-prepared samples sintered at 1450°C; the corresponding pattern for sample E ($[V_O^{\bullet\bullet}] = 0.83\%$) showed a mixture of 3C and 6H phases (**Figure 4.6**b) which completely converted to the single-phase 3C pattern shown in **Figure 4.6**a after a 48 hour post-anneal at 1150 °C. The $(111)_c$ peak reveals a systematic evolution of the lattice constant with the Ni, Nb, vacancy concentration. Substitution of BNN with $y = 0$, $Ba(Ni_{1/3}Nb_{2/3})O_3$ (sample A), increases the lattice constant relative to undoped $BaTiO_3$ consistent with the larger average radius of Ni^{2+} (0.69 Å) and Nb^{5+} (0.64 Å) compared to Ti^{4+} (0.605Å). The cell constants of the other 3C BNN-substituted phases are also larger than $BaTiO_3$, but show a progressive decrease with increasing y (right panel of **Figure 4.6**a) which again correlates with the average radius of the cations occupying the B-site. It should also be noted the trends in the lattice parameters are consistent with the nickel cations being in a 2+ state, the radius of Ni^{3+} (0.60 Å) is smaller than Ti^{4+} and would not induce an expansion in the cell volume. The results for the phase stabilities of the powder samples indicate the cubic 3C polymorph of $BaTiO_3$ can accommodate at least 0.83% $V_O^{\bullet\bullet}$ (sample E, $Ba(Ti_{0.9}Ni_{0.05}Nb_{0.05})O_{2.975}$) when co-doped with 5% Ni through a BNN end-member.

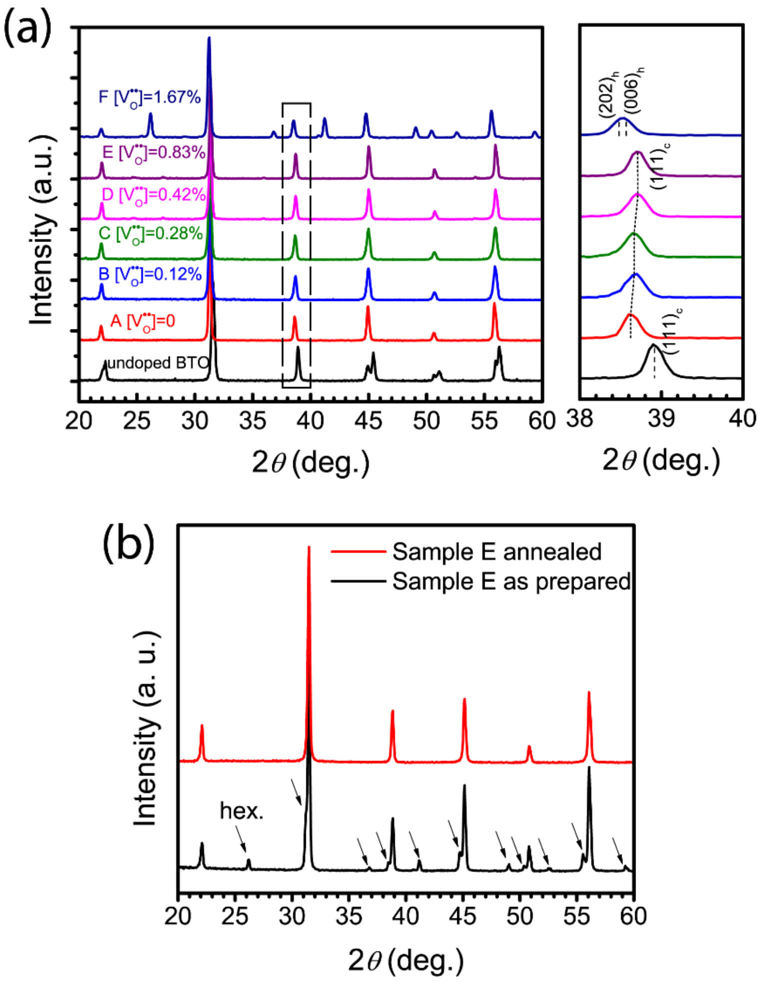

Figure 4.6 (a) XRD patterns of BNN-substituted $BaTiO_3$ with different nominal oxygen vacancy concentrations; see **Table 4-1** for compositional details. (b) XRD patterns of as-prepared and 1245 °C annealed sample E

Dense pellets of sample E, obtained by sintering the pre-calcined (1100 °C, 12 h) powder at 1450 °C, contained a 3C+6H phase mixture; however, a single phase 3C sintered pellet could be prepared at 1450 °C by using the annealed single-phase 3C powder as the green body. The microstructures of the two pellets are compared in **Figure 4.7**; the single phase 3C sample shows an even distribution of 3-8 μm grains, the two-phase pellet consists of ~30 μm plate-like 6H grains embedded in the finer-grain 3C matrix. Similar types of microstructure evolution have been observed for the 3C to 6H conversion in Zn/W co-doped $BaTiO_3$.[100] Analyses by energy dispersive spectroscopy showed the chemical composition of each grain in the 3C pellet are identical within the error of EDS, while the 3C+6H sample showed small variations from grain to grain.

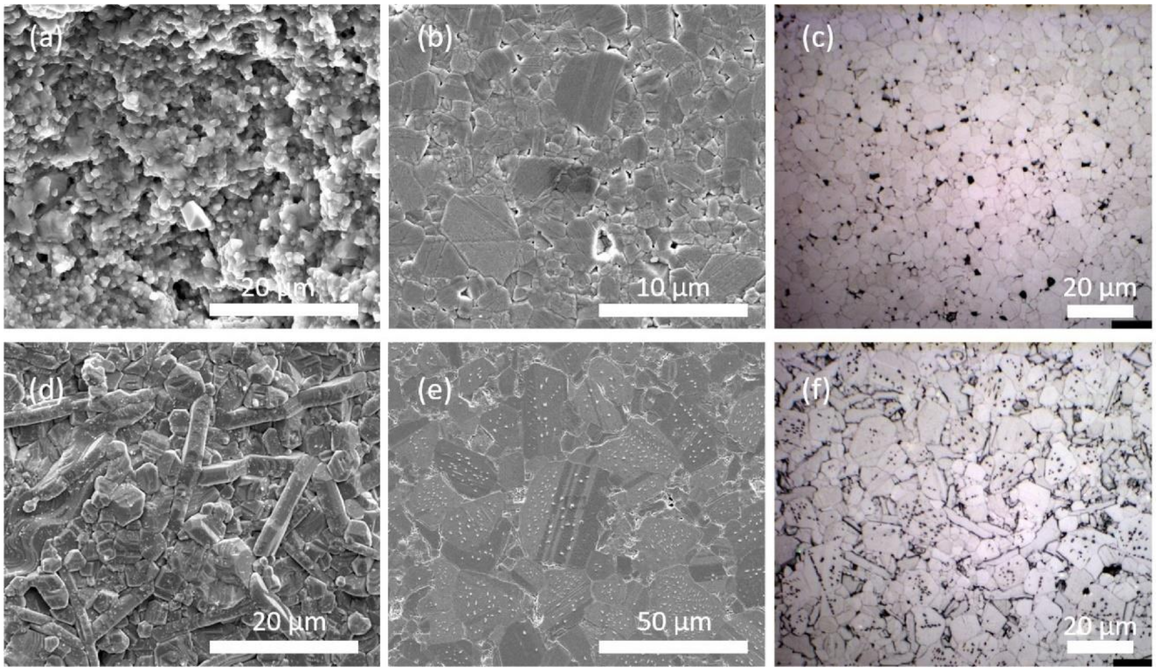

Figure 4.7 Microstructures of single-phase 3C annealed sample E: (a) SEM image of fracture surface; SEM (b) and optical microscopy images (c) of polished and thermally etched surfaces. Microstructures of the biphasic, 3C+6H as-prepared sample E: (d) SEM image of fracture surface; SEM (e) and optical microscopy images (f) of polished and thermally etched surface

4.4.2 Optical Response

UV-vis diffuse reflectance spectra of the BNN-substituted $BaTiO_3$ samples, **Figure 4.8**, show a systematic increase in the absorption between 380 nm to 1000 nm as the concentration of oxygen vacancies is increased. Because all the samples contain the same concentration of Ni^{2+}, it is apparent the visible light absorption can be controlled by engineering the oxygen vacancy content. Sample F, Nb-free $Ba(Ti_{0.95}Ni_{0.05})O_{2.95}$, has the highest absorption, however it has a 6H hexagonal structure that does not support ferroelectricity at room temperature. The Kubelka-Munk transformed spectra of the highest absorbing 3C structure [sample E, $(0.9)(BaTiO_3)$-$(0.1)(BaNi_{0.5}Nb_{0.5}O_{2.75})$], are shown in **Figure 4.9**a. Beginning at ~1.3 eV, the absorption in the visible range increases dramatically compared to undoped $BaTiO_3$ with a second absorption edge at 3.2 eV. Bandgaps extracted from a Tauc-type plot would yield a direct gap of 3.2 eV (**Figure 4.9**b) with an Urbach tail extending to 1.5 eV (see inset in **Figure 4.9**b) and an indirect gap of 1.25 eV (**Figure 4.9**c).

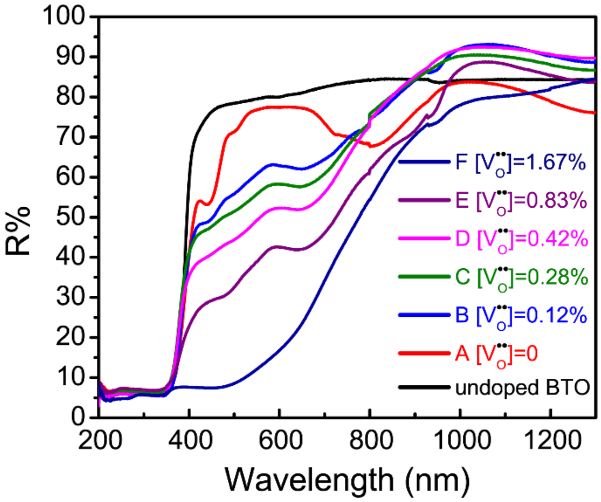

Figure 4.8 UV-vis diffuse reflectance spectra of BNN-substituted $BaTiO_3$.

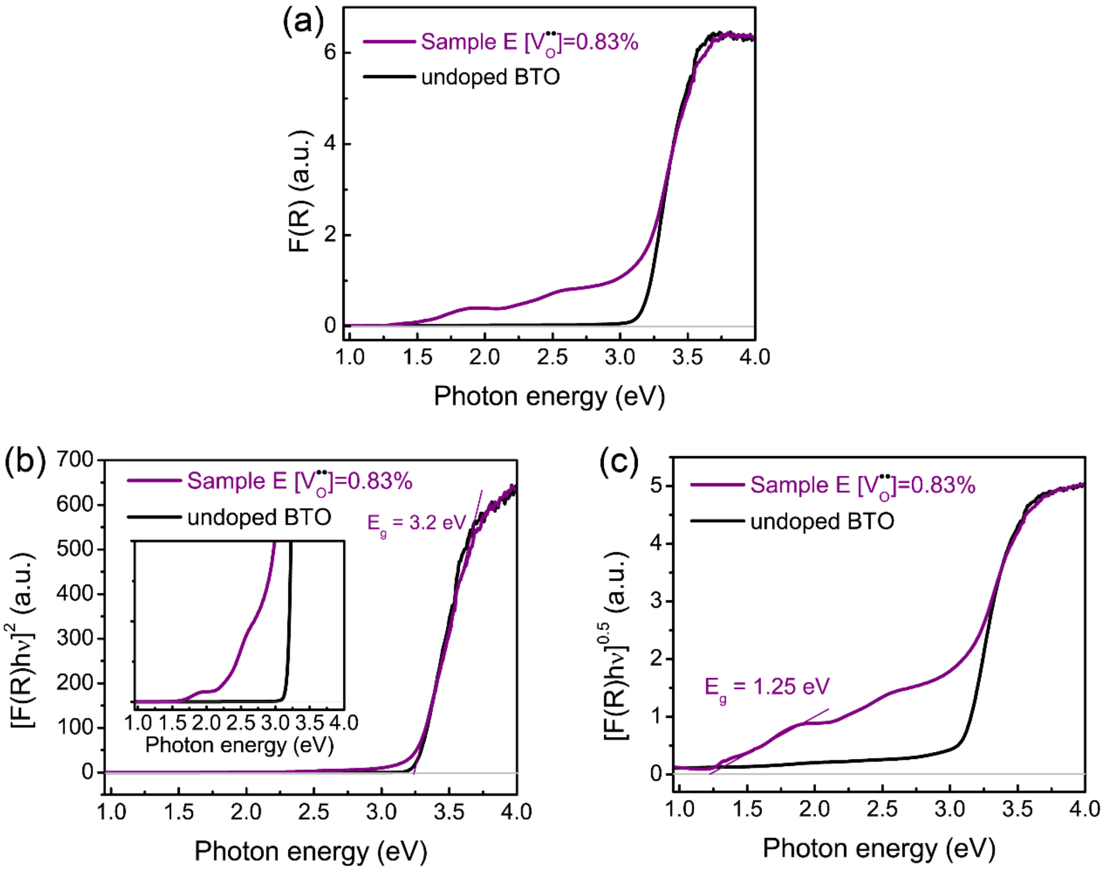

Figure 4.9 (a) Kubelka-Munk transformed function F(*R*) of sample E. (b) Direct bandgap Tauc plot; inset shows onset of optical absorption edge. (c) Indirect bandgap Tauc plot.

4.4.3 Ferroelectric Response

The ferroelectric properties of sample E were studied at different temperatures and frequencies. The *P-E* hysteresis loops were collected at 77 K and 300 K from a 145 μm thick sample with symmetric silver paste electrodes using four different frequencies (**Figure 4.10**a-b). At 300 K the sample shows very narrow loops with an almost linear response suggesting at best it is only weakly ferroelectric at room temperature. At 77 K the *P-E* loop was well defined with a remnant polarization $P_r \approx 5$ μC/cm^2 and coercive field $E_c \approx 12$ kV/cm. At both temperatures, the hysteresis loops were largely independent of the measuring frequency and essentially free of any leakage component associated with the lower bandgap.

Temperature dependent *P-E* loops were also collected in a probe station using an ITO(~100 nm)/FE-layer(107 μm)/Ag asymmetric electrode configuration designed for the photoresponse measurements (**Figure 4.10**c). The loops broaden with decreasing temperature; at 77 K saturation started to appear at $P_r \approx 2$ μC/cm^2 and $E_c \approx 5$ kV/cm, value that were smaller than those collected from the regular testing fixture due to the restricted field strength that could be applied in the probe station.

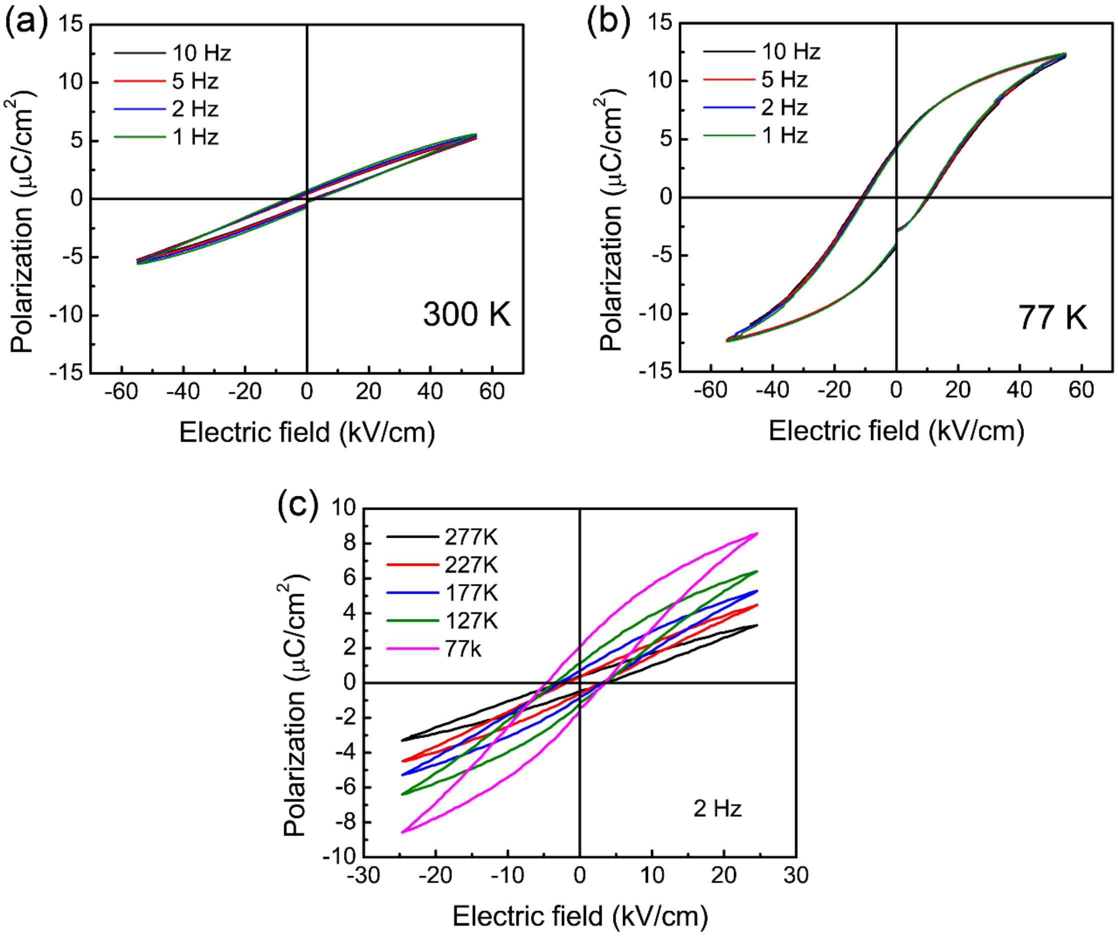

Figure 4.10 Ferroelectric P-E hysteresis loops of sample E. Frequency-dependent measurements of Ag/FE-layer (145 µm)/Ag geometry at (a) 300 K and (a) 77 K. (c) Temperature dependence of the ITO/FE-layer (107 µm)/Ag geometry measured in the probe station.

4.4.4 Photoresponse

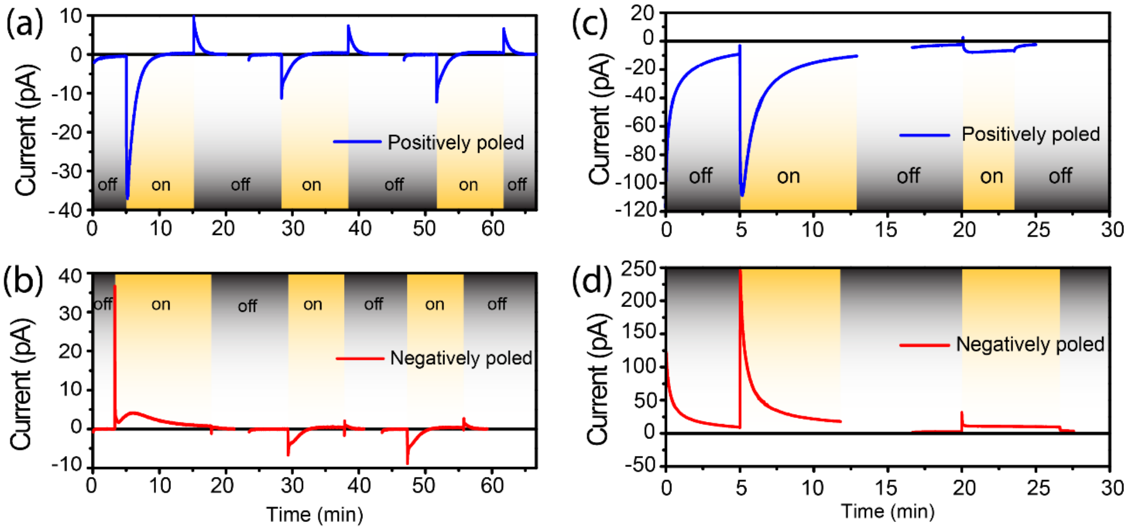

Figure 4.11 Photoresponses of positively poled (a) and negatively poled (b) sample E under AM1.5 at 77 K. Photoresponses of (c) positively poled and (d) negatively poled sample E under AM1.5 at 300 K.

Measurements of the photoresponse were made by poling sample E with a 268 V (25 kV/cm) pulse for 100 s at 77 K and exposure to AM1.5 illumination. **Figure 4.11**a-b shows the photocurrent versus time at zero bias under dark and illuminated conditions after positive and negative poling at 77 K. After poling no current was observed under dark conditions. For the positively poled sample the illumination induced a large negative current (–38 pA); however, this transient decayed and eventually changed sign to a small positive (0.5 pA) value. After the light was switched off, another transient current spike (10 pA) appeared and decayed to zero in the dark condition. The same photoresponse pattern was observed after re-illumination with smaller peak values and remained unchanged after 3 additional light on/off periods. After negative poling a positive current (38 pA) was observed after the initial illumination, the decay of the transient was faster than the positively poled sample but showed a similar reduction in magnitude after repeated modulation of the light. At 77 K, the direction of the poling only impacted the sign of the initial current spike after the first illumination, which flowed through the sample in a direction opposite to the ferroelectric polarization. Irrespective of the poling direction, the transient photoresponses of the second and third illumination periods were always negative when the light was switched on and positive when the light was turned off. In both cases no dark current was observed immediately after poling, implying negligible back switching or other relaxation processes.

The photoresponse measurements were repeated at 300 K, see **Figure 4.11**c-d. Positive poling induced an initial dark current (−120 pA) that decayed to −10 pA after 5 minutes before the light was turned on. The transient dark current was only observed at 300 K and could arise from incomplete discharging after poling and/or back diffusion of mobile ions or vacancies; similar effects have been reported organic-inorganic hybrid perovskite polycrystalline solar cells.[101] The first application of light induced a transient current spike with a peak value of −110 pA; this transient was not present in subsequent illuminations where a slow decaying, quasi-steady-state photocurrent of −10pA (−8 nA/cm^2) was observed. The value of this photocurrent is higher than that reported for a $BaTiO_3$ + 5 wt% $CaTiO_3$ ceramic (~ 2 nA/cm2) under 100 mW/cm^2 of 403 nm illumination and 0.25%Mn-doped $BaTiO_3$ single crystals (0.285 nA/cm^2) under 14 mW/cm^2 halogen lamp illumination.[102,103] The direction of the photocurrent was reversed when the poling direction was switched, consistent with a ferroelectric photovoltaic effect. In contrast to the 77 K measurements, where the current reversal only occurred during first illumination, the photoresponse at 300 K showed consistent switchability during subsequent exposures of light.

The reasons for the differences in the 77 K and 300 K photoresponses are unclear as there could be several contributing factors. The ferroelectric polarization should dictate the direction of the photocurrent and this was the case for the first illumination at 77 K and all the photo-excitations at 300 K. The change in the photoresponse of the subsequent 77 K measurements could arise from a Schottky barrier at the ITO - ferroelectric interface; it is also possible the formation of a space charge region during poling could mediate the currents at 300 K. For a polycrystalline ferroelectric with numerous grain and domain boundaries it is difficult to unambiguously relate the reversible photoresponse to the ferroelectric polarization or to a bulk photovoltaic effect. During poling the electromigration of $V_O^{\bullet\bullet}$ could cause accumulation at the grain boundaries where the resultant space charge[97] could separate excited charge carriers throughout the sample in a forward or reverse direction determined by the poling voltages.

4.5 Conclusions

The phase stability, optical absorption, ferroelectric and photovoltaic responses of the $Ba(Ti_{1-x}Ni_x)O_{3-x}$ and $(1-x)BaTiO_3$-$(x)[(1-y)Ba(Ni_{1/3}Nb_{2/3})O_3$-$(y)$“$BaNiO_2$”] systems were investigated to elucidate their potential for applications in solar energy generating devices. The Ni^{2+}-$V_O^{\bullet\bullet}$ pair is identified as the main factor in determining the phase stability and absorption properties of both systems. Although Ni^{2+}-$V_O^{\bullet\bullet}$ stabilizes a hexagonal 6H phase at high temperature, $Ba(Ti_{0.99}Ni_{0.01})O_{2.99}$ and $(0.9)(BaTiO_3)$-$(0.1)(BaNi_{0.5}Nb_{0.5}O_{2.75})$

can be transformed to a single-phase 3C structure by post-annealing. By controlling the Ni to Nb ratio and therefore the $V_O^{\bullet\bullet}$ concentration, the optical absorption can be tuned to values between 1.3 eV to 3.2 eV suitable for potential ferroelectric photovoltaic applications. $Ba(Ti_{0.99}Ni_{0.01})O_{2.99}$ and $(0.9)(BaTiO_3)$-$(0.1)(BaNi_{0.5}Nb_{0.5}O_{2.75})$ show saturated hysteresis loops at room temperature and 77 K respectively. By alternating the direction of the poling voltage, a reversible transient photoresponse (38 pA) at 77 K was observed for $(0.9)(BaTiO_3)$-$(0.1)(BaNi_{0.5}Nb_{0.5}O_{2.75})$ with a reversible steady state photoresponses of 3 pA for $Ba(Ti_{0.99}Ni_{0.01})O_{2.99}$ and 10 pA for $(0.9)(BaTiO_3)$-$(0.1)(BaNi_{0.5}Nb_{0.5}O_{2.75})$ at 300 K under a AM1.5 light source. These results compare favorably to the photoresponses previously reported for $BaTiO_3$ + 5 wt% $CaTiO_3$ ceramics and Mn-doped $BaTiO_3$ single crystals[102],[103]. The controllable absorption properties of Ni and Ni-Nb substituted $BaTiO_3$ make these systems appropriate candidates for optimization of their ferroelectric and photovoltaic responses in thin film form.

Chapter 5 $PbTiO_3$-$BiFeO_3$-$Bi(Ni_{1/2}Ti_{1/2})O_3$ System

5.1 Introduction

In this chapter we explore potential new photovoltaic materials, preparable in ceramic form, that combine a large polarization with a reduced and tunable bandgap. This part of the thesis was recently published in *Chemistry of Materials*, 31(11), 4184–4194 (2019) [reprinted (adapted) with permission from American Chemical Society] and this chapter follows the format of the published paper with small alterations; the supplementary materials are attached in the Appendix.

In an attempt to maintain a high polarization, we investigated a (Pb, Bi)-based pseudo-ternary system where one of the component binaries, $PbTiO_3$-$BiFeO_3$ (PT-BF), exhibits enhanced tetragonality with a high T_C. BF is one of a few solid solution additives that increase the c/a ratio of PT[104–107] and the substitution also reduces the bandgap.[108] However, highly tetragonal PT-BF ceramics are not practical for bulk ferroelectric applications due to the large coercive field and the large internal strains accompanying the paraelectric to ferroelectric transition which cause cracking during cooling.[109] To mitigate these issues we focused on solid solutions of PT-BF with a third component, $Bi(Ni_{1/2}Ti_{1/2})O_3$ (BNT), that could induce an MPB and maintain a high T_C and low bandgap. The choice of BNT was guided by previous theoretical[58,91] and experimental[16,46,48,49,73] studies that show Ni^{2+} is effective in lowering the E_g of titanate and niobate perovskites, while the occupancy of Ti^{4+} on the remaining B-sites and Bi^{3+} on the A-sites can promote polar distortions. Although pure BNT can only be stabilized in a perovskite form at high pressure,[110] an extensive range of solid solutions with PT up to 65% BNT can be prepared at 1 atm. The previous studies also showed the PT-BNT pseudo-binary forms an MPB between ~ 51-55% BNT with a T_C (≈ 670 K) that is higher than the Pb(Zr,Ti)O_3 system;[111–114] there are no reports on the optical absorption properties of this system.

Here we investigate the structural, ferroelectric and optical properties of the PT-BF-BNT ternary system and the photovoltaic response of compositions at the MPB. The ternary shows bandgaps ranging from 3.2 to 1.75 eV and the MPB compositions retain a substantial P_r (> 32 μC/cm^2) with switchable, linear photovoltaic *IV* responses and above-bandgap open circuit voltages (V_{oc}). The wavelength dependence of the light-induced response shows a correlation between the photocurrent and the bandgap, and under 1 sun AM1.5 G illumination the photovoltaic performance (*e.g.* V_{oc} = 5 V; j_{ph} = 0.09 μA/cm^2) of the MPB compositions exceeds most previously reported ferroelectric oxide ceramics.

5.2 Synthesis Details

The synthesis of the PT-BF-BNT solid solutions followed the standard procedures described in Section 2.1. The stoichiometric raw mixtures were first calcined at 650 °C for 6 hours. This calcination temperature is chosen to avoid the easily formed liquid phases of Bi containing compounds. Multiple calcinations were carried out to achieve single phase purity prior to sintering. Green bodies of PT-BF-BNT were sintered for 2 hrs at temperatures between 975 to 1050 °C according to the composition; samples containing higher BF content requires lower sintering temperature.

5.3 $PbTiO_3$-$BiFeO_3$ pseudo-binary

The phase stability of the (x)PT-(1–x)BF solid solutions was investigated over the entire range of composition using XRD (**Figure 5.1**a). All compositions showed single-phase perovskite patterns except $BiFeO_3$, which contained small amounts of $Bi_{25}FeO_3$ and $Bi_2Fe_4O_9$ secondary phases (see full scans in Figure A.1 of Appendix A). At room temperature the solid solution retains a PT-type structure from $0.3 < x < 1.0$ and the tetragonality, as manifested by the splitting of the $(001)_T/(100)_T$ and $(011)_T/(110)_T$ peaks, increased with decreasing x. From the calculated lattice parameters (Table A.1 in Appendix A), at $x = 0.3$ $c/a = 1.19$, which is consistent with literature data.[115] The compositions with the highest tetragonality (*i.e.* $x = 0.3$ and 0.325) also form a metastable rhombohedral phase when the particle size is small (≤ 1 μm).[116] The details of the stabilization of the different phases are described in Appendix A Figure A.2. For $x \leq 0.2$, the tetragonal reflections completely transform to the rhombohedral peaks, $(102)_R$ and $(104)_R/(110)_R$, and as reported previously a region of two-phase coexistence is observed between $0.2 < x < 0.3$.[117]

The optical absorption of the (x)PT-(1–x)BF samples was investigated by diffuse reflectance spectroscopy and the resultant Kubelka-Munk function $F(R)$ (**Figure 5.1**b) contains two principle features. The first is a strong absorption edge followed by a plateau extending up to 6 eV, which is present for all compositions. This excitation, which defines the E_g of (x)PT-(1–x)BF, is caused by charge transfer from the oxygen 2p states at the valence band maximum to the transition metal (*e.g.* Ti^{4+} or Fe^{3+}) 3d states at the conduction band minimum. The onset of this fundamental absorption edge is red-shifted from ~3 eV to 2.2 eV by the substitution of $BiFeO_3$ into $PbTiO_3$. The second feature is the appearance of broad and weak absorption peaks below 2.2 eV for $BiFeO_3$-rich compositions; these result from localized Fe^{3+} *d-d* transitions due to the crystal field (see Appendix A Figure A.3), they are forbidden by the Laporte rule and do not contribute to the photoconduction.

The fundamental absorption edge of the (x)PT-(1–x)BF spectra was analyzed using Tauc plots to quantify the magnitude of the direct and indirect optical gap. Details of the line fits for the Tauc plots are provided in Appendix A Figure A.4 and the variation of the optical E_g with x is shown in **Figure 5.1**c**.** The absorption edge of the tetragonal compositions ($x \geq 0.3$) is well-fitted by a single allowed direct transition, resulting in a decreased direct E_g as the tetragonality increases. The rhombohedral compositions ($x < 0.3$), especially $BiFeO_3$, show two distinct direct transitions. The first transition at higher energy is in agreement with the frequently reported E_g of 2.7 eV for $BiFeO_3$ films obtained by spectroscopic ellipsometry[61,62]. The second lower energy transition is more likely due to a combination of high energy crystal-field excitations and exciton bands[64,118–120] (see Figure A.3 and Figure A.4 in Appendix A). The tetragonal compositions with $x \geq 0.4$ also show a well-defined linear region in the indirect Tauc plot; however, for $x \leq 0.3$ the strong overlap of the *d-d* transitions and the charge transfer absorption edge prevent any satisfactory fitting for an indirect transition. It should be noted that the lowest direct E_g (= 2.18 eV) is observed in the composition (x = 0.3) with the highest tetragonality and the transformation to the rhombohedral phase fundamentally alters the electronic structure of the (x)PT-(1–x)BF solid solution.

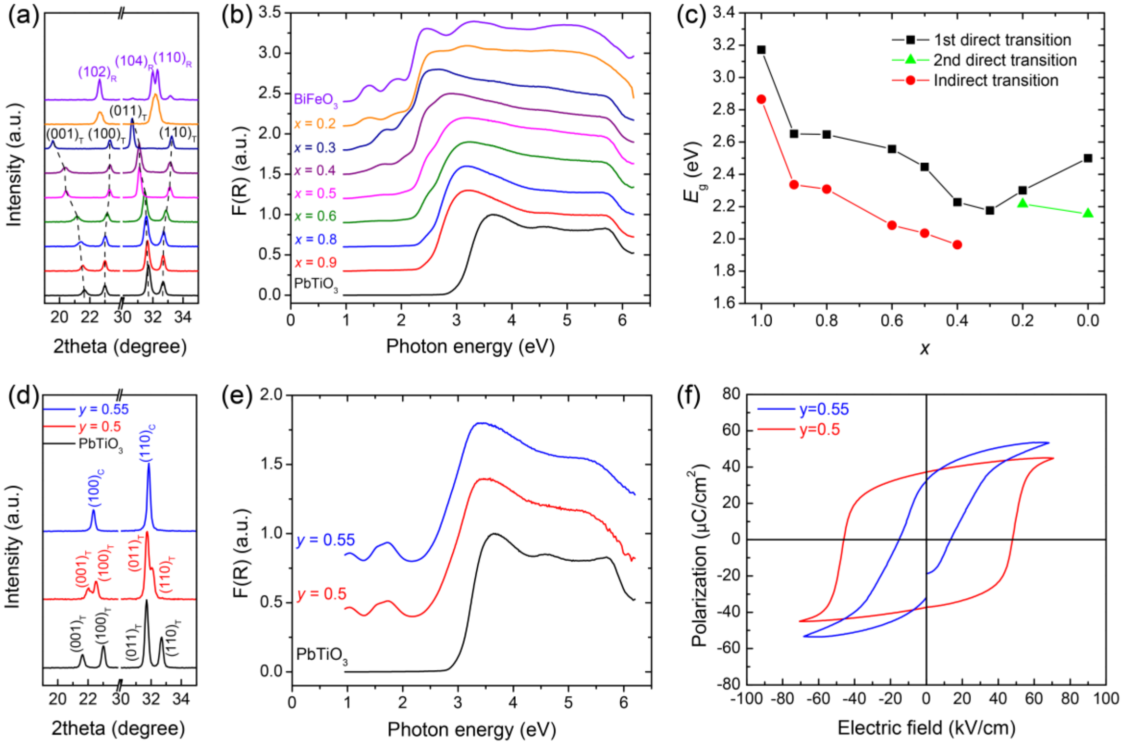

Figure 5.1 (*x*)PT-(1−*x*)BF solid solutions: (a) XRD patterns; (b) Kubelka-Munk spectra; (c) optical bandgap. (1−*y*)PT-(*y*)BNT solid solutions: (d) XRD patterns; (e) Kubelka-Munk spectra; (f) ferroelectric hysteresis loops measured at 1 Hz.

5.4 $PbTiO_3$-$Bi(Ni_{1/2}Ti_{1/2})O_3$ pseudo-binary

$Bi(Ni_{1/2}Ti_{1/2})O_3$ (BNT), which has a balance of ferroelectrically active Ti^{4+} and gap-lowering Ni^{2+} cations on the B-site, was chosen to modify the tetragonal (*x*)PT-(1–*x*)BF solid solutions through formation of an MPB. First the (1–*y*)PT-(*y*)BNT pseudo-binary was explored to quantify the effect of the BNT additive on the structure and ferroelectric and optical properties of lead titanate. The splitting of the $(001)_T/(100)_T$ and $(011)_T/(110)_T$ reflections in the XRD patterns of the solid solution (**Figure 5.1**d) is reduced up to $y = 0.5$; their replacement by pseudocubic $(100)_C$ and $(110)_C$ peaks at $y = 0.55$ confirms the previously reported location of the MPB.[112]

The diffuse reflectance spectra (**Figure 5.1**e) show the substitution of BNT also causes a shift in the onset of the absorption edge, from 3 eV for pure $PbTiO_3$ to ~2.5 eV for y = 0.5 and 0.55; these compositions have almost identical absorption spectra with weaker additional peaks appearing below 2 eV. The weaker peaks are associated with localized *d*-*d* transitions for octahedral complexes of Ni^{2+} and can be attributed to $^3A_{2g}$ to $^3T_{2g}$ and $^3A_{2g}$ to $^3T_{1g}$ transitions through a Tanabe-Sugano diagram.[121] The Tauc plots (Figure A.5 in Appendix A) yield a direct and indirect gap of 2.85 eV and 2.2 eV for both y = 0.5 and 0.55 samples.

In contrast to their similar optical absorption, the ferroelectric response of the y = 0.5 and 0.55 ceramics (**Figure 5.1**f) are very different, as expected for compositions close to an MPB. Tetragonal y = 0.5 has a well-saturated hysteresis loop with a coercive field E_c = 50 kV/cm and P_r = 38 μC/cm^2; the loop for pseudocubic y = 0.55 is more slanted with E_c = 18 kV/cm and P_r = 32 μC/cm^2. The large reduction of E_c at y = 0.55 is consistent with the lower barrier to domain switching in the pseudocubic MPB phase.

5.5 $PbTiO_3$-$BiFeO_3$-$Bi(Ni_{1/2}Ti_{1/2})O_3$ ternary compositions

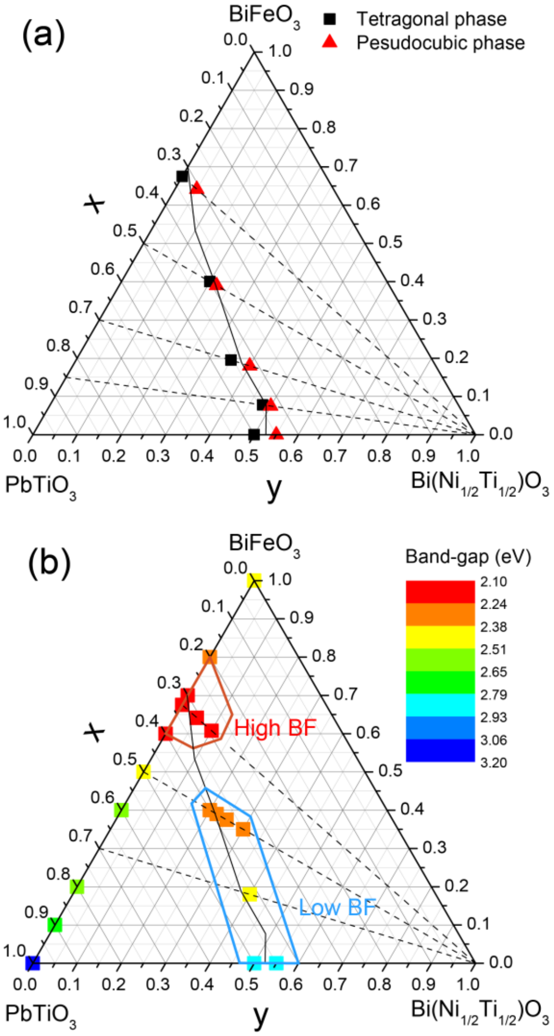

Figure 5.2 (a) Schematic of the (1–*y*)[(*x*)PT-(1–*x*)BF]-(*y*)BNT pseudo-ternary phase diagram. Dashed lines represent tie-lines explored to monitor the changes in structure and properties; the resultant MPB is marked by the solid line. Detailed XRD and ferroelectric data along each tie-line are provided in **Figure A.6**. (b) color map of the measured direct bandgaps. The MPB regions with high and low BF content are indicated

The evolution of the MPB in the $PbTiO_3$-$BiFeO_3$-$Bi(Ni_{1/2}Ti_{1/2})O_3$ ternary was investigated by synthesizing samples in the vicinity of the tie line connecting the MPB in the (*x*)PT-(1–*x*)BF ($x = 0.27$) and (1–*y*)PT-(*y*)BNT ($y = 0.55$) pseudo-binaries.

Compositions were prepared along tie-lines from BNT to (x)PT-(1–x)BF with $x = 0.85$, 0.7, 0.5 and 0.325 (**Figure 5.2**); the MPB was identified by locating the transition from tetragonal to pseudocubic symmetry in the XRD patterns and from the reduction of E_c in the ferroelectric hysteresis loops (Figure A.6 in Appendix A). For the $x = 0.325$ tie-line the transition from tetragonal to pseudo-cubic could be observed in the XRD patterns, however, the higher conductivity of the $BiFeO_3$-rich ceramics prevented any significant ferroelectric switching for electric fields up to 70 kV/cm (Figure A.6 in Appendix A). The difficulty in switching $BiFeO_3$-containing ceramics due to their conductivity and/or domain wall clamping from the ordered alignment of Fe^{2+}-oxygen-vacancy defect dipoles, has been reported in many other studies.[122–124] The location of the ternary MPB deduced from the structural and ferroelectric responses of the samples is shown in **Figure 5.2**a.

The optical absorption properties of the PT-BF-BNT system were analyzed through Tauc plots and the extracted direct E_g of various compositions is shown in **Figure 5.2**b; the corresponding values for an indirect gap are presented in Figure A.7 in Appendix A. BF and BNT are both effective in reducing the charge transfer gap of the solid solutions, resulting a continuously tunable E_g ranging from 3.2 eV to 1.75 eV. The tunability could potentially enable optimization for applications in multi-junction solar cells as previously shown in other perovskite oxide[51] and halide systems.[125,126] For the $x = 1$, 0.7, and 0.5 compositional lines, the substitution of BNT into (x)PT-(1–x)BF can further reduce the charge transfer gap through the broadening of the localized Ni $3d$ e_g states to the conduction band minimum.[127] Along the $x = 0.325$ line the increasing BNT content produces a slight blue-shift in the absorption edge (see Figure A.8 in Appendix A) due to an abrupt change in structure from highly tetragonal to pseudocubic (Figure A.6 in Appendix A); this increase in the gap is similar to the effect of the structure change on the bandgap observed at x = 0.3 and 0.325 in the (x)PT-(1–x)BF pseudobinary (Figure A.2 in Appendix A). These observations indicate the MPB in the high and low BF regions marked in **Figure 5.2**b are different in terms of the evolution of electronic structures for compositions across the MPB.

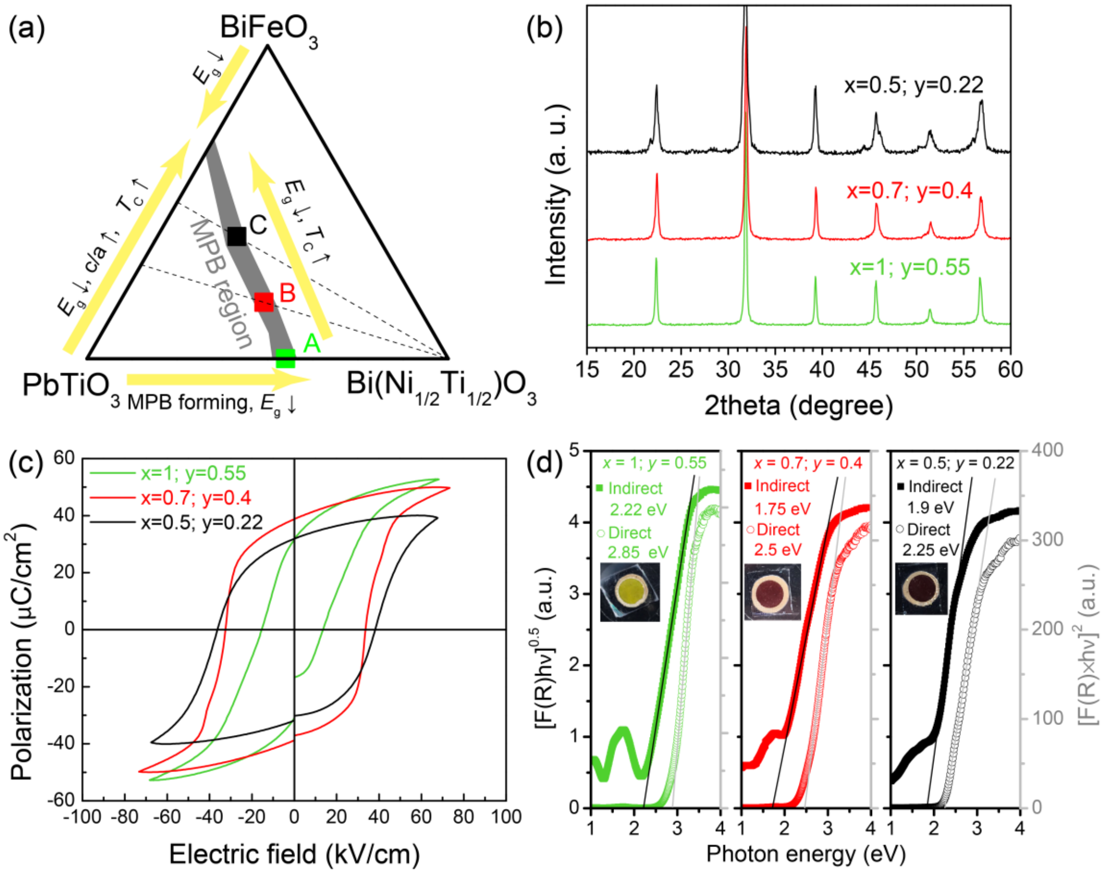

Figure 5.3 Structure, optical and ferroelectric properties of the MPB compositions selected for detailed investigation in the (1–y)[(x)PT-(1–x)BF]-(y)BNT ternary: (a) locations of compositions A (x = 1, y = 0.55), B (x = 0.7, y = 0.4) and C (x = 0.5, y = 0.22) and a summary of the property variations across the system; (b) XRD patterns; (c) ferroelectric hysteresis loops; (d) Tauc plots used for bandgap calculations, images of the polished surfaces of each sample are inset.

Three representative compositions, “A”: $(Pb_{0.45}Bi_{0.55})(Ni_{0.275}Ti_{0.725})O_3$ ($x = 1$, $y = 0.55$); “B”: $(Pb_{0.42}Bi_{0.58})(Fe_{0.18}Ni_{0.20}Ti_{0.62})O_3$ ($x = 0.7$, $y = 0.4$); and “C”: $(Pb_{0.39}Bi_{0.61})(Fe_{0.39}Ni_{0.11}Ti_{0.50})O_3$ ($x = 0.5$, $y = 0.22$), were selected to investigate the evolution of the structure and properties in the vicinity of the MPB in the pseudo-ternary (**Figure 5.3**a). The XRD patterns, ferroelectric response, and Tauc plots of these MPB compositions are shown in **Figure 5.3**b, c, and d respectively. The XRD patterns show pseudo-cubic structures for A and B; composition C has a main pseudo-cubic phase with a trace amount of a tetragonal structure. The ferroelectric hysteresis loops of the three compositions are well saturated with minimal contributions from conductivity. As the BF content along the MPB increases, E_c also increases while the saturation polarization decreases, indicating the domain switching is harder in $BiFeO_3$-rich compositions. The range of P_r values, 32 to 39 $\mu C/cm^2$, exceeds those previously reported for compositions lying in the tetragonal phase field of the PT-BF-BNT system.[128] The Tauc plots show a reduction in the direct gap along the MPB with increasing BF content and this leads to a strong variation in the color of the samples (inset **Figure 5.3**d) from green (A) to red (B) to almost black (C). However, it should be noted that composition B shows the smallest indirect $E_g = 1.75$ eV and the largest difference in the value of the direct and indirect gaps. The combination of a narrow bandgap and a large P_r for the ternary PT-BF-BNT MPB compositions compares favorably to those previously reported for other ferroelectric ceramic photovoltaic systems (Figure A.9 in Appendix A). These MPB compositions also maintain T_C’s, ranging from ~ 670 K to 850 K, that are among the highest reported for a photovoltaic ferroelectric oxide (the dielectric data is provided in Figure A.10 in Appendix

A), potentially allowing high temperature applications. Their photovoltaic performance is assessed in the following section.

5.6 Photovoltaic Properties of MPB Compositions

5.6.1 Switchability and Above-bandgap V_{oc}

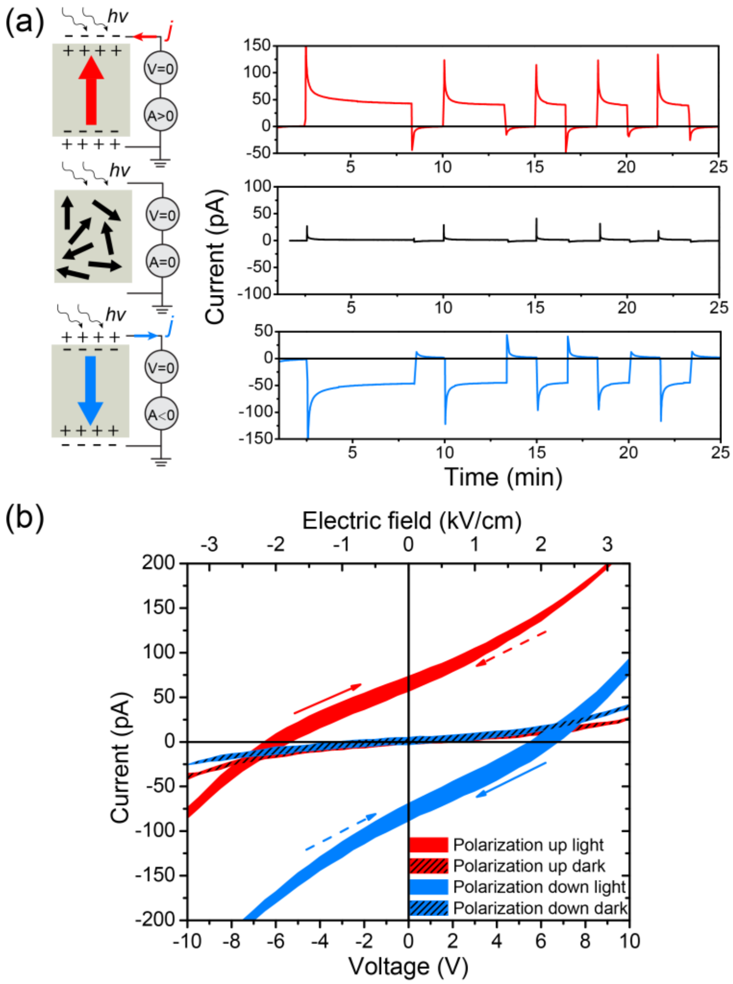

Figure 5.4 Photoresponse, switchability and *IV* characteristics of composition B (x = 0.5, y = 0.4) under 450 nm laser illumination. (a) Top: photocurrents for laser on/off cycles after negatively poling (polarization up); middle: non-poled state; bottom: after positive poling (polarization down). (b) *IV* response of oppositely poled states in the dark and under illumination; solid arrows indicate the direction of the forward sweep, dash arrows the backward sweep.

The photovoltaic properties of the MPB compositions A, B, and C were measured using an ITO/FE-layer/Ag device structure (see Figure A.11 in Appendix A). The electrode materials were deliberately chosen to reduce the difference in the work function of the top and bottom electrodes; the work functions for polycrystalline silver and ITO are ~4.3 eV and ~4.5 eV respectively.[31] Composition B (direct E_g = 2.5 eV; P_r = 39 μC/cm^2) is representative in illustrating the polarization-modulated photovoltaic response under above-bandgap monochromatic illumination (450 nm, ~50 mW/cm^2) (see Figure A.12 in Appendix A for the response of composition C). The sign of the measured current is defined as positive for current flow from the top to bottom electrode through the ferroelectric layer. In the virgin state (*i.e.* before poling), under zero bias composition B does not shown any significant response with the light on or off (middle panel **Figure 5.4**a) except for a small transient current spike triggered by turning on the laser, which immediately decays to a negligible steady-state photocurrent. The absence of a steady-state current in the virgin state rules out any significant contribution to the photoresponse from ferroelectric imprint effects and/or asymmetrical Schottky barriers.

The sample was then positively poled at 300 K using a 300 s, 200 V step-like voltage pulse. During poling the area under the top electrode showed a clear shape change (see Figure A.11 in Appendix A), indicating a strong electromechanical response in the sample. After positive poling, a significant photocurrent was induced in a direction opposite to the ferroelectric polarization (top panel, **Figure 5.4**a). Multiple light on/off cycles gave reproducible patterns for the photocurrent. The same area of the sample was then negatively poled and, in accordance with the switching of the ferroelectric polarization, under the same illumination conditions the polarity of the photocurrent was reversed in a symmetric manner (bottom panel **Figure 5.4**a). The switchable photoresponse clearly demonstrates the concurrence of the bulk polarization and the photovoltaic effect.

The *IV* responses of composition B with up and down polarized states were studied to elucidate the distinct features of the observed photovoltaic effect (**Figure 5.4**b). The *IV* curves were collected using a slow voltage sweep rate (0.05 V/s) to achieve quasi-steady-state currents at each voltage and minimize hysteresis from the capacitor component of the circuit. The dark *IV*s of the up and down poled states pass through the origin and their linear response between ±10 V shows there is no significant contribution from domain back-switching or electromigration of mobile defects, ensuring an equilibrium polarization during the sweep. Under illumination the *IV* response of the up/down poled states were quite different to conventional photovoltaics where the built-in electric field inside the heterojunctions and Schottky barriers provides the driving force for carrier separation. Firstly, similar to the photocurrent versus time measurements, the polarity of the *IV* curve is switched after reversal of the polarization. Secondly, the *IV* curves of the oppositely poled states are nearly symmetrical with the same absolute value of the open circuit voltage (6 V), which is equivalent to a photogenerated electric field E_p = 2 kV/cm (below the coercive field E_c = 35 kV/cm), and slightly different absolute values of the short circuit current (65 pA and 80 pA for polarization up and down respectively). The difference can be explained by the polarization-induced modification of the Schottky barriers, which combines with the bulk contribution to produce the overall photovoltaic response. A more detailed analysis of the band bending at the electrode interfaces is provided in the supplementary material (see Figure A.13 in Appendix A). Thirdly, the 6 V V_{oc} (obtained from the median value of the forward and reverse sweeps) is multiple times larger than the bandgap of the composition (E_g = 2.5 eV), which is not possible in a traditional single junction solar cell. These observations are consistent with the BPVE model in which the built-in electric field is not required for carrier separation and the V_{oc} is not limited by the bandgap.

To further clarify the origin of the high open-circuit voltage, it is useful to compare these results to the above-bandgap V_{oc} reported for the non-ferroelectric polycrystalline hybrid perovskite, $CH_3NH_3PbI_3$. In that system the high V_{oc} has been attributed to the granular nature of the polycrystalline films and the series connection of multiple sub-cells through inter-grain tunneling junctions.[101] The formation of a tunneling junction in $CH_3NH_3PbI_3$ results from the accumulation of a substantial number of mobile charged ions at grain boundaries during poling. However, the likelihood of a significant contribution from a tunneling junction mechanism in our samples is very low as the activation energy for ion migration in perovskite oxides, even those considered as good oxygen conductors, is typically at least one order of magnitude higher than the hybrid perovskites.[129,130] This conclusion is supported by additional measurements made at 173 K where a very large above-bandgap V_{oc} = 10 V was observed at a temperature where any ion migration is extremely unlikely during poling (Figure A.14 in Appendix A). This comparison points to a mechanism where the anomalous V_{oc} devices is caused by the BPVE associated with the absence of crystal inversion symmetry and/or ferroelectric-related boundary effects that do not rely on ion migration.

5.6.2 Wavelength dependence

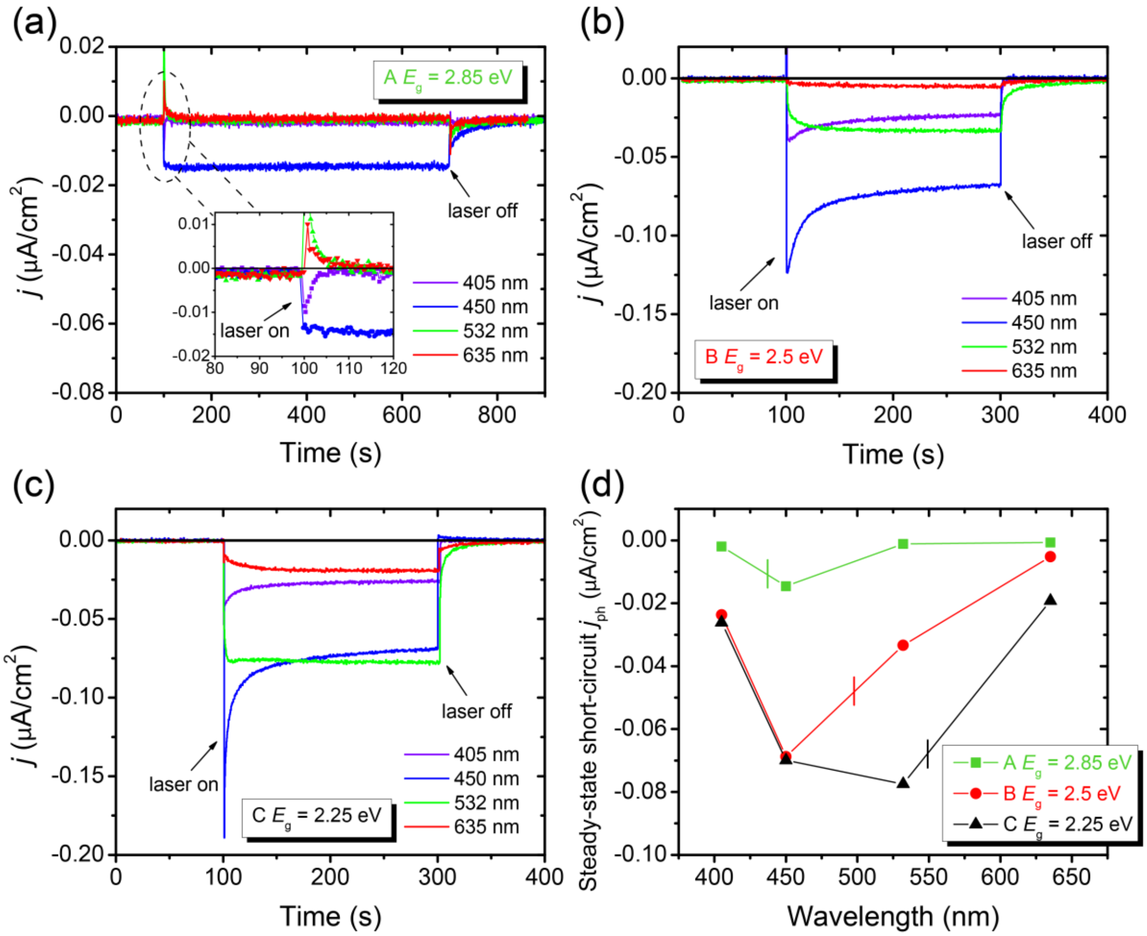

Figure 5.5 Photo-induced responses of (a) composition A (x = 1, y = 0.55; direct E_g = 2.85 eV), (b) B (x = 0.7, y = 0.4; direct E_g = 2.5 eV) and (c) C (x = 0.5, y = 0.22; direct E_g = 2.26 eV) under monochromatic illumination of various wavelengths; (d) spectral dependence of steady-state photocurrents of A, B and C (vertical markers indicate optical bandgap of each composition).

To determine how the photoresponse is affected by the evolution of the bandgap along the ternary MPB, spectroscopic analyses of the photocurrent under zero bias were conducted on samples A, B and C under different excitation wavelengths (405 nm, 450 nm, 532 nm, 635 nm). All samples were poled to a "polarization down" state prior to measurement. Composition A (x = 1, y = 0.55; direct E_g = 2.85 eV) shows the smallest photoresponse (**Figure 5.5**a) due to the larger E_g and partial depolarization as evidenced by the gap in the hysteresis loop (see **Figure 5.3**c). In this sample a significant steady-state photocurrent density (j_{ph}), 0.015 μA/cm^2 was only observed under 450 nm illumination, which is close to the value of the direct gap. Wavelengths below (532 nm and 635 nm) and above (405 nm) the direct gap produced a transient response that eventually decayed to a negligible steady-state photocurrent (inset **Figure 5.5**a). The transient response was wavelength dependent and the spikes for below- and above-bandgap illumination have opposite polarity. In ferroelectric materials, transient photoresponses that eventually equilibrate to steady state values are frequently attributed to pyroelectric currents originating from the heating of the sample under illumination;[26,131] however, this would not explain the change in the polarity of transient spikes that we observe at the different wavelengths.

The wavelength dependence of the photocurrent is more prominent in compositions B and C, which have a larger P_r and narrower direct E_g. For composition B (x = 0.7, y = 0.4; direct E_g = 2.5 eV) all wavelengths produce a larger negative j_{ph} (**Figure 5.5**b) compared to composition A. The above-bandgap illumination (405 nm and 450 nm) induced a transient spike which decays to the steady state current, while the below-bandgap illumination (532 nm and 635 nm) produced a current that gradually increases to the steady state value. Considering the change in the polarity of the transient spikes observed for sample A, the photoresponse of composition B can be treated as a superposition of a transient spike which decays to zero and a steady-state step function. The transient is likely related to a surface recombination process,[132] while the steady-state response results from the BPVE.[133] Composition C (x = 0.5, y = 0.22; direct E_g = 2.25 eV) yielded a similar photoresponse to its sample B counterpart, however the steady-state currents under long-wavelength illumination (532 nm and 635 nm) were larger (**Figure 5.5**c). The near-bandgap illumination (532 nm) yielded an instantaneous establishment of the largest steady-state j_{ph} (= 0.078 μA/cm^2) consistent with a fast band-band excitation without trapping or thermal activation processes from levels within the bandgap.[133] The variation of the photoresponse with wavelength is commonly used as an alternative method for determining the bandgaps of semiconductors.[134] The observation of a sharp maximum at the absorption edge is not unusual; the decrease in the photoresponse at longer wavelengths is due to the decrease in the excitation of free carriers, while for wavelengths below the maximum the photocurrent is limited by the reduced penetration depth (0.1 µm assuming an absorption coefficient of ~10^5 cm^{-1} for above-bandgap illumination)[61] with the radiation largely being absorbed near the surface where rapid carrier recombination can occur.

If the steady-state photocurrents for the three MPB compositions are plotted as a function of the illumination wavelength (**Figure 5.5**d**),** it is apparent the near-bandgap illumination stimulates the highest response. This is potentially due to the combined result of strong band-band excitation and a good match between the absorption depth and sample thickness for the near-bandgap illumination. Composition C, which has the narrowest direct E_g, generates the largest photocurrent under all the wavelengths used in this study. Furthermore, samples B and C are among the few ferroelectric oxides (*e.g.* KBNNO[46] and

BiFeO$_3$[11,135]) that show a steady-state photovoltaic effect for wavelengths larger than 600 nm.

5.6.3 Performance under 1 Sun AM 1.5 G Illumination

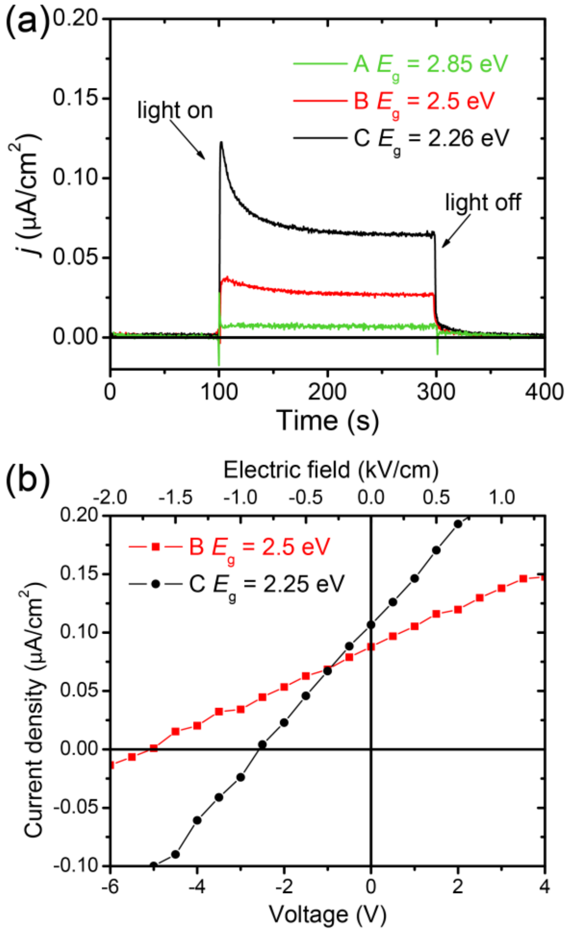

Figure 5.6 (a) Photoresponses and (b) *IV* responses of MPB compositions under 1 sun AM1.5 G.

The photoresponse of the MPB samples was also measured under 1 sun AM1.5 G conditions; as expected, the photocurrents (shown in **Figure 5.6**a for a “polarization up” state) increase with decreasing bandgap. The photovoltaic *IV* characteristics of B and C (**Figure 5.6**b) were quantified by averaging the forward and reverse sweeps. Both compositions show a linear *IV* response with an above-bandgap V_{oc}: for B, V_{oc} = 5.0 V (E_p

= 1.7 kV/cm) and j_{sc} = 0.09 μA/cm^2; for C, V_{oc} = 2.6 V (E_p = 0.87 kV/cm), j_{sc} = 0.11 μA/cm^2. The power conversion efficiencies under 1 sun for B and C are 1.1×10^{-4}% and 7.15×10^{-5}% respectively assuming a fill factor of 0.25 for linear *IV*. These values compare favorably to most state-of-the-art ferroelectric ceramics due to the coexistence of $P_r \geq 32$ μC/cm^2 and a direct $E_g \leq 2.5$ eV. For example, the photogenerated electric fields (E_p) for B and C are much higher than those reported for $Ba_{1-x}(Bi_{0.5}Li_{0.5})_xTiO_3$ (E_p = 0.32 kV/cm) where P_r ~10 μC/cm^2.[70] and $(K,Na)NbO_3$-$Ba(Ni_{0.5}Nb_{0.5})O_{3-\delta}$ (0.27 kV/cm) which has P_r ≈ 11 μC/cm^2.[73] Similar fields have been reported in PT-$Bi(Ni_{2/3}Nb_{1/3})O_3$ (E_p = 2 kV/cm), another MPB system with a comparable P_r; however, for that system the j_{sc} (~0.04 μA/cm^2) collected under 100 mW/cm^2 white light is more than 50% lower than those we observe for the PT-BF-BNT compositions.[16] The higher j_{sc} for PT-BF-BNT arises from the lower bandgaps and highlights the importance of combining a large P_r with a low E_g in optimizing the photovoltaic performance of ferroelectric oxide ceramics.

5.7 Conclusions

In an attempt to combine a continuous tunability of the bandgap while maximizing the ferroelectric polarization, high *c/a* perovskites along the $PbTiO_3$-$BiFeO_3$ (PT-BF) pseudo-binary were modified by substituting an MPB-forming additive, $Bi(Ni_{1/2}Ti_{1/2})O_3$ (BNT) and their photovoltaic properties were explored. Ternary compositions stabilized along the MPB have a direct E_g as low as 2.25 eV (indirect 1.75 eV) and retain a strong ferroelectric polarization (> 32 μC/cm^2) which are advantageous for photovoltaic applications. The BPVE under various wavelengths showed a switchable photoresponse with an above-bandgap V_{oc} (6V). The reduction of E_g was effective in increasing the short circuit photocurrent under 1 sun AM1.5 G conditions. It is possible additional coupling to the piezoelectric properties of these MPB compositions could also enable multisource energy harvesting applications[73]. These results may also guide future optimization of ferroelectric photovoltaics through the growth of their thin film counterparts.

Chapter 6 Photovoltaic Effects in $PbTiO_3$-$Bi(Ni_{1/2}Ti_{1/2})O_3$

6.1 Introduction and Motivation

In the previous chapters it was shown the photovoltaic response can be tuned and enhanced by engineering the bandgap and optical absorption of ferroelectric ceramics. In the $(K,Na)NbO_3$-based system, the substitution of $Ba(Ni_{0.5}Nb_{0.5})O_{3-\delta}$ greatly increases the optical absorption of the ferroelectric parent end member, which leads to a photoresponse under visible light that is orders of magnitude higher than the undoped ferroelectric oxide. However, the ferroelectric properties of $KNbO_3$-$Ba(Ni_{0.5}Nb_{0.5})O_{3-\delta}$ suffer from processing difficulties associated with the volatilization of K at high temperature and leakage currents caused by defects, especially oxygen vacancies, even though the Curie temperature of the system remains relatively high. In Chapter 4, the same strategy was applied to $BaTiO_3$ to avoid the volatilization issue during high temperature sintering. For $BaTiO_3$ the optical absorption in the visible range can be systematically controlled by changing the ratio of Ni to Nb and the accompanying $V_O^{\bullet\bullet}$. The leakage issue in $BaTiO_3$-$Ba(Ni_{0.5}Nb_{0.5})O_{3-\delta}$ was also minimized, even with substantial amounts of $V_O^{\bullet\bullet}$; however, the Curie temperature is very sensitive to foreign dopants and the $BaTiO_3$-$Ba(Ni_{0.5}Nb_{0.5})O_{3-\delta}$ solid solutions are barely ferroelectric at room temperature. To address this issue, in Chapter 5 materials that could combine a tunable narrow bandgap and a robust ferroelectric polarization with a high T_C were explored. That chapter described the properties of the $PbTiO_3$-$BiFeO_3$-$Bi(Ni_{1/2}Ti_{1/2})O_3$ system where the $PbTiO_3$-$BiFeO_3$ pseudo-binary served as the high T_C, narrow bandgap end-member and $Bi(Ni_{1/2}Ti_{1/2})O_3$ enabled further reductions in the bandgap and formation of MPB compositions with an enhanced ferroelectric response. The photovoltaic properties of the MPB compositions of the PT-BF-BNT ternary confirmed the bandgap reduction leads to increased photocurrents.

Aside from the magnitude of the bandgap, many other factors are important in optimizing the photovoltaic response of ferroelectric materials. These include, but are not limited to: the device configuration (*e.g.* electrode materials[31]/size[13,26]/contact configuration;[33] sample thickness[15]); ferroelectric polarization;[136] domain wall configuration;[9] temperature and conductivity;[12] defects and gap states;[22,137] strain gradient[138] and the concomitant flexoelectric effect.[139] Many of these factors have been extensively studied in ferroelectric thin films and single crystals.

This chapter investigates the impact of the ferroelectric polarization, electrode configuration and temperature on the photovoltaic response of the $PbTiO_3$-$Bi(Ni_{1/2}Ti_{1/2})O_3$ pseudo-binary. As discussed in Chapter 5, compositions close to the MPB in this pseudo-binary (*e.g.* 0.5PT-0.5BNT and 0.45PT-0.55BNT) show almost identical optical absorption but drastically different ferroelectric hysteresis loops. Therefore, these compositions provide an ideal opportunity to isolate the impact of the ferroelectric polarization on the PV response.

A correlation between the remanent polarization and photoresponse was established in 0.5PT-0.5BNT and confirmed by comparison of the *IV* characteristics of tetragonal 0.5PT-0.5BNT and pseudo-cubic 0.45PT-0.55BNT. The performance of 0.5PT-0.5BNT was also evaluated under different electrode configurations and over a wide range of temperature; measurements of the dielectric and mechanical properties also allowed a deeper understanding of the temperature dependence of the PV response. At low temperature the formation of a re-entrant relaxor phase produces a saturation of the photovoltage, while at high temperature the PV properties are degraded by thermal depolarization. The results also suggest that p-type behavior and thermally activated polaron hopping are the primary transport mechanisms in 0.5PT-0.5BNT, which in turn can be mediated by controlling the oxygen partial pressure.

6.2 Synthesis Details

The synthesis of the PT-BNT solid solutions followed the standard procedures described in Section 2.1. The stoichiometric raw mixtures were first calcined at 650 °C for 6 hours and multiple subsequent firings were carried out to achieve single phase purity prior to sintering. Green bodies of PT-BNT were sintered for 2 hrs at 1050 °C. Specific sample processing and testing procedures for the ferroelectric and PV measurements used in this chapter are described in the relevant sections.

6.3 PT-BNT: Polarization and PV Response

6.3.1 Polarization Switching and Photocurrent

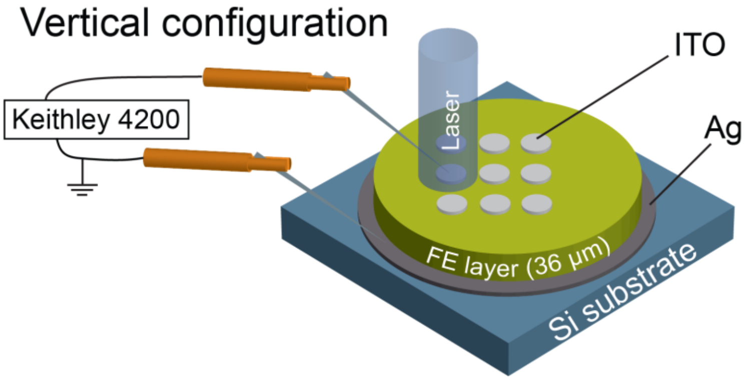

Figure 6.1 Schematic illustration of a vertical ferroelectric ceramic device for FE and PV measurement. The top surface of the sample is patterned with ITO pads (100 nm thick; 100 μm diameter) and bottom electrode is silver.

The PV and FE response of PT-BNT was initially investigated using the vertical device configuration shown in **Figure 6.1**. The sintered ceramic specimen was cut and polished down to 36 μm and ITO pads and silver were added as the top and bottom electrodes respectively. For the electrical measurements, the bottom electrode was set as the ground reference and the measuring signals applied on the top electrode. The direction of the measured current is defined as positive for flow from the top to bottom electrode through the FE layer. The device can be treated as an effective capacitor in an ITO/FE layer/silver structure.

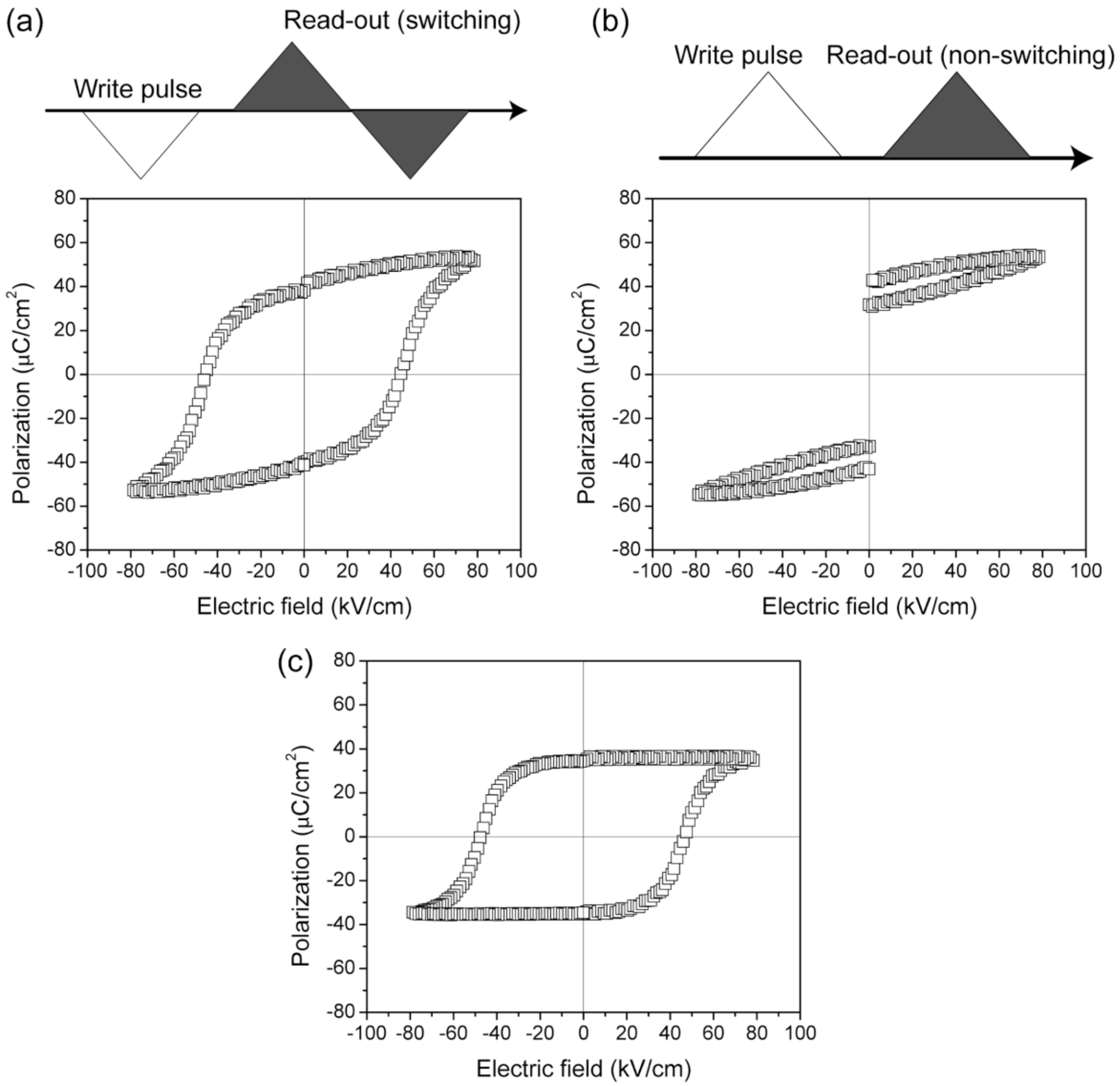

Figure 6.2 Remnant polarization hysteresis loop of 0.5PT-0.5BNT. (a) Conventional FE hysteresis loop measurement. (b) Non-switching component measurement. (c) The remnant polarization hysteresis loop: subtraction of non-switching from switching

The FE properties of 0.5PT-0.5BNT were measured to establish the remnant polarization during dynamic switching (**Figure 6.2**). In conventional FE hysteresis loop measurements (**Figure 6.2**a), the measurement signal contains a pre-pulse to first write the polarization state followed by a read-out pulse, separated by a delay time, to switch the pre-written polarization state. The read-out pulse measures the change in charge, which includes contributions from switching and non-switching behavior of the ferroelectric capacitor. The resultant hysteresis loop (**Figure 6.2**a) shows typical switching behavior; however, the remanent polarization is not the true value due to the non-switching contribution. To obtain the remnant polarization hysteresis loop, an extra measurement signal was applied without switching the polarization (**Figure 6.2**b). In this measurement, the write and read-out pulses have the same polarity to ensure the change in charge only originates from the non-switching behavior. The resultant polarization-voltage relationship (**Figure 6.2**b) clearly accounts for the small polarization induced by the non-switching behavior and after subtracting from the switching loop, the remnant polarization at each voltage level during this dynamic process was obtained (**Figure 6.2**c). This remnant polarization hysteresis loop was used to confirm the switching behavior of the PV in 0.5PT-0.5BNT.

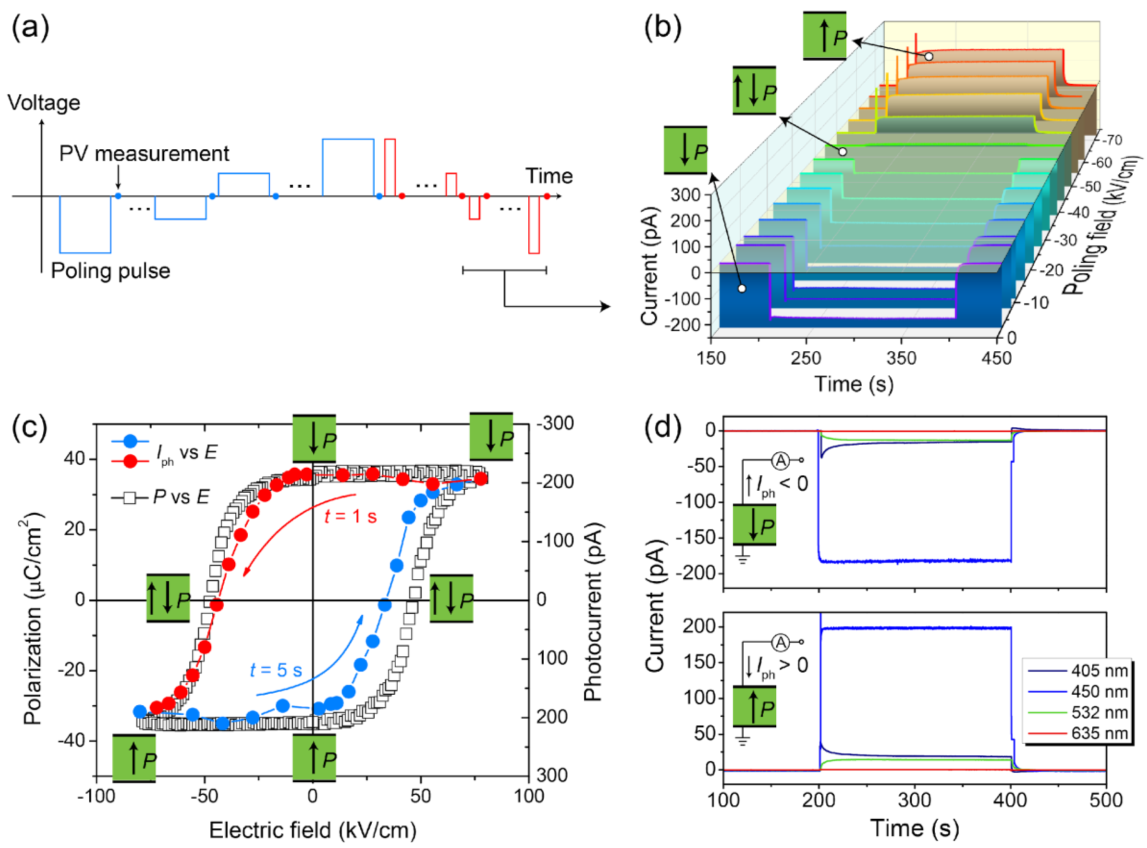

Figure 6.3 Switching behavior of PV response for 0.5PT-0.5BNT. (a) Schematic illustration of the poling and PV measurement sequence. (b) Time dependence of photocurrent under 450 nm illumination as a function of poling electric field. (c) Steady-state photocurrent under 450 nm illumination as a function of poling electric field and the remnant polarization hysteresis loop. (d) Time dependence of photocurrent under different illumination at positive and negative polarization saturation respectively.

The effect of the FE polarization on the PV response was elucidated using a procedure where the poling voltage pulse was followed by the measurement of a short-circuit photocurrent. The procedure is illustrated in **Figure 6.3**a, where the amplitude of the pulse is gradually increased from -80 kV/cm to +80 kV/cm and then ramped down to -80 kV/cm to obtain the different polarization state at the corresponding applied field. Poling pulses of 5 s and 1 s were used for the ramp up and down as shown by the blue and red step functions in **Figure 6.3**a. The short-circuit photocurrent was measured after each voltage pulse under 450 nm illumination.

Figure 6.3b shows the evolution of the short-circuit photocurrent from a negative-to-zero- to-positive net polarization for poling pulses ranging from -3 kV/cm to -80 kV/cm. After each pulse, a steady-state photocurrent was established instantaneously under illumination. The steady-state photocurrent is plotted as a function of the poling electric field in **Figure 6.3**c for comparison to the remnant polarization hysteresis loop. The striking similarity of the switching behavior of the ferroelectric polarization and the photocurrent indicates the PV response of the 0.5PT-0.5BNT ferroelectric is controlled by the remnant polarization of the system. It should be noted that the value of the coercive field for photocurrent switching is different for the 1 s and 5 s poling pulses. For the 1 s pulse the direction of the photocurrent is at 45 kV/cm, which is very close to the coercive field of remanent polarization hysteresis loop (which was measured at 0.5 Hz so the half period of the measuring signal is also 1 s). For the 5 second pulse, the coercive field of the photocurrent decreases to 35 kV/cm. It is well known that polarization switching in ferroelectrics involves domain nucleation and domain wall motion, both of which are time-dependent.[95] The time dependence observed for the switching of the photocurrent confirms the dynamics are the same as the reversal of the polarization. Three important conclusions can be drawn from these observations: first, multiple polarization states can be achieved by tuning the amplitude and width of the poling pulses; second, the retention of these states does not require additional power; third, the states can be non-destructively read out through the steady-state photocurrent. It is possible the correlation between the ferroelectric and photovoltaic switching could enable functionalities in multi-state non-volatile memory with non-destructive optical readout.

The switchable behavior of the photocurrent is maintained over a broad range of wavelengths (**Figure 6.3**c), and under 405 nm, 450 nm, 532 nm and 635 nm illumination the short-circuit photocurrents show a symmetric reversal from a positive to negative saturation polarization state. Similar to the compositions in the ternary PT-BF-BNT system, the photocurrent of 0.5PT-0.5BNT shows a wavelength dependence that is related to the bandgap of the sample (direct E_g 2.85 eV and indirect E_g 2.22 eV). Of these four wavelengths, the 450 nm illumination (which is closest to the direct bandgap of the sample) promotes the largest photocurrent (185 pA) and is 12× higher than that for 405 nm and 532 nm (~15 pA). Under 635 nm illumination, which is below the direct and indirect bandgap values, only a very small steady-state photocurrent (0.5 pA) was observed, which could be associated with occupied states in the forbidden band. The enhancement of the photocurrent when the energy of the illumination is close to bandgap is presumably due to the coincidence of the absorption depth and sample thickness, as this leads to strong absorption throughout the sample and an instant photoresponse without any transients from the build-up of a space charge region. The 450 nm laser was used for additional characterizations of the PV response.

6.3.2 Polarization Retention and Its Impact on the PV Response

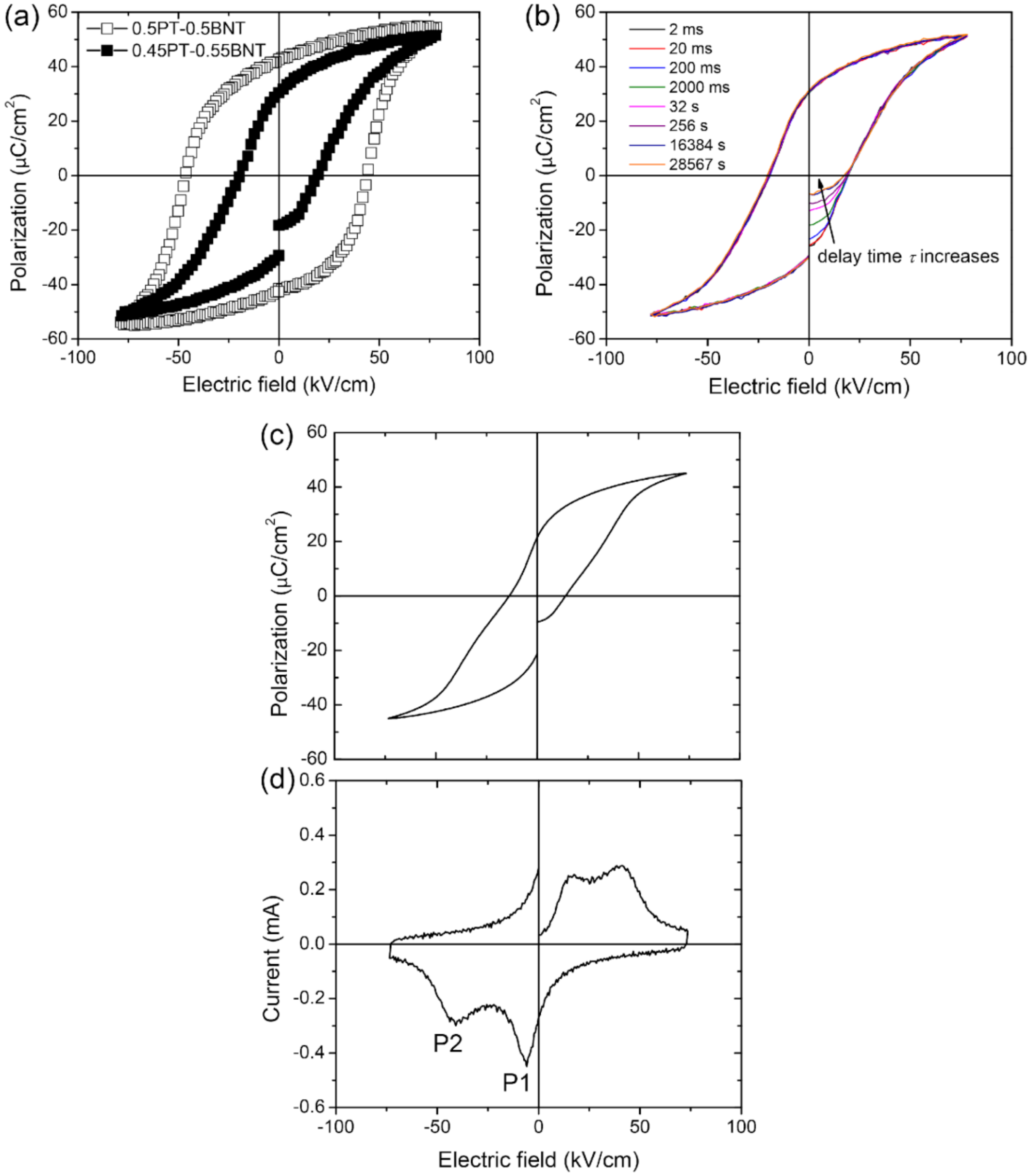

Figure 6.4 Comparison of ferroelectric properties of 0.5PT-0.5BNT and 0.45PT-0.55BNT. (a). Ferroelectric hysteresis loops of both compositions in ITO/FE layer (~ 30 μm)/Ag. (b) Response of ferroelectric hysteresis loops for 0.45PT-0.55BNT on delay time between preset pulse and measuring pulses. (c) Ferroelectric hysteresis loop of 0.45PT-0.55BNT measured from pellet sample Ag/FE pellet (0.5 mm)/Ag. (d) Corresponding current as a function of applied field.

In addition to mediating the switching behavior, the polarization retention plays an important role in controlling the PV response of the ferroelectric samples. In this section the PV properties of tetragonal 0.5PT-0.5BNT and pseudocubic 0.45PT-0.55BNT, which have different polarization retention behavior, are compared. In Chapter 5 0.5PT-0.5BNT and 0.45PT-0.55BNT were shown to have identical bandgaps, which eliminates the possibility of the influence of the optical absorption on their PV response. The FE hysteresis loops of these compositions were measured using the vertical ITO/FE layer/Ag configuration (see **Figure 6.1**). Tetragonal 0.5PT-0.5BNT has a closed loop with E_c = 46 kV/cm, a spontaneous polarization P_s = 54 μC/cm^2, and P_r = 42 μC/cm^2. The true P_r = 35 μC/cm^2 is smaller, as discussed earlier. The hysteresis loop for pseudocubic 0.45PT-0.55BNT is narrower with E_c = 20 μC/cm^2, P_s = 52 μC/cm^2 and P_r = 30 μC/cm^2, consistent with the location of the composition at the MPB in the PT-BNT pseudobinary. 0.45PT-0.55BNT also shows a gap between the start and end of the loop. The gap arises from the 1 second delay, τ, between the preset and measurement pulses when a loss of polarization can occur. This is evidenced by the increase in the magnitude of the gap with increasing τ (**Figure 6.4**b).

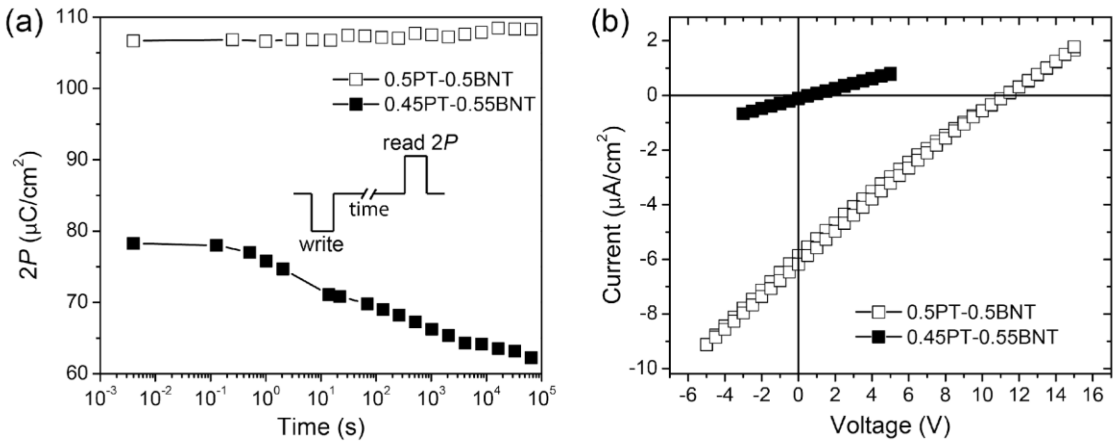

Figure 6.5 Polarization retention and its impact on PV response of 0.5PT-0.5BNT and 0.45PT-0.55BNT. (a) Retention polarization as a function of time. (b) *IV* characteristics of pre-poled samples under 450 nm illumination.

The polarization retention of 0.5PT-0.5BNT and 0.45PT-0.55BNT were evaluated further by measuring the time-dependence of the decay using electric write and read pulses separated by a given decay time (**Figure 6.5**a). Tetragonal 0.5PT-0.5BNT shows no loss of polarization over a long period of time (10^5 second); however, for pseudocubic 0.45PT-0.55BNT the polarization gradually decays after 0.1 second with a linear-log time dependence. The depolarization can be explained by the response of the structure of the MPB composition to the electric field. As shown in Chapter 5, the XRD pattern of 0.45PT-0.55BNT only exhibits pseudocubic perovskite peaks without any apparent broadening from a rhombohedral or monoclinic distortion; this is different to the tetragonal/rhombohedral coexistence observed at the MPB in PZT and PT-BiScO$_3$.[140] Structural analyses of PT-BNT and a chemical similar system, PT-Bi(Ni$_{1/2}$Zr$_{1/2}$)O$_3$, suggest the Bi-rich side of MPB retain an average $Pm\bar{3}m$ symmetry,[141,142] which has been shown to be a manifestation of a locally distorted tetragonal structure where the distorted regions only have a very short coherence length.[142,143] The application of an electric field on such a pseudocubic system induces a transition to a ferroelectric phase with a correlated, long-range tetragonal distortion and reorients the non-180° domains. Previous studies of PT-BNT and La-doped PT-BF[143–145] showed both effects can be reversed when the electric field is removed (or alternated) and induce the retention loss we observe in 0.45PT-0.55BNT. The existence of a reversible field-induced phase transition and domain switching is also supported by the pinched ferroelectric hysteresis loop in measurements of a bulk pellet sample using silver electrodes (see **Figure 6.4**c and d), where the two peaks in the current (P1 and P2, **Figure 6.4**d) potentially correspond to the domain switching and pseudocubic to tetragonal phase transition, respectively.

The *IV* characteristics of 0.5PT-0.5BNT and 0.45PT-0.55BNT were measured under 450 nm illumination after poling the samples under a +80 kV/cm field for 1 min. In **Figure 6.5**b, both samples show a PV response with a positive open-circuit voltage induced by the preferred reorientation of the ferroelectric domains. The *IV* response of tetragonal 0.5PT-0.5BNT, where V_{oc} = 11.5 V (3.2 kV/cm) and j_{sc} = −6.2 µA/cm^2, is the largest combination of both values reported for any ferroelectric ceramic. Due to the retention loss, the values are significantly reduced in pseudocubic 0.45PT-0.55BNT, where V_{oc} = 0.5 V and j_{sc} = 0.1 µA/cm^2. These results are similar to those reported in a recent study of La-doped $BiFeO_3$ thin films, where compositions near a boundary between the polar and non-polar phases showed PV enhancements from the polar instability.[64]

6.3.3 Electrode Configuration

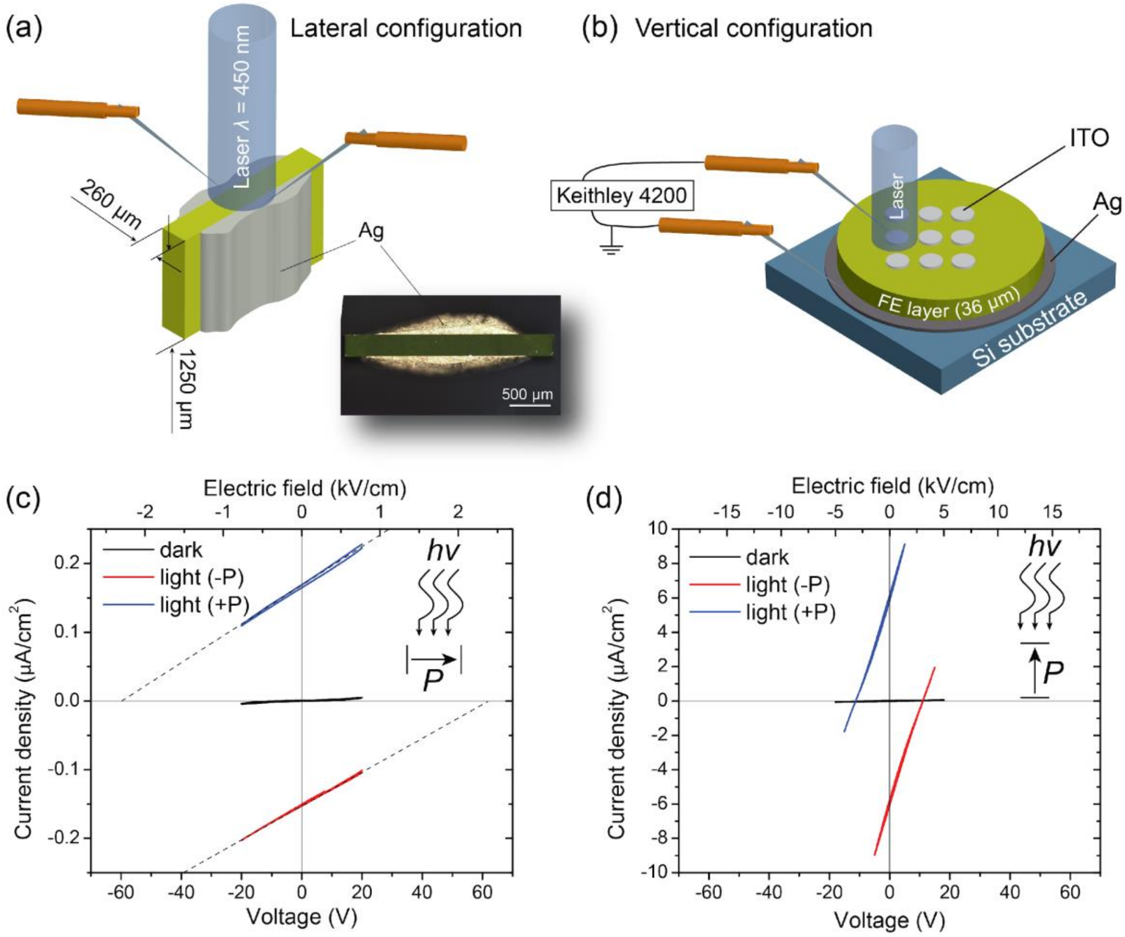

Figure 6.6 (a) Lateral configuration Ag/FE layer (260 µm)/Ag. (b) Vertical configuration ITO/FE layer (36 µm)/Ag. (c) *IV* characteristics of lateral device. (d) *IV* characteristics of vertical device.

To clarify the effect of the electrode configuration on the PV response, the performance of devices with electrodes on the two lateral sides of the sample (**Figure 6.6**a) were compared to their vertical electrode counterparts (**Figure 6.6**b). The 260 µm thick 0.5PT-0.5BNT ferroelectric layer was poled by applying ±80 kV/cm field between the two side electrodes to introduce a “−P” (pointing to the left) and “+P” (pointing to the right) polarization state. The top surface of the lateral device was illuminated by the laser such that the direction of the incident light was perpendicular to the ferroelectric polarization. The lateral device shows a linear *IV* response which is switched when the polarization is reversed (see **Figure 6.6**c); the V_{oc} is extremely high and beyond the voltage limit of the source measure unit. By extrapolating the measured *IV* curves, values of V_{oc} = 62 V (E_{ph} = 2.4 kV/cm) and j_{sc} = 0.16 µA/cm^2 were obtained for the −P and +P state respectively.

The 36 µm thick vertical device (see **Figure 6.6**b) was poled by applying ±80 kV/cm field between the top and bottom electrodes with the resultant polarization either parallel (−P) or anti-parallel (+P) to the direction of laser. The *IV* curves show the same polarity and linear response as the lateral device, however the values of V_{oc} = 11 V (E_{ph} = 3 kV/cm) and j_{sc} = 6.0 µA/cm^2 are different. These differences are associated with the interelectrode spacings of the two devices and the absorption depth of the 450 nm light. The linear relationship between j and V for both devices implies the photocurrent is not affected by the applied voltage. The total current can be written as a linear addition of the short-circuit photocurrent and the electric-field driven drift current as follows:

$$j = j_{\mathrm{sc}} - \frac{V}{L}\left(\sigma_{\mathrm{d}} + \sigma_{\mathrm{ph}}\right)$$

where L is the interelectrode spacing, σ_{d} and σ_{ph} are the dark and photo-conductivities respectively.[24] Under open-circuit conditions, the photocurrent is canceled the drift current, resulting in zero total current. Therefore, the open-circuit voltage is expressed as:

$$V_{\mathrm{oc}} = \frac{j_{\mathrm{sc}}L}{\sigma_{\mathrm{d}} + \sigma_{\mathrm{ph}}}$$

It is clear the V_{oc} in the ferroelectric scales with the distance between the two electrodes and is not limited by the bandgap of the sample. This is consistent with the observation that the V_{oc} of the lateral device (62 V) far exceeds that of the vertical device (11 V), due to the much larger interelectrode spacing, $L = 260\ \mu\mathrm{m}$. In addition, the V_{oc} of both devices are multiple times higher than the bandgap of 0.5PT-0.5BNT (direct $E_{\mathrm{g}} = 2.85$ eV). For high intensity illumination, $\sigma_{\mathrm{ph}} \gg \sigma_{\mathrm{d}}$, the V_{oc} is then approximated as:

$$V_{\mathrm{oc}} \cong \frac{j_{\mathrm{sc}}L}{\sigma_{\mathrm{ph}}}$$

As the light intensity increases, j_{sc} and σ_{ph} increase at the same rate, leading to a saturation of V_{oc}.[8] This suggests in the limit of high intensity illumination, the photo-induced electric field E_{ph} is constant regardless of the light intensity. The smaller $E_{\mathrm{ph}} = 2.4$ kV/cm observed in the lateral device is attributed to the large volume of the sample that is not illuminated, leading to a breakdown of the $\sigma_{\mathrm{ph}} \gg \sigma_{\mathrm{d}}$ condition and, in turn, a lower E_{ph} compared to the saturation value. For the lateral device, the height of the sample (1250 µm) is much larger than the absorption depth of the 450 nm laser in 0.5PT-0.5BNT (the absorption coefficients of transition metal oxides at wavelengths close to the bandgap are typically on the order of 10^2 to 10^4 cm^{-2}, which yields an absorption depth of 1 to 100 µm), therefore strong absorption is limited to the surface of the sample. Normalizing the total current (generated in the small illuminated region) by the large lateral electrode size (0.017 cm^2) also leads to the smaller $j_{\mathrm{sc}} = 0.16\ \mu\mathrm{A/cm}^2$ for the lateral device. The larger $E_{\mathrm{ph}} = 3$ kV/cm and 40 times higher $j_{\mathrm{sc}} = 6.0\ \mu\mathrm{A/cm}^2$ for the vertical device are due to the higher effective absorption of the light per unit volume. The 3 kV/cm photoinduced electric field in these systems is higher than the other materials that exhibit above-bandgap photovoltages (thin film $BiFeO_3$ 0.8 kV/cm;[9] $BiFeO_3$ 2.6 kV/cm;[13] ceramic La-doped PZT 2 kV/cm;[15] $MAPbI_3$ 2 kV/cm;[101] ceramic $BiVO_4$ 0.07 kV/cm[37]).

6.4 0.5PT-0.5BNT: Temperature Dependence of the PV Response

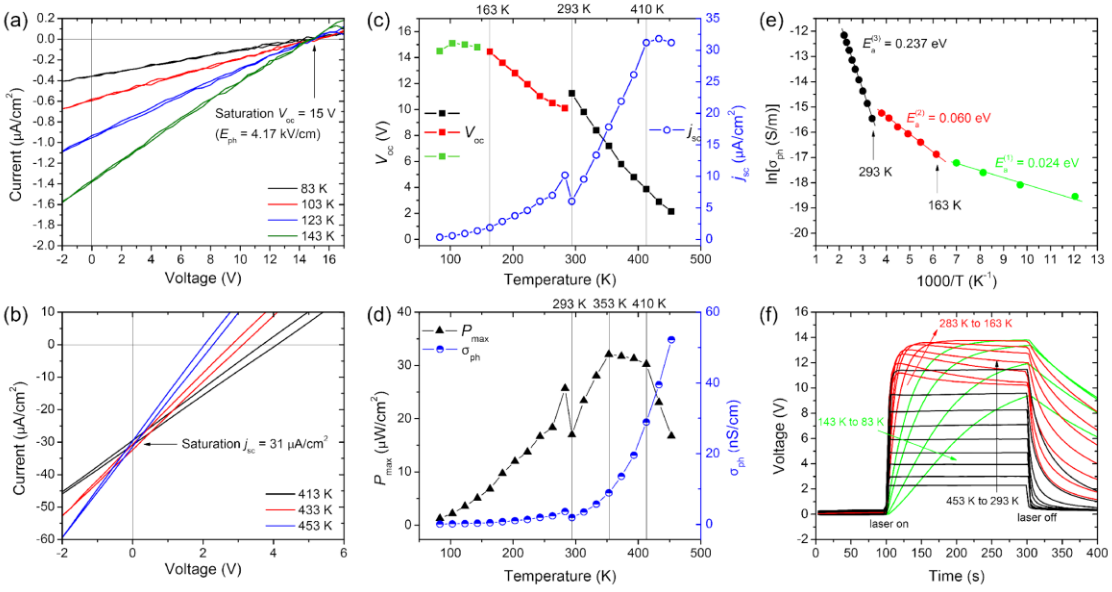

Figure 6.7 Temperature-dependent PV response of 0.5PT-0.5BNT vertical device under 450 nm illumination. (a) *IV* characteristics at low temperatures (from 83 K to 143 K); (b) *IV* characteristics at high temperatures (from 413 K to 453 K); (c) Temperature dependence of open-circuit-voltage V_{oc} and short-circuit-current j_{sc}; (d) Temperature dependence of maximum power density P_{max} and photoconductivity σ_{ph}; (e) Arrhenius plot of the photoconductivity σ_{ph}; (f) Time dependence of open-circuit-voltage V_{oc} at different temperatures.

The temperature dependence of the PV response of the 0.5PT-0.5BNT vertical device was investigated from 83 K to 453 K using a 450 nm laser. After poling at 300 K through the application of a +80 kV/cm field on one ITO electrode, the device was cooled to 83 K in the probe station. *IV* sweeps and measurements of the time-dependence of the open-circuit-voltage were made by heating and thermally equilibrating the samples in 20° increments. At all temperatures, the vertical device showed a linear *IV* response with an above-bandgap V_{oc} (**Figure 6.7**a and b); V_{oc} and j_{sc} are plotted as a function of temperature in **Figure 6.7**c. The temperature dependence of V_{oc} shows three distinct slopes as represented by the different colors in **Figure 6.7**c: between 83-143K V_{oc} saturates at a maximum of ~15 V (green points), while j_{sc} gradually increases with temperature; from 163K-283 K, V_{oc} decreases to 10 V (red points in **Figure 6.7**c); at 293 K, V_{oc} abruptly increases to 11.3 V followed by an essentially linear decrease to 2.3V at 453K (black points). The j_{sc} generally increases continuously with temperature (blue curve, **Figure 6.7**c) reaching a maximum value of 31 μA/cm^2 at 453K; however, an anomaly is again observed at 293K, where the rate of increase with *T* increases, and between 413 K - 453 K the current appears to saturate.

The *IV* data can be used to calculate the temperature dependence of the maximum power density, $P_{\mathrm{max}} = 0.25 j_{\mathrm{sc}} V_{\mathrm{oc}}$ (where the linear *IV* response implies a maximum fill factor of 0.25) and photoconductivity, $\sigma_{\mathrm{ph}} = \frac{j_{\mathrm{sc}} L}{V_{\mathrm{oc}}}$ (**Figure 6.7**d). P_{max} increases from 83K to 293 K where a sudden decrease is observed; at higher *T* P_{max} reaches a maximum at 353 K and then decreases and saturates at 410K. σ_{ph} shows an exponential-type increase with respect to *T*, with an anomaly at 293 K. The temperature dependence of the photoconductivity can be quantified using a thermally activated Arrhenius relationship:

$$\sigma_{\mathrm{ph}} = \sigma_0 \exp(-\frac{E_{\mathrm{a}}^{(\mathrm{i})}}{kT})$$

where σ_0 is the pre-exponential factor and $E_\mathrm{a}^{(\mathrm{i})}$ is activation energy for the conductivity in a specific range of temperature range (denoted by the letter i). In the Arrhenius plot (**Figure 6.7**e) the fits to the data reveal three linear regions with the transition temperatures corresponding to those observed in the V_oc-T curves. The first linear region (83 K - 163 K) has $E_\mathrm{a}^{(1)}$ of 0.024 ± 0.002 eV; for the second (163 K - 283 K) $E_\mathrm{a}^{(2)} = 0.060 \pm 0.002$ eV and for the third region (293 K - 453 K) $E_\mathrm{a}^{(3)} = 0.237 \pm 0.002$ eV. The results clearly suggest the PV response is governed by different photoconduction mechanisms in the three ranges of temperature. The different mechanisms also affect the time dependent variation of V_oc when the light is turned on and off (see **Figure 6.7**f). Between 83 K and 143 K, the light induced V_oc requires a long time (> 200s) to increase (or decay) to a steady state value; from 163 K to 283 K, V_oc rapidly increases to a maximum upon illumination and then slowly decays toward a lower steady state value; from 293 K to 453 K the steady state V_oc is reached instantaneously.

The results from the *IV* data show clear evidence for transitions in the temperature dependence of V_oc, j_sc, P_max, and σ_ph at ~160 K, 300 K, 350 K and 410 K. We first consider the transition at 350 K where P_max reaches its maximum value of 32 μW/cm^2, which corresponds to a power conversion efficiency of 1.6×10^{-3}% under 450 nm illumination by a laser with 200 mW/cm^2 peak intensity. For traditional PN junction based solar cells, an increase in temperature usually degrades of P_max due to the large reduction in V_oc with only a small concomitant increase in j_sc.[146] In the 0.5PT-0.5BNT ferroelectric, V_oc and j_sc are both strongly temperature dependent and correlate with each other through σ_ph. A balance between V_{oc} and j_{sc} is required to increase the maximum power; this can be potentially controlled through tuning the σ_{ph} by annealing and doping.

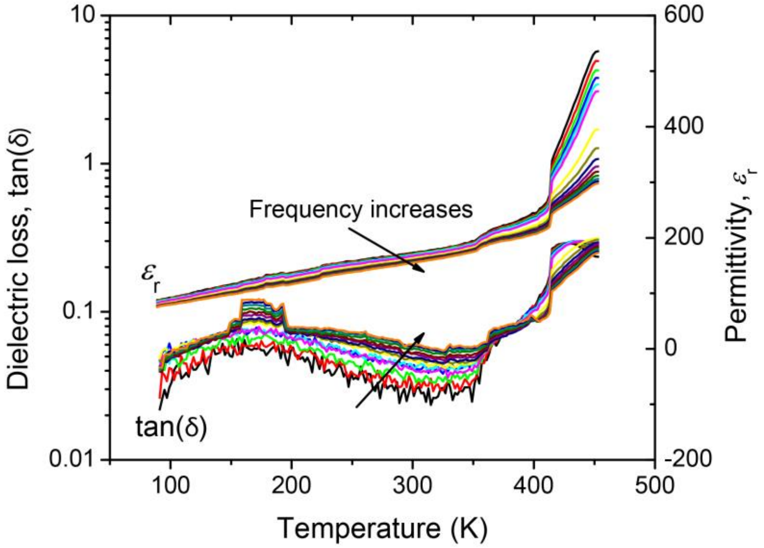

Figure 6.8 Dielectric measurement of the poled 0.5PT-0.5BNT vertical device; The data were taken every 2 K on poled region of ITO/FE layer (36 μm)/Ag configuration ramping from 90 K to 450 K in probe station.

At 410 K j_{sc} no longer increases with T, coupled with the decreasing V_{oc}, this leads to a rapid decrease in P_{max}. To understand if this change was associated with the thermal depolarization of 0.5PT-0.5BNT, dielectric measurements were conducted on the vertical device. The temperature dependence of the dielectric response of the poled region under the ITO top electrode is shown in **Figure 6.8**. At 410K a sharp increase in the permittivity and dielectric loss was observed for all frequencies (50 kHz to 1 MHz), consistent with partial depolarization of the sample. The onset of depolarization occurs well below the Curie temperature of 0.5PT-0.5BNT (T_C ~670 K). Because the poled regions are embedded in a large unpoled “matrix” (**Figure 6.6**b), the onset of depolarization below T_C is likely facilitated by the interfacial energy and discontinuity of the polarization between the two regions. Above 410 K the samples clearly retain a significant fraction of the polarization as V_{oc} is still > 2V at 453 K and recovers to 10 V (slightly smaller than the original V_{oc} = 11 V after poling at 293 K) when the temperature is cooled back to room temperature.

In addition to the anomaly associated with partial thermal depolarization, a broad frequency dependent relaxation peak is clearly present in the dielectric spectra between 150 K to 200 K (**Figure 6.8**). This relaxation is related to the formation of nanopolar domains and is discussed in the following section.

6.5 160 K Re-entrant Relaxor Transition

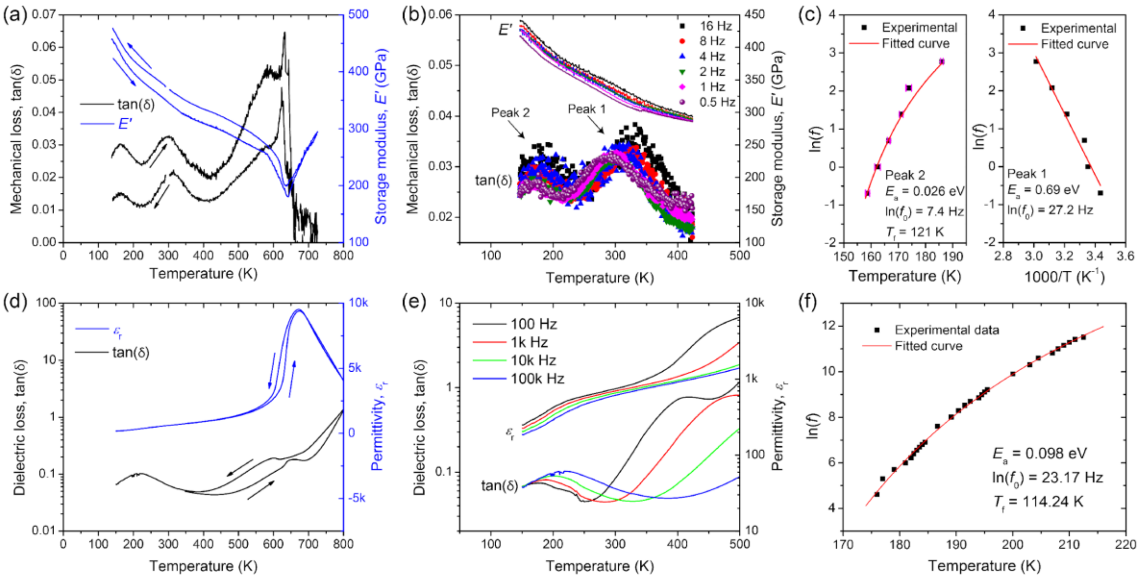

Figure 6.9 Temperature dependent mechanical and dielectric responses of 0.5PT-0.5BNT. (a) Dynamic mechanical analysis (DMA) of 0.5PT-0.5BNT: temperature dependency of storage modulus and mechanical loss under 1 Hz dynamic force; (b) frequency dependent DMA from 150 K to 420 K where two anelastic relaxations (Peak 1 and Peak 2) are present; (c) right: Vogel-Fulcher fitting of relaxation Peak 1; left: Arrhenius fitting of relaxation Peak 2; (d) dielectric measurement of 0.5PT-0.5BNT: temperature dependency of permittivity and dielectric loss under 100 kHz ac field; (e) frequency dependent of dielectric response from 150 K to 500 K; (f) Vogel-Fulcher fitting of the dielectric relaxation around 200 K.

To understand the temperature dependence of the PV response, the dielectric and dynamic mechanical responses of tetragonal 0.5PT-0.5BNT were investigated. Dynamic mechanical analysis (DMA) is the mechanical analog of dielectric spectroscopy and allows the storage modulus and mechanical loss to be measured; this is a useful method for characterizing phase transitions and the relaxation behavior of ferroelectrics especially when the dielectric measurement is complicated by electrical conduction. The DMA measurements were made at 1 Hz on ceramic bars of 0.5PT-0.5BNT under 3-point bending geometry upon heating and cooling. The storage modulus (see **Figure 6.9**a) shows a sharp minimum at 640 K, corresponding to the Curie temperature where the paraelectric to ferroelectric phase transition occurs. The mechanical loss tangent has two additional maxima at 300 K and 165 K (peaks 1 and 2, **Figure 6.9**b). The loss peaks are reversible with little to no thermal hysteresis and coincide with the temperatures where the changes in the activation energy of the photoconductivity was observed (**Figure 6.7**e). The loss maxima are not accompanied by an anomaly in the storage modulus, suggesting they are related to anelastic relaxations rather than a phase transition.

To elucidate the relaxation response frequency-dependent DMA measurements were made between 150 K to 423 K (**Figure 6.9**b). The temperatures of the loss maxima were quantified using Gaussian functions (see **Figure 6.10**); both peaks are displaced to higher temperature as the frequency increases, confirming they originate from an anelastic relaxation. It is possible the frequency dispersion could be induced by a transition into a relaxor state or through a diffusional defect-related relaxation.[147] The dynamics of relaxor transitions are typically described by the Vogel-Fulcher relationship, $f = f_0 \exp[\frac{E_\mathrm{a}}{k(T_\mathrm{M} - T_0)}]$, where f is the measurement frequency, f_0 is the pre-exponential factor, E_a is the activation energy, T_M is the loss peak temperature and T_0 is the freezing temperature. Defect-related relaxations follow an Arrhenius-type behavior where $f = f_0 \exp(\frac{E_\mathrm{a}}{kT_\mathrm{M}})$ describes the dynamics of independent dipoles. Due to the limited range of frequency accessible in DMA, the fitting of the observed data by the two models does not show a significant statistical difference. However, their origin can be elucidated by comparison with the dielectric response.

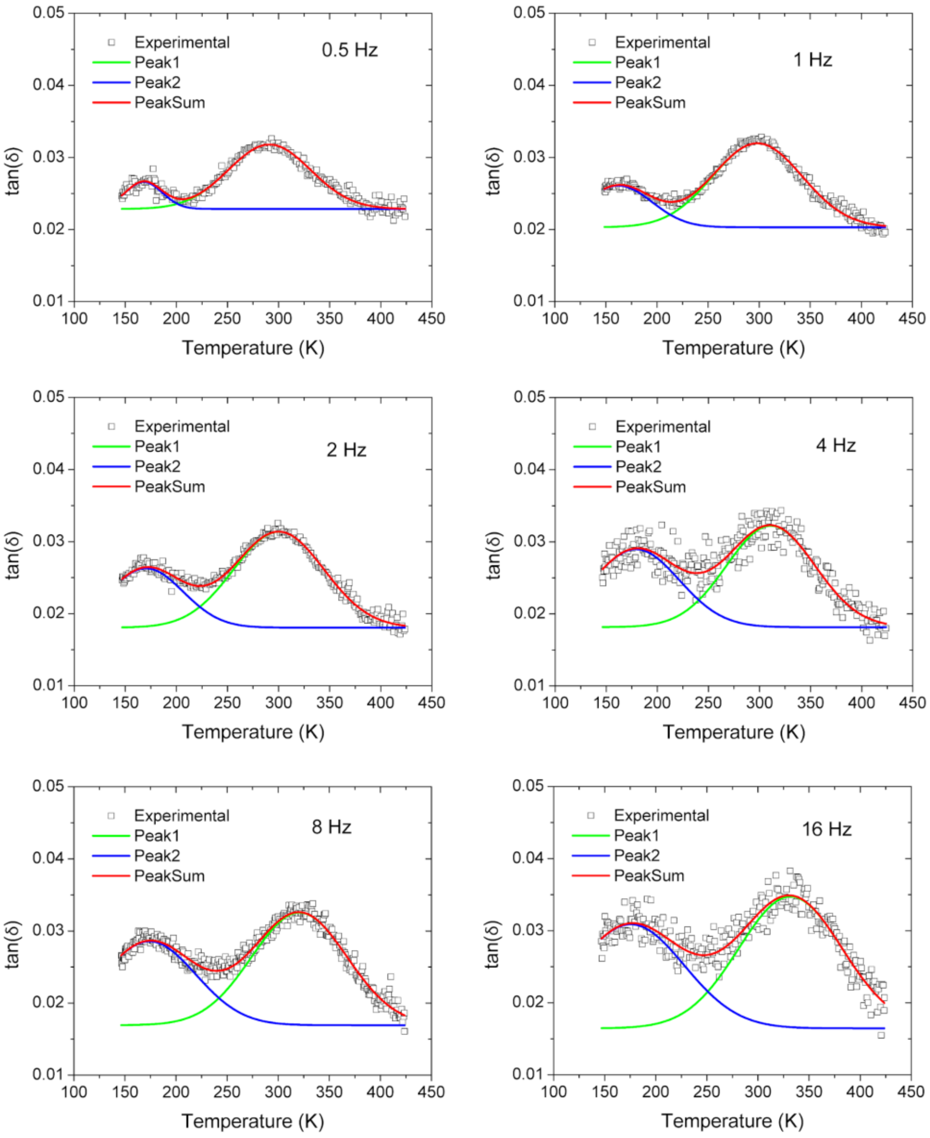

Figure 6.10 Fitting of mechanical loss tan(δ) of different frequencies.

The temperature dependence of the permittivity and dielectric loss at 100 kHz (**Figure 6.9**d) shows a clear peak at ~650 K corresponding to T_C; however, the dielectric loss data at 100 kHz show a second diffuse maximum at ~220 K. Additional measurements show this maximum is frequency dependent with the loss peak being displaced to lower temperature at lower frequency (**Figure 6.9**e). The temperature and frequency dependence of this dielectric relaxation is essentially identical to peak 2 in the DMA data. The broader range of measurement frequencies accessible for the dielectric measurements allow detailed modeling and the Vogel-Fulcher law clearly provide a better statistical fit (**Figure 6.9**f), confirming the loss maxima are associated with a transition to a relaxor ferroelectric state. The resultant activation energy, $E_a = 0.098 \pm 0.003$ eV, agrees well with the values reported for other relaxors such as $Pb(Mg_{1/3}Nb_{2/3})O_3$ (PMN) or the low temperature relaxation of MPB composition in PT-$BiScO_3$, and is associated with the switching energy barrier for the polar nanoregions (PNRs).[148,149]

At room temperature the average symmetry of 0.5PT-0.5BNT is tetragonal and this ferroelectric phase persists to low temperature without showing any long-range phase transition. The observed relaxation is therefore attributed to the so-called re-entrant relaxor behavior where the PNRs exist a ferroelectric matrix. Similar low temperature relaxations are observed in the well-known MPB compositions of PT-relaxor systems [*e.g.* PT-PMN, PT-$Pb(Zn_{1/3}Nb_{2/3})O_3$] and are important for their exceptional piezoelectric performance.[150] The PNRs have different local symmetry to the ferroelectric matrix and the thermodynamics is governed by the free energy of the entire system, which consists of the Landau energy and interfacial energies (electrostatic, gradient and elastic) associated with the discontinuity of the polarization and strain at the nanoscale interface. According to phase field simulations of PT-PMN,[150] the local PNRs transform to tetragonal symmetry and have dipoles collinear with the ferroelectric matrix at high temperature to minimize the contribution from the interfacial energies. However, at low temperature the Landau term dominates the free energy and the direction of the PNRs are no longer constrained to the polar direction of the ferroelectric matrix.[151] This model can be used to explain the saturation of V_{oc} in 0.5PT-0.5BNT for $T < 160$ K as the local inhomogeneity caused by PNRs that are non-collinear with the ferroelectric matrix will decrease the net polarization along the polar direction of the macroscopic tetragonal domains. The reduction of the net polarization will in turn prevent any further increase in $V_{\mathrm{oc}} = \frac{j_{\mathrm{sc}}L}{\sigma_{\mathrm{ph}}}$ by lowering σ_{ph} as temperature decreases. The additional interfaces between the PNRs and the ferroelectric matrix may also mediate the photoconductivity of the system, leading to the change in activation energy of σ_{ph} at 160 K.

Returning to the mechanical relaxation peaks, peak 2 of the loss can now be assigned to the transition into a re-entrant relaxor state and the frequency dependence can be assumed to follow a Vogel-Fulcher relationship (**Figure 6.9**c, left). The resultant activation energy, $E_a = 0.026$ eV, is presumably associated with the energy barrier for domain wall motion of the PNRs under dynamic stress. This activation energy is lower than the barrier for the polarization switching of PNRs in the ac electric field (0.098 eV). The freezing temperature T_f for the dielectric (114K) and mechanical (121K) relaxations are essentially identical confirming the PNRs are responsible for both.

6.6 300 K transition

The second maximum in the mechanical loss at ~ 300 K (“peak 1” in **Figure 6.9**b), has no counterpart in the dielectric response, but coincides with one of the changes in the activation energy for photoconduction. However, at the lowest frequencies (100 Hz and 1k Hz) the dielectric loss does begin to increase above this temperature culminating in a very broad, frequency dependent, maximum above 400 K (**Figure 6.9**e). The absence of any increase in the permittivity or of any peaks in the loss at higher frequency (100k Hz) suggests that space charge/diffusional carriers, which only respond to low-frequency fields, are the source of this relaxation.[147] The types and concentrations of charge carriers are correlated to the defect chemistry of the system and will be affected by temperature and by the oxygen partial pressure (pO_2) during annealing.

Additional indications of the importance of the defect chemistry was discovered in the initial mechanical measurements of 0.5PT-0.5BNT in the DMA system. The first measurements were made on “as-prepared” specimens that had not been subjected to any type of controlled pO_2 annealing after sintering. For the DMA analysis the sample was first cooled to low temperature (~150 K) using nitrogen gas that flowed into the measurement system from a liquid source. For the first data set, collected upon heating (under nitrogen) to a temperature (725 K) above the Curie point, the 300 K maximum in the loss was clearly observed; however, this peak was absent on cooling if the sample was maintained in the nitrogen atmosphere. It became apparent the irreversibility of the transition resulted from the loss of oxygen and partial reduction of the sample in the N_2 atmosphere at the higher temperature. If the sample reduction was avoided, for example by heating to a temperature that was too low (*e.g.* 425 K) to allow any type of reduction in a short time, the transition was fully reversible.

In “stoichiometric” 0.5PT-0.5BNT, which has the chemical formula $(Pb^{2+}_{0.5}Bi^{3+}_{0.5})(Ti^{4+}_{0.75}Ni^{2+}_{0.25})O_3$, none of the components are present in an oxidation state that would be expected to be reduced by nitrogen gas at such a low temperature (725 K). Furthermore, in the absence of any additional non-stoichiometry, it is not possible for the

Ni^{2+} cation (which is the only species that could reasonably be expected to change oxidation state under these conditions) to oxidize when the oxygen sub-lattice is fully occupied. However, it is well known that in these Pb/Bi based perovskites small degrees of volatilization of the A-site cations can occur during sintering (with Pb typically being the most volatile) leading to the formation extrinsic oxygen vacancy defects through the following reaction:

$$\mathrm{Pb_{Pb}} + \mathrm{O_O} \rightleftharpoons \mathrm{PbO} + \mathrm{V_{Pb}''} + \mathrm{V_O^{\bullet\bullet}}$$

where Kröger-Vink notation of the point defects are adopted.

Given that the volatilization takes place during sintering, it would be possible to oxidize the ceramics through lower temperature annealing or slow cooling with the filling of the oxygen vacancies being charge compensated by the partial oxidation of Ni from 2+ to 3+:

$$2\mathrm{Ni_{Ni}} + \mathrm{V_O^{\bullet\bullet}} + \frac{1}{2}\mathrm{O_2} \rightleftharpoons 2\mathrm{Ni_{Ni}^{\bullet}} + \mathrm{O_O}$$

In the following section we provide direct evidence for the redox activity of 0.5PT-0.5BNT and its effect on the mechanical relaxation phenomena.

6.7 Effect of pO_2 Annealing Studies

6.7.1 Dielectric and Mechanical Responses

As discussed in the previous section, the room temperature transition in the mechanical loss of 0.5PT-0.5BNT was affected by the annealing atmosphere suggesting that $\mathrm{V_{Pb}''}$, $\mathrm{V_O^{\bullet\bullet}}$, and $\mathrm{Ni_{Ni}^{\bullet}}$ defects play an important role in dictating the physical properties of the system. According to the defect chemistry model, the concentration of Pb vacancies $[V_{Pb}'']$ will be established during high temperature sintering (> 1000 °C), while $[V_O^{\bullet\bullet}]$ and $[Ni_{Ni}^{\bullet}]$ are determined by the pO_2 (and T) during cooling or lower temperature annealing. The charge neutrality equilibrium can be expressed as

$$2[V_{Pb}''] = 2[V_O^{\bullet\bullet}] + [Ni_{Ni}^{\bullet}]$$

assuming the absence of free electrons in the system. By changing the pO_2, and hence $[V_O^{\bullet\bullet}]$ and $[Ni_{Ni}^{\bullet}]$, the role of the different defects on the properties of 0.5PT-0.5BNT can be elucidated.

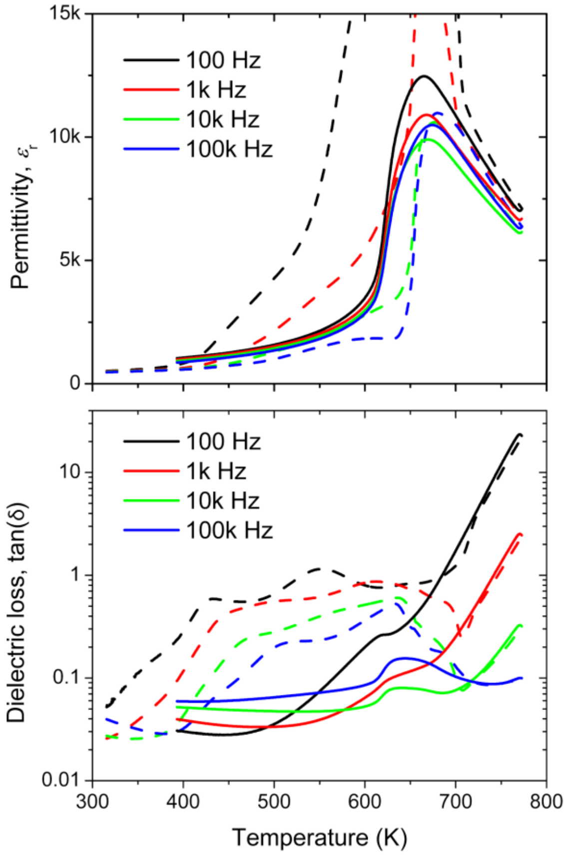

Figure 6.11 Dielectric response of as-prepared 0.5PT-0.5BNT measured in N_2 purge. Dashed and solid lines represent ramp-up and cool-down respectively.

As noted above, the potential role of the pO_2 was observed during measurements of the mechanical response of as-prepared 0.5PT-0.5BNT under a N_2 purge gas. For an "as-prepared" sample, the V_{Pb}'' could be partially compensated by $Ni_{Ni}^{\bullet}$ through the filling of the oxygen vacancies during the post-sintering cooling. The presence of $Ni_{Ni}^{\bullet}$ could in turn induce conductivity and dielectric relaxation at elevated temperature. **Figure 6.11** shows the dielectric response when the as-prepared sample was heated from room temperature ("ramp-up", dashed lines) under a nitrogen purge gas. On heating the data show considerable frequency dispersion and a rapid increase of the permittivity below T_C that is likely associated with the contribution from the $Ni_{Ni}^{\bullet}$-induced conductivity. However, when temperature reaches ~700 K, the low frequency permittivity drops precipitously, with an associated abrupt change in the dielectric loss, due to the onset of a redox reaction that reduces the Ni^{3+} to Ni^{2+}, decreases $[Ni_{Ni}^{\bullet}]$, and increases $[V_O^{\bullet\bullet}]$. When the sample is cooled, still under nitrogen ("cool-down" cycle), there is no replenishment of oxygen and the sample cannot re-oxidize to recover the conductivity of the as-prepared state. The permittivity during the cool-down cycle shows almost no frequency dependence, no enhanced contributions from $Ni_{Ni}^{\bullet}$-induced conductivity, and the dielectric loss is reduced significantly compared to the ramp-up cycle.

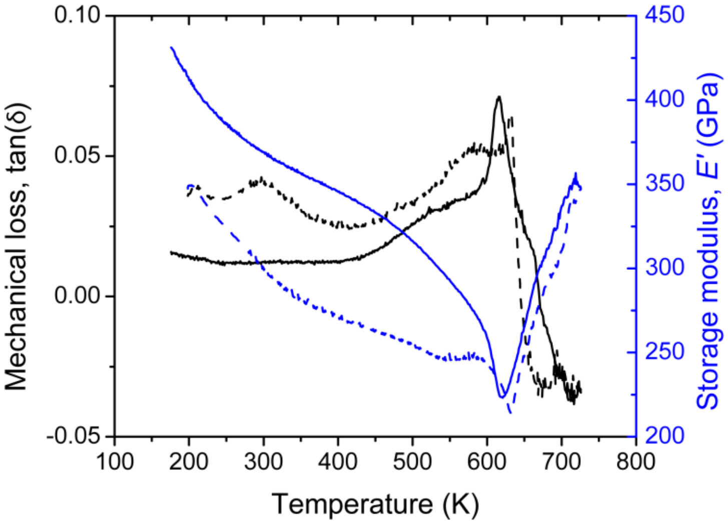

Figure 6.12 Dynamic mechanical analysis of as-prepare 0.5PT-0.5BNT measured in N_2 purge. Dashed and solid lines represent ramp-up and cool-down respectively.

A series of controlled experiments were also made to quantify the irreversible changes in the mechanical response for as-prepared 0.5PT-0.5BNT during the DMA measurements under a N_2 purge (see **Figure 6.12**). The mechanical loss maximum centered at ~300 K, which is related to a $V_{Pb}''-Ni_{Ni}^{\bullet}$ induced anelastic relaxation, is only present during the ramp-up (dashed line). For the cool-down cycle (solid line), the loss peak is not recovered due to the redox reaction at ~ 700 K which reduces Ni^{3+} and increases $V_{O}^{\bullet\bullet}$. These two experiments clearly show the formation of $Ni_{Ni}^{\bullet}$ induces the dielectric and anelastic relaxations observed above 400 K and at ~300 K respectively.

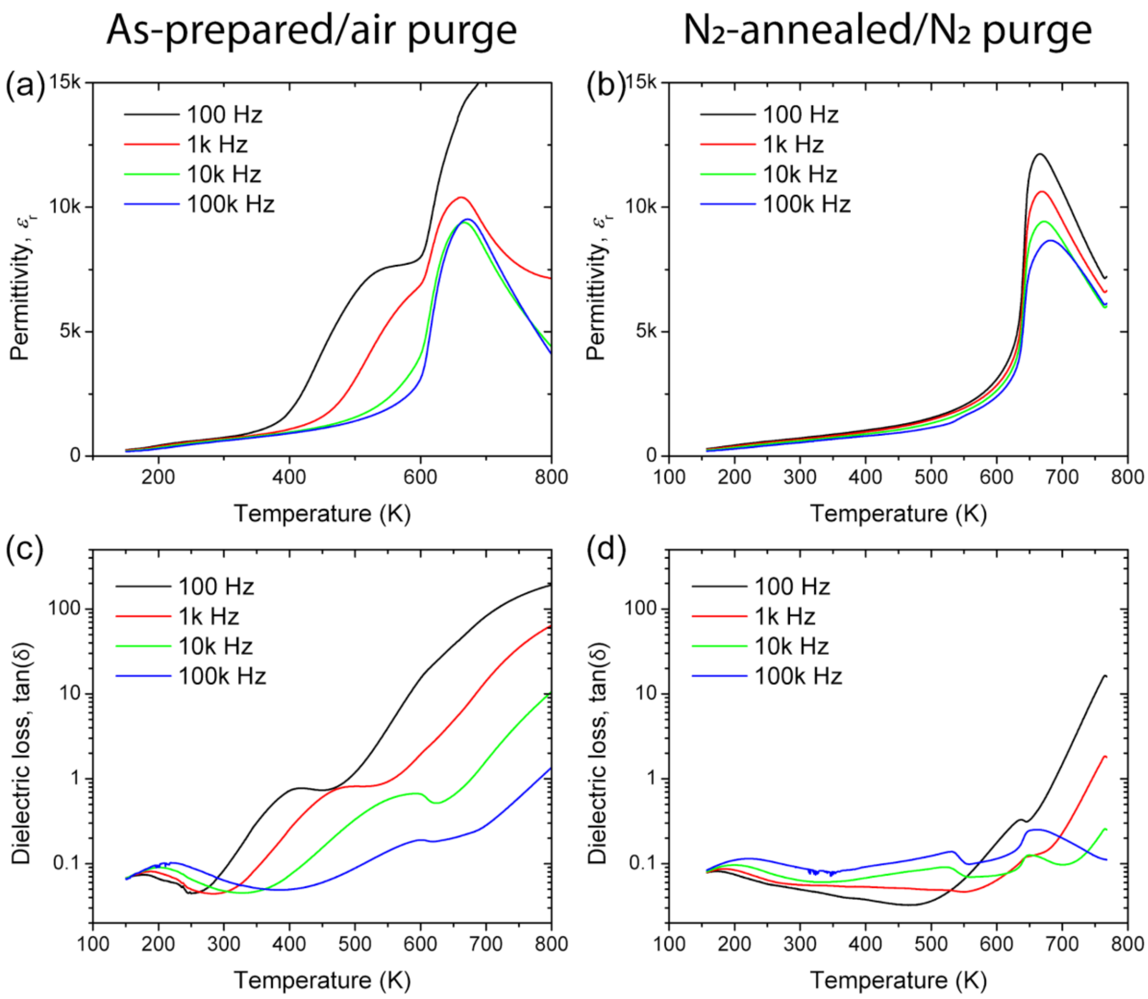

Figure 6.13 Temperature dependence of dielectric response for as-prepared 0.5PT-0.5BNT sample in air purge: (a) permittivity and (c) dielectric loss; Temperature dependence of dielectric response for N_2 annealed 0.5PT-0.5BNT sample in N_2 purge: (b) permittivity and (d) dielectric loss.

The dielectric response of the as-prepared sample was also measured in an air purge gas to inhibit the redox reaction; the temperature dependence of the permittivity and dielectric loss are shown in **Figure 6.13**a and c. The increase in the low frequency permittivity at ~400 K and the loss relaxation above 300 K were caused by the $\mathrm{Ni}_{\mathrm{Ni}}^{\bullet}$ present in the as-prepared sample as discussed previously. However, in contrast to the N_2 purge, there is no sudden change in the dielectric properties at elevated temperature from a redox reaction. The as-prepared sample was then annealed in N_2 at 500 °C for 12 hours, conditions expected to reduce all of the nickel to the +2 state and maximize the oxygen vacancy content, and the dielectric response was measured under N_2 gas to preserve the fully reduced state. Consistent with this expectation, the permittivity showed minimal frequency dependence (**Figure 6.13**b) and a significantly smaller loss (**Figure 6.13**d) compared to its “as-prepared” counterpart. It is important to note the different annealing treatments have no effect on the low temperature dielectric relaxation at 200 K indicating the re-entrant relaxor transition is independent of the concentration of $\mathrm{Ni}_{\mathrm{Ni}}^{\bullet}$ and $\mathrm{V}_{\mathrm{O}}^{\bullet\bullet}$ defects.

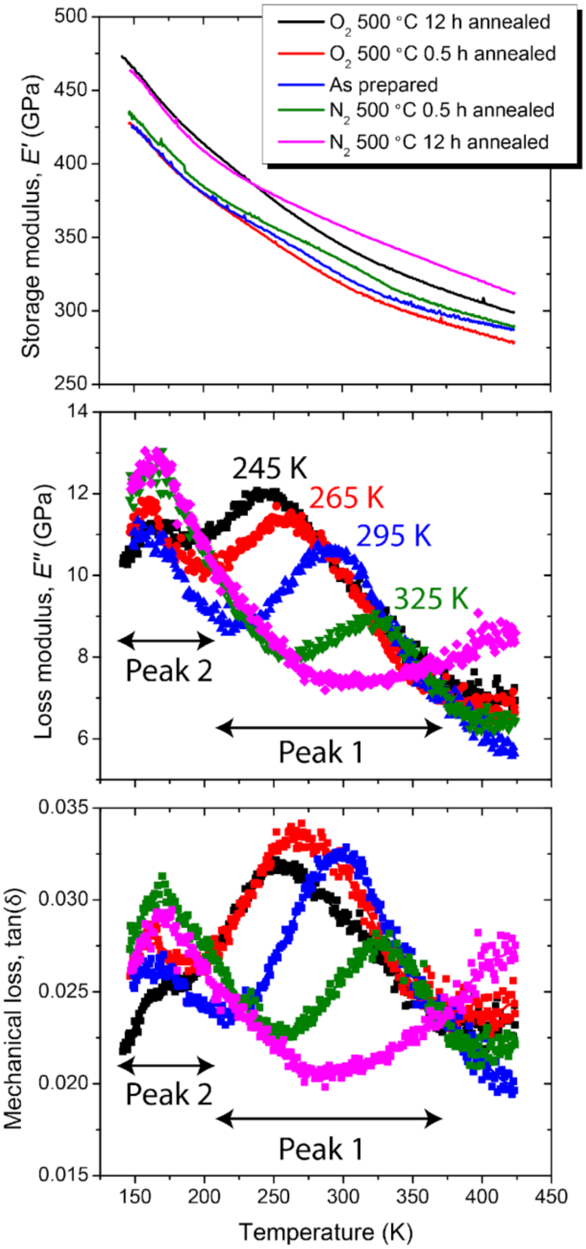

Figure 6.14 Temperature dependence of mechanical response under 1 Hz dynamic force for 0.5PT-0.5BNT samples annealed in different conditions.

The impact of the defects on the anelastic relaxation was also investigated by DMA by annealing the as-prepared samples under different conditions to control the $[\mathrm{Ni}_{\mathrm{Ni}}^{\bullet}]$ and

$[V_O^{\bullet\bullet}]$. The degree of oxidation was maximized through a 12 hour anneal in pure O_2 at 500°C and minimized by a nitrogen gas anneal for the same time and temperature. Shorter anneal times (*e.g.* 0.5 h) were also used to estimate the kinetics of the redox reaction at this temperature. The samples tested are listed in order of the expected $[Ni_{Ni}^{\bullet}]$ in **Figure 6.14**. The storage modulus of each sample shows a stiffening behavior as the temperature decreases without any discernible peaks associated with a phase transition. In contrast, the loss modulus and loss tangent (which reflect the energy dissipation) show two well defined maxima (labelled peak 1 and 2 in **Figure 6.14**). The lowest temperature maximum at ~160K (peak #2) does not show any dependence on the annealing treatment; this peak originates from the previously described relaxor behavior of the PNRs in the long-range ferroelectric matrix, which causes both dielectric and anelastic relaxations. However, the position and intensity of the higher temperature peak (#1) are strongly correlated to the annealing conditions. The peak is completely absent in the least oxidized sample (12 hr N_2 anneal) and systematically increases in intensity and displaces to lower temperature as the degree of oxidation (higher $[Ni_{Ni}^{\bullet}]$, lower $[V_O^{\bullet\bullet}]$) increases: *i.e.* $T_{max}(12hr\ O_2) < T_{max}(0.5hr\ O_2) < T_{max}(as\text{-}prepared) < T_{max}(0.5hr\ N_2)$. These results clearly confirm this relaxation is directly related to the concentration of $Ni_{Ni}^{\bullet}$ (Ni^{3+}) and its absence in the N_2 12 hr sample demonstrates the presence of oxygen vacancies does not play a role in this anelastic transition.

As the temperature approaches T_C, all samples show a gradual increase in the loss beginning at ~350 K. This feature is essentially independent of the annealing condition.

6.7.2 Optical Properties

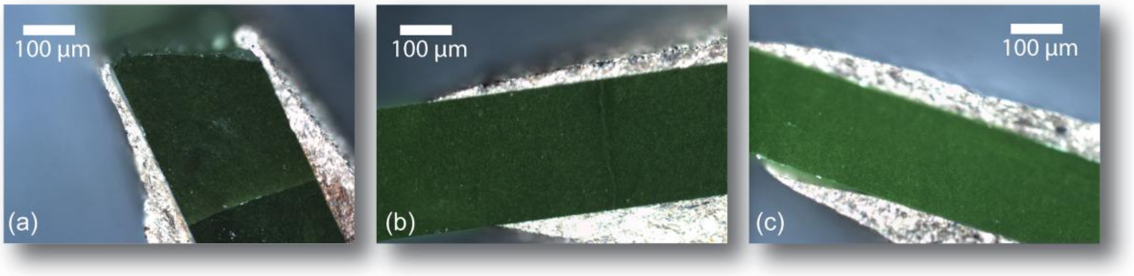

Figure 6.15 Pictures of (a) O_2 500 °C 12 hour annealed, (b) as-prepared, and (c) N_2 500 °C 12 hour annealed 0.5PT-0.5BNT samples.

The different annealing conditions also induce visible changes in the color of the samples; these are evident in **Figure 6.15** which shows optical images of as-prepared, and O_2-, N_2-annealed (500 °C, 12 hr) 0.5PT-0.5BNT. The samples darken as the pO_2 and $[Ni_{Ni}^{\bullet}]$ increase. While the darkening of titanate based ceramics is well known, for pure titanates such as $BaTiO_3$ and $SrTiO_3$ the darkening is induced through reduction (of Ti) rather than oxidation, with the oxygen vacancies and trapped electrons forming color centers that produce broad absorption peak below 2 eV.[82,152] The observation of the opposite effect in 0.5PT-0.5BNT compared to the n-type $BaTiO_3$ and $SrTiO_3$ systems, indicates p-type $Ni_{Ni}^{\bullet}$ color centers are responsible for the darkening of the oxidized samples. Future UV-vis spectroscopy measurements on the annealed samples would be helpful in quantifying the changes in optical absorption.

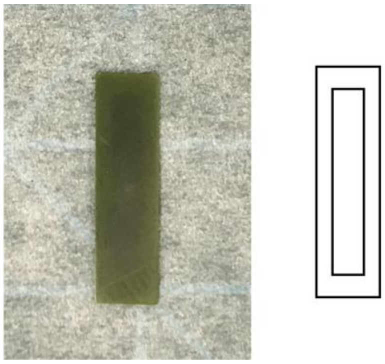

Figure 6.16 Frame effect of N_2 500 °C 0.5 hour annealed 0.5PT-0.5BNT samples.

For the shorter anneals (0.5 hr) at 500 °C the redox reaction is limited by kinetics and the ceramics show the well-known "picture-frame" effect, **Figure 6.16**. This as-prepared sample had been annealed in nitrogen for 30 minutes and the picture shows the darker more oxidized interior is surrounded by the brighter reduced edges. As the reduction front diffuses into the sample the width of the frame increases, and with time (5 hrs are sufficient) the core and edges have a uniform concentration of oxygen vacancies and Ni^{2+} and a homogenous bright green color.

6.7.3 Electrical Properties

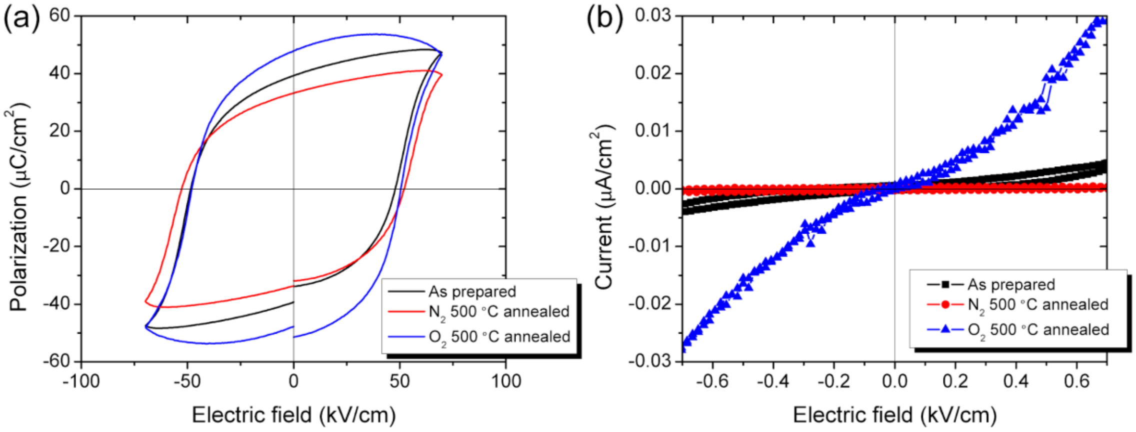

Figure 6.17 (a) Ferroelectric hysteresis loops of 0.5PT-0.5BNT annealed under different conditions; (b) dark *IV* characteristics of 0.5PT-0.5BNT annealed under different conditions.

To quantify the effect of the redox reaction on the ferroelectric response of 0.5PT-0.5BNT, *P-E* hysteresis loops of samples annealed under the different conditions were measured at 1 Hz. The *P-E* loops were strongly dependent on the annealing history and resultant defects, see **Figure 6.17**a. The loop for the O_2 500 °C annealed sample has a rounded shape which is characteristic of a significant contribution from the leakage associated with the $\mathrm{Ni}_{\mathrm{Ni}}^{\bullet}$ defects in the oxidized sample. The leakage component is reduced by the 500 °C N_2 annealing and produces a more square-like loop characteristic of an ideal ferroelectric capacitor. Although $\mathrm{Ni}_{\mathrm{Ni}}^{\bullet}$ induces leakage during ferroelectric switching, all samples have the same coercive field (~50 kV/cm).

The leakage is also apparent in the dark *IV* characteristics of 0.5PT-0.5BNT, **Figure 6.17**b. The O_2 500 °C annealed sample has a significantly enhanced dark conductivity manifested by the large slope of the *IV* curve; the increase arises from the higher concentration of $\mathrm{Ni}_{\mathrm{Ni}}^{\bullet}$ carriers. This *IV* also shows a small degree of nonlinearity which is not present in the as-prepared or N_2 annealed samples. The nonlinearity is characteristic of a diode-type response possibly associated with Schottky barriers at the electrode interfaces formed when the Fermi level is changed by the higher concentration of $\mathrm{Ni}_{\mathrm{Ni}}^{\bullet}$.

6.7.4 Electronic Transport Mechanisms: Polaron Hopping

The defect mechanisms in 0.5PT-0.5BNT, involving extrinsic oxygen vacancies and oxidizable Ni cations, are now considered in more detail to understand the changes in the activation energies for photoconduction.[153] In the low pO_2 regime, ionic compensation with $[\mathrm{V}_{\mathrm{Pb}}'']$ = $[\mathrm{V}_{\mathrm{O}}^{\bullet\bullet}]$ is dominant, all of the Ni remains in a divalent state and the conductivity is minimized. At high pO_2, oxidation occurs by the filling of the extrinsic $V_O^{\bullet\bullet}$ and formation of $Ni_{Ni}^{\bullet}$ (Ni^{3+}):

$$2Ni_{Ni} + V_O^{\bullet\bullet} + \frac{1}{2}O_2 \rightleftharpoons 2Ni_{Ni}^{\bullet} + O_O$$

The conductivity reaches a maximum when $2[V_{Pb}''] = [Ni_{Ni}^{\bullet}]$ leading to a change from ionic to electronic compensation.

This defect model implies these systems have p-type conductivity realized by hopping of localized holes through the lattice. The increase in permittivity and the low frequency dispersion observed in dielectric measurements above 400 K are induced by carrier hopping; this polaron behavior has been observed in a similar temperature range in other closely related systems.[152,154,155] Subsequent annealing in oxidizing atmospheres, which is supposed to reduce the difference between the partially reduced grains and oxidized barrier layers formed during sintering and cooling respectively, actually further increases the loss and conductivity, suggesting an interfacial effect such as Maxwell-Wagner polarization is not the main factor in the observed dielectric relaxation. More importantly, it is consistent with the proposed defect model that the trapped hole concentration $[Ni_{Ni}^{\bullet}]$ is governed by pO_2 and its hopping contributes to the dielectric relaxation and the conduction (detailed discussion in next section).

The anelastic relaxation of peak 1 in the mechanical loss (**Figure 6.9**b) could be attributed to the dipolar behavior of a defect associate $V_{Pb}''-Ni_{Ni}^{\bullet}$ which can interact with the motion of the ferroelectric/ferroelastic domain walls under stress. The reorientation of the $V_{Pb}''-Ni_{Ni}^{\bullet}$ associate under dynamic stress is thermally activated and the loss peak shows Arrhenius-type behavior (**Figure 6.9**c) with an activation energy (0.69 ± 0.05eV) related to the motion of polarons.[155,156] The magnitude of the activation energy is also significantly smaller than the values for $V_O^{\bullet\bullet}$ diffusion (≥ 0.9 eV) obtained from DMA[157] and dielectric[152]/conduction[97] measurements on similar oxides, ruling out the effect of $V_O^{\bullet\bullet}$ motion on the anelastic relaxation. This conclusion is further supported by the studies of the effect of the concentration of $[Ni_{Ni}^{\bullet}]$ on the anelastic relaxation discussed in section 6.7.1. When $[Ni_{Ni}^{\bullet}]$ is varied through the annealing under different pO_2's, the position of peak 1 systematically changes, shifting to lower for a higher concentration and higher temperature for lower and ultimately disappearing when the anelastic relaxation is eliminated when $[Ni_{Ni}^{\bullet}] = 0$.

6.7.5 Electronic Transport Mechanisms: Photoconductivity (σ_{ph}) and Dark Conductivity (σ_d)

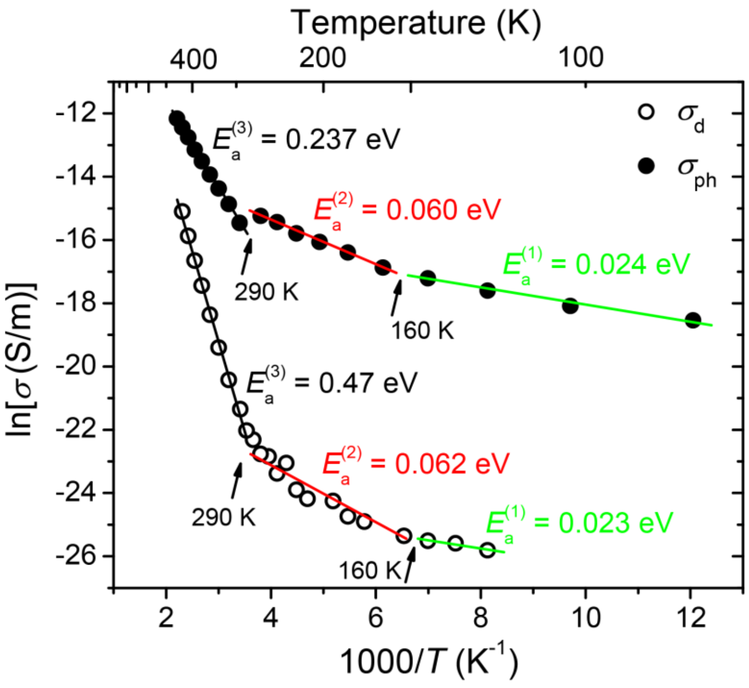

Figure 6.18 Temperature dependence of photoconductivity (σ_{ph}) and dark conductivity (σ_d).

A comparison of the temperature dependence of the photo- (σ_{ph}) and dark-conductivity (σ_{d}) was made to further elucidate the conduction mechanism. σ_{ph} and σ_{d} are plotted as a function of $1/T$ in **Figure 6.18**; the temperature dependence can be divided into three regions with different activation energies.

Above 290 K, the activation energy of σ_{d} (0.47 eV) is greater than σ_{ph} (0.24 eV) and σ_{d} approaches σ_{ph} as temperature increases. In this regime, the dark conductivity σ_{d} depends on a number of factors:

$$\sigma_{\mathrm{d}} = e(n\mu_{\mathrm{n}} + p\mu_{\mathrm{p}})$$

where n and p are electron and hole carrier concentrations respectively, μ_{n} and μ_{p} are their mobilities.

In 0.5PT-0.5BNT, the majority carriers are holes which show polaronic transport; the hole concentration and mobility are thermally activated and the total activation energy is the sum of the polaron binding (W_{p}) and hopping (W_{h}) energy.[158,159] The difference in energy of a bound (where $\mathrm{Ni}_{\mathrm{Ni}}^{\bullet}$ is close to $\mathrm{V}_{\mathrm{Pb}}^{\prime\prime}$) and free ("normal" $\mathrm{Ni}_{\mathrm{Ni}}^{\bullet}$ not associated with $\mathrm{V}_{\mathrm{Pb}}^{\prime\prime}$) polaron is defined as W_{p}; under thermal equilibrium the hole polaron concentration can be expressed as

$$p = p_0 \exp(\frac{W_{\mathrm{p}}}{kT})$$

where $p_0 = [\mathrm{Ni}_{\mathrm{Ni}}^{\bullet}] = 2[\mathrm{V}_{\mathrm{Pb}}^{\prime\prime}] - 2[\mathrm{V}_{\mathrm{O}}^{\bullet\bullet}]$. Above 290 K the results in **Figure 6.18** yield a total activation energy for the dark conductivity, $E_{\mathrm{a}}^{(3)} = W_{\mathrm{p}} + W_{\mathrm{h}} = 0.47 \pm 0.01$ eV.

Under illumination the photogenerated excess carriers dominate the conduction and the photoconductivity can be expressed by:

$$\sigma_{\mathrm{ph}} = eG(\tau_{\mathrm{n}}\mu_{\mathrm{n}} + \tau_{\mathrm{p}}\mu_{\mathrm{p}})$$

where G is the rate of photoexcitation and $\tau_{n,p}$ is the lifetime of the corresponding carriers. In the photoconduction process, only the carrier mobility is thermally activated and the activation energy for σ_{ph} is primarily associated with W_{h}. Therefore, at $T > 290$ K, $E_{\mathrm{a}}^{(3)} = W_{\mathrm{h}} = 0.237 \pm 0.002$eV is smaller than the activation energy for dark conduction. The polaron binding energy W_{p} can then be calculated: where $W_{\mathrm{p}} = 0.47 – 0.24 = 0.23 \pm 0.01$ eV.

Below 290 K σ_{ph} ~10^3 - 10^4 is higher than σ_{d}, however the ln(σ) versus T^{-1} curves for dark and photoconduction are essentially parallel with similar activation energies. In the lower T regime the transport mechanism can change to phonon-assisted hopping ("variable range" hopping[41]) between localized states, with a reduction of the activation energy and a conductivity that follows a ln(σ)~$T^{-1/4}$ relation.[42] The identical activation energies at low temperature suggest the photo and dark conduction share the same transport mechanism with the PV effect being independent of the details of the hopping mechanism.

6.7.6 Summary

In summary, the dielectric and anelastic relaxation measurements of 0.5PT-0.5BNT do not show evidence for any long-range phase transitions below T_{C}. However, a transition into a re-entrant relaxor state below ~200K, is accompanied by dielectric and anelastic relaxations. Local inhomogeneities induced by the formation of the relaxor phase in the ferroelectric matrix also cause a saturation of the open-circuit voltage around 160 K. A second anelastic relaxation at ~300 K is induced by the presence of the defect associate $V_{Pb}''-Ni_{Ni}^{\bullet}$ that results in a low frequency dielectric relaxation through polaron conduction. The temperature dependence of the dark and photoconductivity can be explained by polaron transport which changes from a trap-controlled mechanism at high temperature to variable range hopping at low temperature.

6.8 PV Properties of Annealed 0.5PT-0.5BNT

6.8.1 Effect of pO$_2$

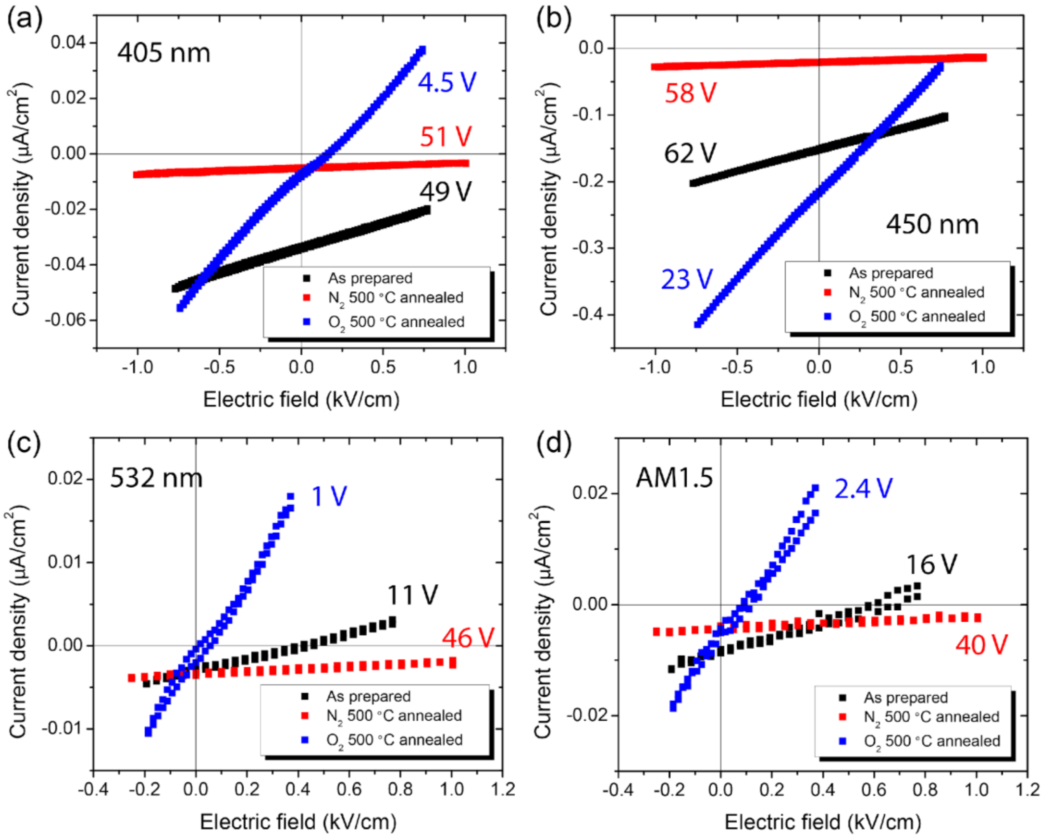

Figure 6.19 Room temperature photovoltaic *IV* characteristics of lateral 0.5PT-0.5BNT samples annealed under different conditions. (a) 405 nm; (b) 450 nm; (c) 532 nm; and (d) AM1.5 illumination.

Because the formation of oxidized $\mathrm{Ni}_{\mathrm{Ni}}^{\bullet}$ defects clearly play an important role in mediating the electrical, mechanical, and optical absorption properties of 0.5PT-0.5BNT, the PV properties were re-characterized using samples that had been subjected to controlled annealing treatments. As-prepared and 500 °C annealed O_2 and N_2 ceramics were polished and coated with silver electrodes using the lateral configuration. The photovoltaic *IV* responses of poled (80 kV/cm field, 60 seconds) samples were investigated using 405 nm, 450 nm, 532 nm and AM1.5 illuminations.

All samples show a linear photovoltaic response with the same polarity (see **Figure 6.19**), consistent with a bulk photovoltaic effect. Because the thickness and electrode area of each sample was slightly different, the *IV* curves are plotted with respect to the normalized current density and electric field. The V_{oc} of each *IV* curve is also labeled to emphasize the "anomalous" above-bandgap voltages. The short-circuit current density j_{sc}, photovoltaic electric field E_{ph}, photoconductivity σ_{ph}, and maximum power per unit thickness P_{max} for the three samples are summarized in **Table 6-1**.

Table 6-1 Summary of room temperature photovoltaic parameters of 0.5PT-0.5BNT samples

Light source	Sample	j_{sc} (μA/cm^2)	E_{ph} (kV/cm)	σ_{ph} × 10^{-9} (S/m)	P_{max} (μW/cm^2) for 1 cm thick sample
405 nm	N_2 annealed	0.0052	**2.57**	0.2	3.34
	As-prepared	**0.0340**	1.89	1.8	**16.05**
	O_2 annealed	0.0075	0.17	4.5	0.31
450 nm	N_2 annealed	0.0207	**2.92**	0.7	15.07
	As-prepared	0.1522	2.38	6.4	**90.48**
	O_2 annealed	**0.2199**	0.85	25.6	46.40
532 nm	N_2 annealed	**0.0034**	**2.31**	0.1	**1.98**
	As-prepared	0.0031	0.41	0.7	0.31
	O_2 annealed	0.0013	0.04	3.6	0.01
AM1.5	N_2 annealed	0.0043	**1.99**	0.2	**2.13**
	As-prepared	**0.0086**	0.62	1.3	1.33
	O_2 annealed	0.0057	0.09	6.3	0.13

The *IV* curves of the three samples have distinct slopes which implies different σ_{ph}. The O_2 500 °C sample, with the highest $[\mathrm{Ni}_{\mathrm{Ni}}^{\bullet}]$, has the largest σ_{ph} under all illuminations; the smallest σ_{ph} is observed in the N_2 500 °C sample with the lowest $[\mathrm{Ni}_{\mathrm{Ni}}^{\bullet}]$. The dependence of σ_{ph} on $[\mathrm{Ni}_{\mathrm{Ni}}^{\bullet}]$ is the same as that observed for the dark conductivity (**Figure 6.17**b).

E_{ph} and j_{sc} are related to σ_{ph} through the following equation

$$E_{ph} = \frac{V_{oc}}{L} = \frac{j_{sc}}{\sigma_d + \sigma_{ph}} \approx \frac{j_{sc}}{\sigma_{ph}}$$

where the approximation only holds when $\sigma_d \ll \sigma_{ph}$. By reducing the $[\mathrm{Ni}_{\mathrm{Ni}}^{\bullet}]$ charge carriers, which decrease σ_d and σ_ph, E_ph of the N_2 annealed sample is enhanced under all illuminations compared to its as-prepared and oxidized counterparts. However, j_sc is strongly dependent on wavelength and does not directly scale with σ_ph; for example, under 532 nm illumination, the oxidized sample (0.0013 μA/cm^2) has a smaller j_sc than the N_2 sample (0.0034 μA/cm^2), while for 405 nm j_sc of the N_2 sample (0.0054 μA/cm^2) is smaller (j_sc of oxidized = 0.0075 μA/cm^2). For photovoltaic applications, ideally high power conversion efficiency is achieved through a combination of large E_ph and large j_sc with a fill factor close to 1. At 405 nm and 450 nm none of the samples combine the largest E_ph and j_sc; the highest P_max is observed in the as-prepared sample where a tradeoff between E_ph and j_sc is achieved. At 532 nm all samples have a small j_sc due to the limited absorption of the below-bandgap illumination and the N_2 annealed sample has the largest E_ph (2.31 kV/cm) and highest P_max. Under broad band AM1.5 illumination, the N_2 sample also generates the highest P_max mainly because of its high E_ph (= 1.99 kV/cm). It should also be noted the 450 nm illumination produces a much higher j_sc and E_ph in all samples for the reasons discussed in section 5.6.2 and section 6.3.1. These results represent the lower limits of the photovoltaic performance of this system as they were collected from lateral devices where the sample thickness is much larger than the absorption depth. As shown in section 6.3.3, improved j_sc and higher power conversion efficiency can be achieved from thinner of samples with a vertical device configuration.

It is possible the large E_{ph} of the N_2 annealed ceramics could enable potential application in photostriction which is superimposition of the photovoltaic and piezoelectric effect.[160] Under illumination, the ferroelectric materials generate E_{ph} in an open-circuit condition. This photogenerated field can in-turn induce a strain ($\varepsilon_{\mathrm{ph}}$) through the converse piezoelectric effect which follows the simple relation:

$$\varepsilon_{\mathrm{ph}} = d_{33} \times E_{\mathrm{ph}}$$

where d_{33} is the piezoelectric coefficient. Thus, ferroelectric materials that combine a high d_{33} and E_{ph} can produce large photo-induced strains $\varepsilon_{\mathrm{ph}}$. PT-BNT is considered a good piezoelectric material with a reported d_{33} ~250 pC/N at the MPB composition (*i.e.* 0.5PT-0.5BNT).[112] N_2 annealed 0.5PT-0.5BNT has $E_{ph} \geq 2$ kV/cm over a broad range of wavelengths and under AM1.5, which leads to a $\varepsilon_{\mathrm{ph}}$ in the range of 10^{-5} to 10^{-4}. This value compares favorably to PLZT ceramics,[161] a conventional piezoelectric material which only responses to UV light, and $BiFeO_3$ single crystal[162] that has smaller E_{ph} and d_{33}.

6.8.2 Temperature Dependence of the Photovoltaic Response

The temperature dependence of V_{oc}, j_{sc}, maximum power and σ_{ph} of as-prepared 0.5PT-0.5BNT at 450 nm were described in section 6.4. Here the temperature dependence is re-visited for the O_2 and N_2 annealed samples to understand the role of $\mathrm{Ni}_{\mathrm{Ni}}^{\bullet}$. Measurements were made using lateral devices; after poling the samples were cooled to 100 K and the photovoltaic *IV* response was collected upon heating under 450 nm illumination. The temperature dependence of V_{oc} and j_{sc} (top panel) and the maximum power per unit sample thickness, (P_{max} lower panel), is shown in **Figure 6.20**; for all three samples V_{oc} is reduced and j_{sc} increased as T increases. However, the magnitude of V_{oc} and the temperature at which it decays to zero is determined by the annealing history and the concentration of $\mathrm{Ni}_{\mathrm{Ni}}^{\bullet}$. The annealing history also affects the temperature dependence of P_{max}. For the as-prepared sample, the highest value of P_{max} is reached at 350 K, this shifts to higher (~400 K) and lower temperature (~300 K) for the N_2 sample and O_2 samples, respectively.

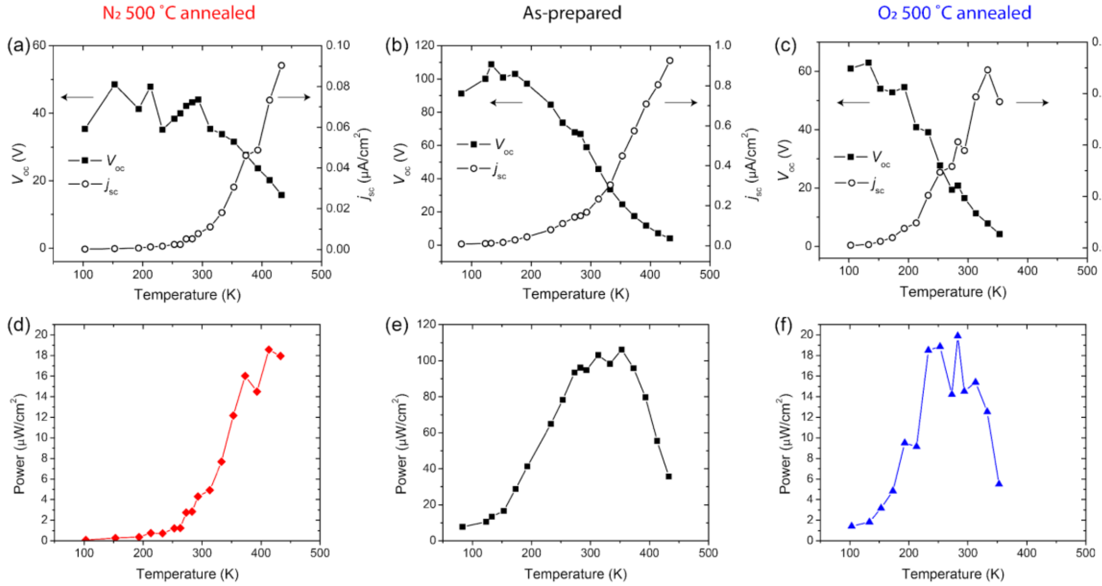

Figure 6.20 Temperature dependence of V_{oc}, j_{sc}, and maximum power of N_2 annealed, as-prepared, and O_2 annealed 0.5PT-0.5BNT under 450 nm illumination.

The temperature dependence of σ_{ph} is shown in **Figure 6.21**; $\ln(\sigma_{\mathrm{ph}})$ does not show a single linear change with T^{-1} in any of the samples and they all have temperature dependent thermal activation. The curves can be divided into three linear regions and fitted by the Arrhenius law ($\ln\sigma_{\mathrm{ph}} = \ln\sigma_0 - \frac{E_{\mathrm{a}}^{(\mathrm{i})}}{kT}$), yielding a specific activation energy $E_{\mathrm{a}}^{(\mathrm{i})}$ where i represents the temperature range. The resultant activation energies are qualitatively consistent with the previously discussed properties of the as-prepared vertical devices (section 6.7.5) and support a polaron hopping transport mechanism. The photoconduction in the lateral devices is limited to the illuminated surface as the sample (~ 1mm) is much larger than the absorption depth of the 450 nm laser. Therefore, the measured photoconductivities have non-negligible contributions from σ_d for the unilluminated region which leads to a deviation of the activation energy from the values for the vertical devices (see **Figure 6.18**). The results indicate the changes in $[\mathrm{Ni}_\mathrm{Ni}^\bullet]$ induced by the post-sintering anneals do not alter the activation energies significantly and the transport mechanism is unchanged. However, the decreased $[\mathrm{Ni}_\mathrm{Ni}^\bullet]$ after N_2 annealing significantly reduces σ_ph.

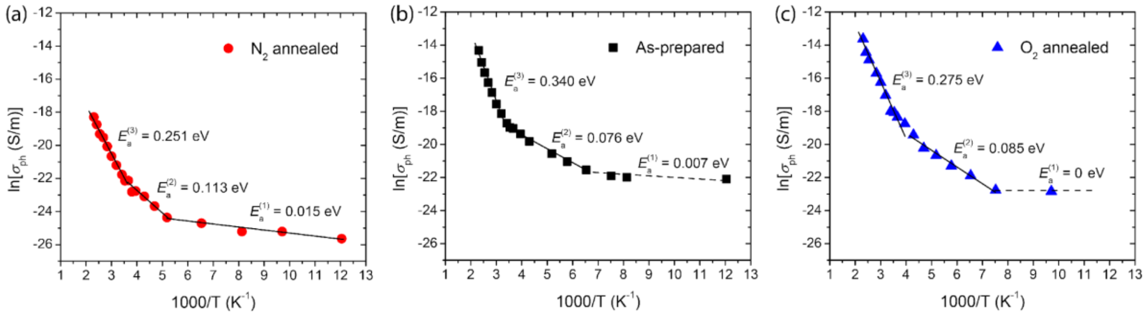

Figure 6.21 Temperature dependence of photoconductivities σ_ph of (a) N_2 annealed, (b) as-prepared and (c) O_2 annealed 0.5PT-0.5BNT samples under 450 nm illumination.

6.9 Nonstoichiometric $(\mathrm{Pb}_{0.5+x}\mathrm{Bi}_{0.5-x})(\mathrm{Ti}_{0.75}\mathrm{Ni}_{0.25})\mathrm{O}_{3-x/2}$

The redox activity of 0.5PT-0.5BNT arises from the volatilization of small amounts of either PbO and/or Bi_2O_3 during the high temperature sintering through the formation of the extrinsic V_Pb'' and $\mathrm{V}_\mathrm{Bi}'''$ defects. It was not possible to reliably quantify the actual concentration of the defects, for example by measuring the uptake of O_2 during the lower temperature oxidation using TGA; however, the amounts are likely to be extremely small and in related systems their concentration is <2 at%.[163] The compensation of the A-site cation vacancies can be ionic through the formation of $V_{O}^{\bullet\bullet}$ at low pO_2, electronic through holes trapped at the Ni^{2+} sites that form $Ni_{Ni}^{\bullet}$ at high pO_2, or by both at intermediate pO_2's. 0.5PT-0.5BNT was found to exhibit p-type behavior and its properties are strongly affected by the small levels of defects. However, it is difficult to control the concentrations of V_{Pb}'' and V_{Bi}''' when they are caused by volatilization. Therefore, attempts were made to introduce p-type carriers in a controlled fashion by changing the Pb^{2+} to Bi^{3+} ratio and preparing deliberately nonstoichiometric compositions with $(Pb_{0.5+x}Bi_{0.5-x})(Ti_{0.75}Ni_{0.25})O_{3-x/2}$. By increasing the ratio of Pb^{2+} : Bi^{3+} ratio, while maintaining the B-site stoichiometry, it was hoped the excess effective negative charge could allow the formation of solid solutions with pre-designed concentrations of $V_{O}^{\bullet\bullet}$.

Table 6-2 Compositions of nonstoichiometric $(Pb_{0.5+x}Bi_{0.5-x})(Ti_{0.75}Ni_{0.25})O_{3-x/2}$ and its dominate defect concentrations at different pO_2.

	Low pO_2 limit		Hight pO_2 limit	
x	Composition	$[V_{O}^{\bullet\bullet}]$	Composition	$[Ni_{Ni}^{\bullet}]$
x=0.1	$(Pb_{0.6}Bi_{0.4})(Ti_{0.75}Ni_{0.25})O_{2.95}V_{0.05}$	1.67%	$(Pb_{0.6}Bi_{0.4})(Ti_{0.75}Ni_{0.15}^{2+}Ni_{0.1}^{3+})O_3$	10%
x=0.05	$(Pb_{0.55}Bi_{0.45})(Ti_{0.75}Ni_{0.25})O_{2.975}V_{0.025}$	0.83%	$(Pb_{0.55}Bi_{0.45})(Ti_{0.75}Ni_{0.2}^{2+}Ni_{0.05}^{3+})O_3$	5%
x=0.02	$(Pb_{0.52}Bi_{0.48})(Ti_{0.75}Ni_{0.25})O_{2.99}V_{0.01}$	0.33%	$(Pb_{0.52}Bi_{0.48})(Ti_{0.75}Ni_{0.23}^{2+}Ni_{0.02}^{3+})O_3$	2%

Three compositions (*e.g.*, x = 0.1, 0.05, and 0.02) were prepared with the targeted defect concentrations are shown in **Table 6-2**. Unfortunately, the resultant XRD patterns (**Figure**

6.22) indicated that even small deviations of Pb:Bi from a 1:1 stoichiometry produce non-perovskite impurities (primarily binary PbO-Bi_2O_3 and NiO). For $x = 0.02$, the amount of impurities is so small so that reliable phase identification is not possible, but their presence is clear in the XRD pattern (**Figure 6.22**). For the higher x values the impurities are more prominent and could be identified as $Pb_2Bi_6O_{11}$ + NiO and $Pb_5Bi_8O_{17}$ + NiO for $x = 0.05$ and $x = 0.1$ respectively. These observations suggest that the tolerance of the systems for the formation of vacancies is very limited, with $[V_O^{\bullet\bullet}] < 0.33\%$. It is possible other synthesis methods and or non-stoichiometric formulations could stabilize and allow quantitative control of the defect formation, but these were not pursued.

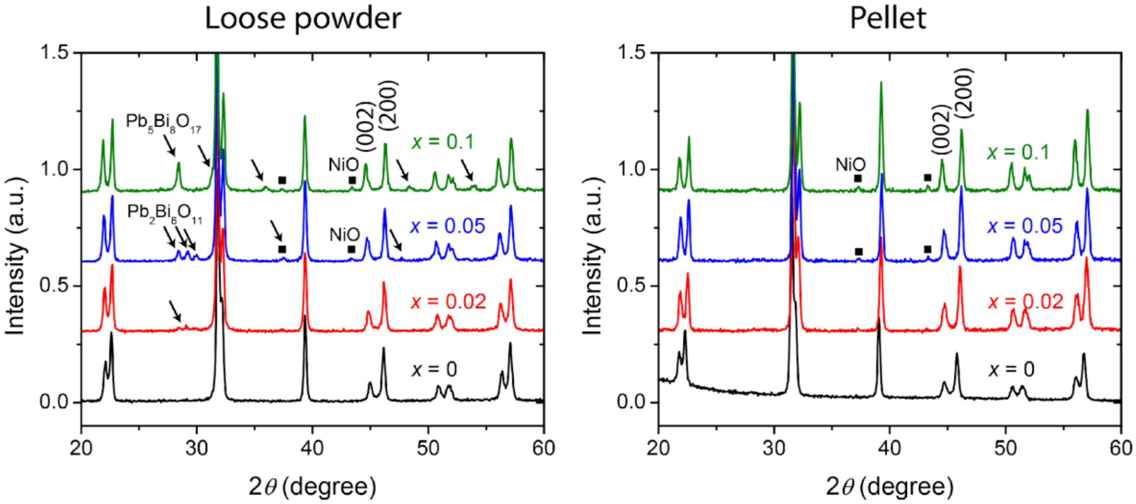

Figure 6.22 XRD patterns of nonstoichiometric $(Pb_{0.5+x}Bi_{0.5-x})(Ti_{0.75}Ni_{0.25})O_{3-x/2}$. Left: loose powders; right: pellets. Arrows indicate PbO-Bi_2O_3 compounds; squares indicate NiO.

6.10 Conclusions

Building on the exploration of the bandgap reduction and photovoltaic properties of MPB compositions in the PT-BF-BNT system, this chapter focused on the ferroelectric polarization and the role of defect formation and temperature on the PV performance of compositions in the PT-BNT pseudobinary. Tetragonal 0.5PT-0.5BNT exhibits the best photovoltaic response of any previously reported ferroelectric ceramic due to its relatively low bandgap (direct E_g = 2.8 eV; indirect E_g = 2.2 eV), large ferroelectric polarization and excellent retention properties.

The photoresponse of 0.5PT-0.5BNT is governed by its polarization state. The correlations between the hysteresis loops of the ferroelectric polarization versus electric field and the photocurrent versus the poling electric field confirmed the concurrence of the polarization and photocurrent. It is possible this system could enable optical readout of multistate in ferroelectric memory devices.

Comparisons of the properties of tetragonal 0.5PT-0.5BNT and pseudocubic 0.45PT-0.55BNT elucidated the influence of the ferroelectric polarization retention on photovoltaic effect. Although both compositions have identical optical properties and similar saturation polarization, tetragonal 0.5PT-0.5BNT shows a significantly larger photovoltaic response due to its retention of a high remanent polarization.

Under near-bandgap illumination (450 nm), the V_{oc} of the 0.5PT-0.5BNT is scalable with respect to the thickness of the sample, leading to a V_{oc} = 62 V for a 260 µm thick lateral device. Moreover, by utilizing a vertical device configuration with an ITO top electrode, a 36 µm thick sample can increase the j_{sc} to 6 µA/cm^2 due to the increase in effective optical absorption. The photo-induced electric field, E_{ph} = 3 kV/cm, in the vertical device is among the highest reported for materials with an above-bandgap V_{oc}.

Measurements of the temperature dependence of the PV response of 0.5PT-0.5BNT show that V_{oc} increases and j_{sc} drops as T decreases; these two quantities are correlated through the photoconductivity which has different activation energies over three ranges of temperature. Frequency dependent dielectric and mechanical measurements suggest a transition into a re-entrant relaxor phase embedded in a long-range ferroelectric matrix is responsible for the saturation of V_{oc} below 200 K and the saturation of j_{sc} is above 400K is due to thermal depolarization. Dielectric and anelastic relaxations above room temperature suggest the existence of polaronic transport in 0.5PT-0.5BNT and the activation energies for the dark and photo conductivities are consistent with a thermally activated polaron hopping mechanism.

The concentration of hole polarons in 0.5PT-0.5BNT are strongly affected by post annealing treatments in different pO_2's. The dielectric and anelastic relaxations caused by polarons can be suppressed and enhanced by annealing in O_2 and N_2 respectively; the changes in carrier concentration also induce alterations in the optical absorption of the samples. The annealing alters the dark and photo conductivities and allows the resultant highest maximum power P_{max} to be tuned to different temperatures. A V_{oc} as high as 100 V was obtained below 200 K for as-prepared 0.5PT-0.5BNT.

Chapter 7 Summary and Future Directions

7.1 Summary and Conclusions

With a broad goal of expanding the utilization of ferroelectric materials for PV applications, this thesis focused on the bandgap engineering of conventional ferroelectric perovskite oxides through chemical substitution and characterization of their PV response. Various solid solutions based on $KNbO_3$, $BaTiO_3$, $PbTiO_3$ and $BiFeO_3$ were synthesized and showed a reduction in the bandgap of the ferroelectric end-member. Testing procedures for the ferroelectric ceramic devices were developed to enable quantitative characterization of their PV properties. Although the results obtained in this work indicate the power conversion efficiencies fall short of traditional PN junction solar cells, compared to other known ferroelectric ceramics significant improvements in PV performance were achieved.

Building on the first principles calculations[58] and the discovery of $KNbO_3$-$Ba(Ni_{1/2}Nb_{1/2})O_{3-\delta}$,[46] of the role of Ni^{2+}-oxygen vacancies was investigated in non-stoichiometric $Ba(Ni_{1/3}Nb_{2/3})O_3$ and its solid solutions with ferroelectric $KNbO_3$ and $(K_{0.5}Na_{0.5})NbO_3$ (Chapter 3). Although the range of non-stoichiometry of $Ba(Ni_{1/3}Nb_{2/3})O_3$ is limited, small deviations in the Ni:Nb ratio and, therefore, the oxygen vacancy content, induce abrupt changes in the optical absorption properties. Solid solutions of $KNbO_3$ and $(K_{0.5}Na_{0.5})NbO_3$, could be formed with $Ba(Ni_{1/2}Nb_{1/2})O_{3-\delta}$ up to ~50%. The TGA results suggest as-prepared samples of KBNNO contain both Ni^{2+} and Ni^{3+} and the diffuse reflectance spectra revealed *d-d* transitions at 1.6 eV and 2.8 eV.

Ni^{2+}-oxygen vacancy substitutions were also utilized to reduce the bandgap of $BaTiO_3$ and the phase stability, absorption properties, ferroelectric, and PV responses of Ni- and Ni-Nb-substituted $BaTiO_3$ were explored in Chapter 4. Although the acceptor substitution of Ni^{2+} stabilized a hexagonal 6H polymorph in both systems, post-annealing treatments allowed restoration of a tetragonal 3C phase for $Ba(Ti_{0.99}Ni_{0.01})O_{2.99}$ and $(0.9)BaTiO_3$-$(0.1)Ba(Ni_{1/2}Nb_{1/2})O_{2.75}$. The oxygen vacancies accompanying the Ni and Ni-Nb substitutions significantly lower the optical bandgap of $BaTiO_3$ to ~1.5 eV and the visible light absorption can be systematically tuned between 380 and 1000 nm by varying the Ni:Nb ratio. Room temperature ferroelectricity was observed in $Ba(Ti_{0.99}Ni_{0.01})O_{2.99}$ with a saturation polarization = 18 $\mu C/cm^2$ and remnant polarization = 1 $\mu C/cm^2$. The Ni-Nb substituted composition $(0.9)BaTiO_3$-$(0.1)Ba(Ni_{1/2}Nb_{1/2})O_{2.75}$ shows a ferroelectric response with a remnant polarization of 5 $\mu C/cm^2$ at 77 K, which gradually decreases as temperature increases. Both compositions exhibit ferroelectrically switchable photoresponses under an AM 1.5 G sunlight simulator; the highest switchable steady-state current of 8 nA/cm^2 observed for $(0.9)BaTiO_3$-$(0.1)Ba(Ni_{1/2}Nb_{1/2})O_{2.75}$ exceeds those reported in previous studies of $BaTiO_3$ ceramic samples.

Although effective in reducing the bandgap, the loss of the ferroelectric polarization in $KNbO_3$ and $BaTiO_3$ at relatively small concentrations of Ni and Ni/Nb prevented access to a wide range of polar solid solutions. To mitigate this issue, bandgap reduction in systems with a more robust ferroelectric order, namely the tetragonally-enhanced $PbTiO_3$-$BiFeO_3$ system with a complete occupancy of the A site by ferroelectrically active Pb/Bi cations, was explored. Using a $Bi(Ni_{1/2}Ti_{1/2})O_3$ additive, the ternary

$PbTiO_3-BiFeO_3-Bi(Ni_{1/2}Ti_{1/2})O_3$ system exhibits a large bulk P_r and a tunable narrow E_g (Chapter 5). To optimize the ferroelectric polarization, ceramics were prepared in the vicinity of the ternary MPB, and their PV properties were characterized over a broad range of optical wavelengths. MPB compositions with a direct optical gap ranging from 2.25 to 2.85 eV and P_r =32−39 μC/cm^2 showed a BPVE with V_{oc} = 6V at room temperature and a wavelength-dependent switchable photoresponse. Under 1 sun AM 1.5 G illumination the short-circuit photocurrent (j_{sc}) of these systems (0.1 μA/cm^2) increased by an order of magnitude as E_g was lowered from 2.85 to 2.25 eV.

In addition to the bandgap and optical absorption properties, other factors such as the ferroelectric polarization, device configuration, temperature and defects were found to affect the PV response of the ceramic ferroelectrics. These factors were investigated for $0.5PbTiO_3-0.5Bi(Ni_{1/2}Ti_{1/2})O_3$, a tetragonal composition close to the MPB, which shows the best PV performance of all the compositions explored in this work (Chapter 6). A robust sizeable polarization was found to be crucial in enhancing the photovoltaic current and voltage. The PV properties of $0.5PbTiO_3-0.5Bi(Ni_{1/2}Ti_{1/2})O_3$ showed strong temperature dependence with V_{oc} increasing and j_{sc} decreasing at lower T; a V_{oc} as high as 100 V was obtained for a 250 µm thick sample below 160 K. Temperature dependent measurements of the PV, dielectric and mechanical response of $0.5PbTiO_3-0.5Bi(Ni_{1/2}Ti_{1/2})O_3$ showed the photovoltaic properties are influenced by thermal depolarization and by a re-entrant relaxor phase transition and also mediated by the polaron hopping mechanism. Post-annealing in atmospheres with different pO_2's allowed modification of the carrier concentration, which in turn could be used to tune the PV performance for applications in different ranges of temperature.

7.2 Future Directions

The approaches used to reduce the bandgap of ferroelectric perovskite oxides in this thesis could be applied to other systems. Based on the observation of significant enhancements of the optical absorption of nonstoichiometric $Ba(Ni_{1/3}Nb_{2/3})O_3$ with excess Ni^{2+} and oxygen vacancies, if the nonstoichiometry can be stabilized the chemically similar system $Pb(Ni_{1/3}Nb_{2/3})O_3$ could show similar optical responses. Considering the relaxor nature of $Pb(Ni_{1/3}Nb_{2/3})O_3$ and the availability of single crystals,[164] investigations of this material may yield interesting properties.

Many potential directions could also be explored for other mixed Pb/Bi perovskites. For example, the $PbTiO_3$-$BiFeO_3$-$BiMnO_3$ system, which was recently prepared in ceramic form by mechnosynthesis, shows a very high remanent polarization (78 $\mu C/cm^2$).[122] Other possibilities include investigation of alternate tetragonally enhanced perovskites such as $PbTiO_3$-$Bi(Zn_{1/2}Ti_{1/2})O_3$, $PbTiO_3$-$Bi(Zn_{2/3}Nb_{1/3})O_3$, and $PbTiO_3$-$Bi(Zn_{3/4}W_{1/4})O_3$, using bandgap changing $Bi(Me)O3$ substituents with Me = Cr, Mn, Fe, Co, Ni, etc.

Bandgap engineering may find more opportunities in oxides where a d^0 cation is not necessary for ferroelectricity. An example is the Ruddlesden-Popper phases that are compatible with hybrid improper ferroelectricity. Calculations have already suggested candidates such as $LaSrAlO_4$ Ruddlesden-Popper phase which shows large bandgap tunability ~2 eV and could be potentially stabilized through epitaxy.[165]

In additions to changes in the bulk chemistry, the PV performance of the ferroelectric ceramics explored in this work could be enhanced through the preparation of epitaxial, ultrathin films where hot carriers of the ballistic current could be efficiently collected.[17] Considering the good performance of the ceramic samples, the growth of $PbTiO_3$-$Bi(Ni_{1/2}Ti_{1/2})O_3$ thin films certainly seems worthwhile. Additional optimization could be realized by combining the growth of the films with the fabrication and deposition of nanoscale electrode arrays, which have recently been shown to improve the PV performance of other ferroelectric oxides.[13,26]

Finally, the origin of the PV effect, especially the large open circuit voltages, of the ferroelectric ceramics explored in this thesis is still unclear due to granular nature of the ceramics. Separation of the bulk and boundary contributions could potentially be investigated in two ways: (a) through study of the angular dependence of the PV to quantify the BPVE which is dependent on the angle between polar axis and light polarization; (b) by utilizing Kelvin probe force microscopy to monitor the sample surface potential under illumination, which will potentially distinguish the potential difference in the bulk of the domains and at their boundaries.

Appendix A: Supporting Materials of Chapter 5

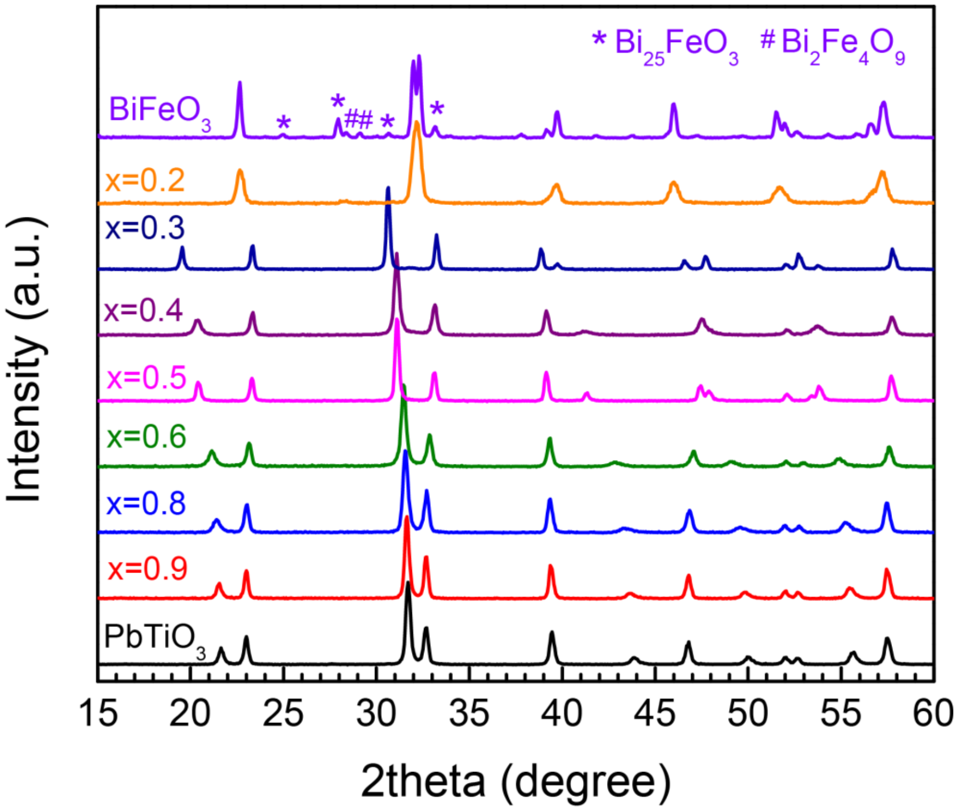

Figure A.1 XRD patterns of (*x*)PT-(1–*x*)BF solid solutions.

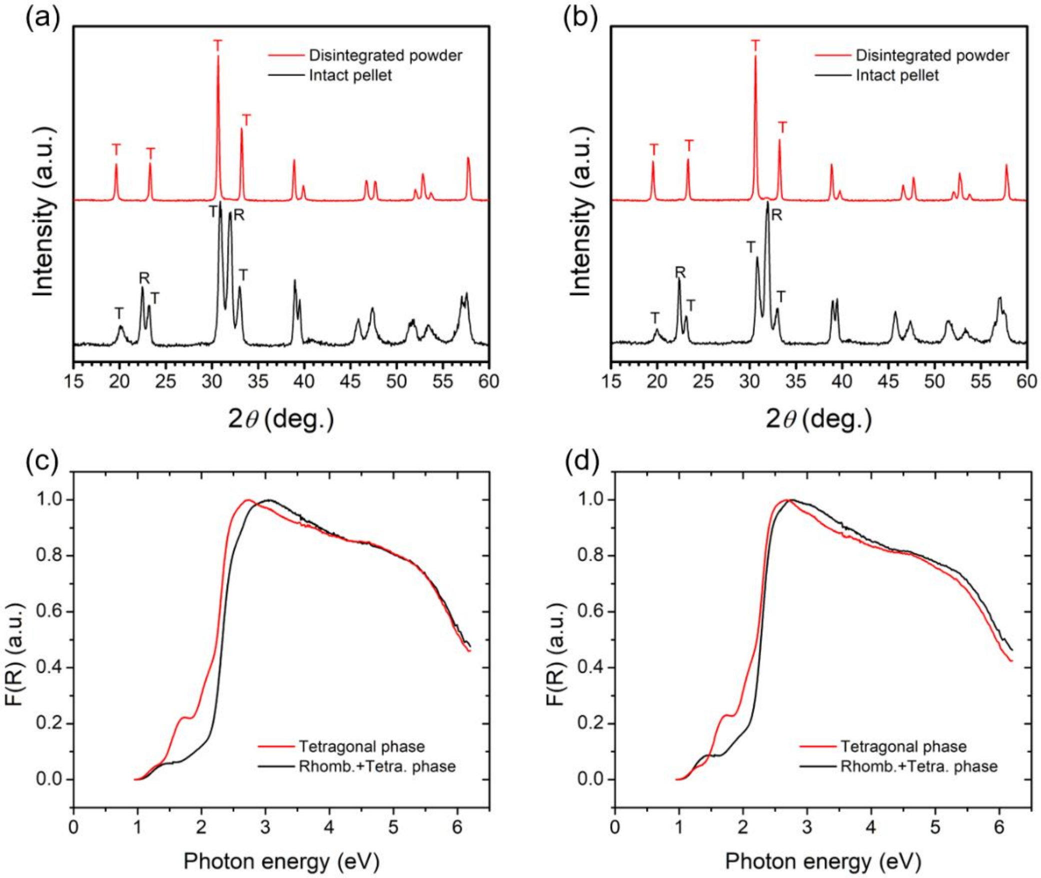

Figure A.2 XRD patterns of (*x*)PT-(1–*x*)BF collected after disintegration of pellets with (a) $x = 0.325$ and (b) $x = 0.3$; upper trace (red) collected from powder, lower (black) from remaining pellet. Corresponding Kubelka-Munk spectra, (c) $x = 0.325$ (d) $x = 0.3$.

Due to the large internal stress developed during cooling through T_C, the edges of highly tetragonal PT-BF pellets, *e.g.* $x = 0.325$ ($c/a = 1.18$) and 0.3 ($c/a = 1.19$), disintegrate into powder. The disintegrated powders have a single-phase tetragonal structure and the pellet core contains a mixture of tetragonal (T) and rhombohedral (R) phases. The core remains unfragmented as the internal stress accompanying the ferroelectric transition is accommodated by formation of a metastable rhombohedral phase. The peaks from the residual tetragonal phase in the pellet core are broadened due to the highly strained state.

For these compositions the tetragonal structure is the stable bulk phase; the R structure in the unfragmented region only forms for grains < 1 µm and eventually vanishes if the grains experience abnormal growth.

The pure T and metastable T+R mixture show subtle differences in their absorption spectra (Figure A.2c and d). The fundamental absorption edge maximum for the T phase occurs at a slightly lower energy and the positions of the weak peaks from Fe^{3+} *d*-*d* transition shows small shifts due to the change in the symmetry of the Fe^{3+} site in the two structures.

Table A.1 Lattice parameters of *P*4*mm* tetragonal phase for x = 0.325 and 0.3.

	x = 0.325	x = 0.3
Lattice parameters	$a = b$ = 3.8140(7) Å; c = 4.517(1) Å; $\alpha = \beta = \gamma$ = 90°	$a = b$ = 3.8103(8) Å; c = 4.536(2) Å; $\alpha = \beta = \gamma$ = 90°
Unit cell volume	65.70 $Å^3$	65.86 $Å^3$
***c/a* ratio**	1.18(4)	1.19(0)

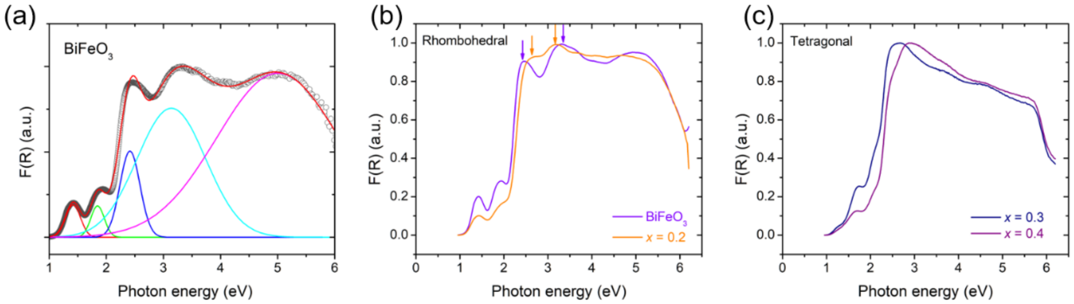

Figure A.3 Kubelka-Munk spectra of (a) $BiFeO_3$, (b) rhombohedral, $x = 0.2$ and (c) tetragonal, $x = 0.3$ and 0.4, regions of the (x)PT-$(1–x)$BF system.

The absorption spectrum of $BiFeO_3$ (Figure A.3a) is best fit by Gaussian peaks for the different transitions; the first (1.42 eV) and second (1.85 eV) correspond to the $^6A_{1g}$ to $^4T_{1g}$ and $^6A_{1g}$ to $^4T_{2g}$ transitions[61,118,166]. The third peak (onset at 2.2 eV maximum at 2.4 eV) is associated with high energy crystal-field excitations and/or excitonic excitations[118]; this peak overlaps with the absorption edge which lies at a slightly higher energy and defines the charge transfer gap. The extensive overlap of the latter two peaks can make it difficult to distinguish the absorption edge and has led to reports of a ~2.2 eV bandgap for $BiFeO_3$[167]. The actual charge transfer gap of $BiFeO_3$ is characterized by the fourth peak, which yields a bandgap in agreement with those, 2.5 ~ 2.7 eV, obtained from quantitative analysis of high quality thin films.[61,118,119]

For the rhombohedral compositions (*i.e.* $x < 0.3$), two maxima are observed above the sharp increase of F(R) at 2.2 eV; these are marked by arrows in Figure A.3b. For the rhombohedral $x = 0.2$ (Figure A.3b), the overlap between the third and fourth absorption peaks, highlighted by arrows, is even stronger. For the tetragonal compositions (*i.e.* $x \geq 0.3$), the absorption edge is characterized by a single maximum, which corresponds to the charge transfer gap, see Figure A.3c. The *d*-*d* transitions ($^6A_{1g}$ to $^4T_{1g}$ and $^6A_{1g}$ to $^4T_{2g}$) are located at 1.7 eV and 2.1 eV[168,169] and are shifted to higher energy compared to the rhombohedral phase due to the change in the local coordination of Fe^{3+} from a [111] to [001] distorted octahedron.

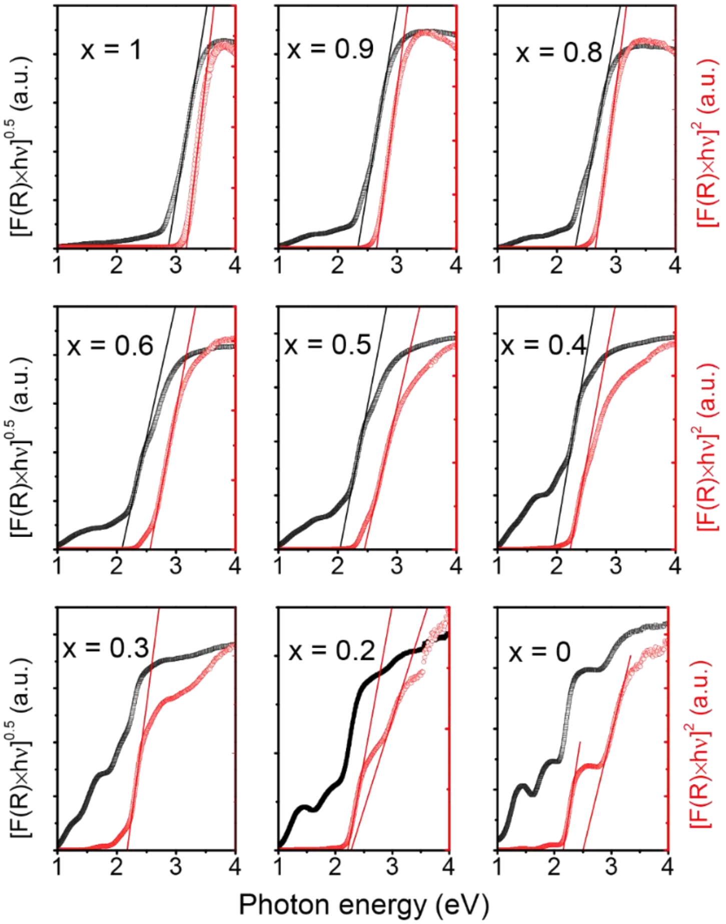

Figure A.4 Direct (red curve) and indirect (black) Tauc plots of (x)PT-(1–x)BF solid solutions.

The optical transitions were modeled through Tauc’s law:

$$\alpha h\nu = A\left(h\nu - E_{\mathrm{g}}\right)^{n}$$

where α = absorption coefficient, $h\nu$ = photon energy, A is a scaling constant, and n represents the transition type (n = ½ for direct transition and 2 for indirect transition). In diffuse reflectance spectroscopy, α is replaced by Kubelka-Munk function F(R). The corresponding direct and indirect optical gaps E_g are obtained by extrapolation of the linear region for $[\mathrm{F}(R)h\nu]^{\frac{1}{n}}$ to the photon energy axis.

The direct Tauc plots ($n = ½$; red curves) of the tetragonal compositions ($x \geq 0.3$) show a good linear fit. However, for the rhombohedral phases ($x < 0.3$) two linear regions are observed due to the overlap of the crystal-field and charge transfer peaks; the higher energy region was used to estimate the direct gap. The indirect Tauc plots ($n = 2$; black curves) for $x \geq 0.4$ show a well-defined region of linearity, no satisfactory fitting was possible for $x < 0.3$.

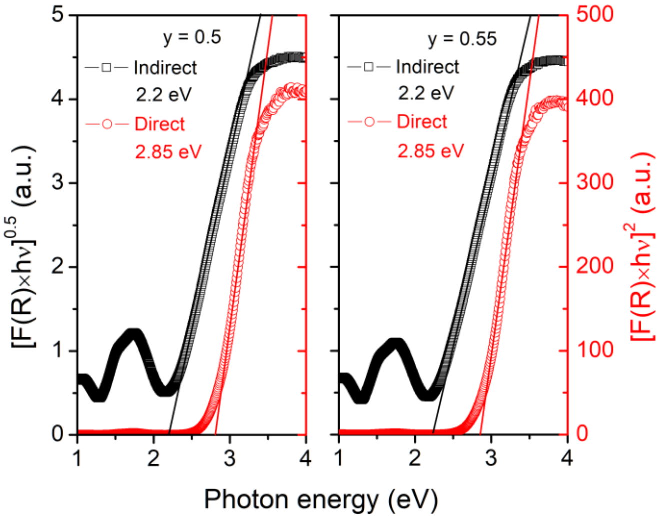

Figure A.5 Tauc plots for (1–*y*)PT-(*y*)BNT with *y* = 0.5 and 0.55.

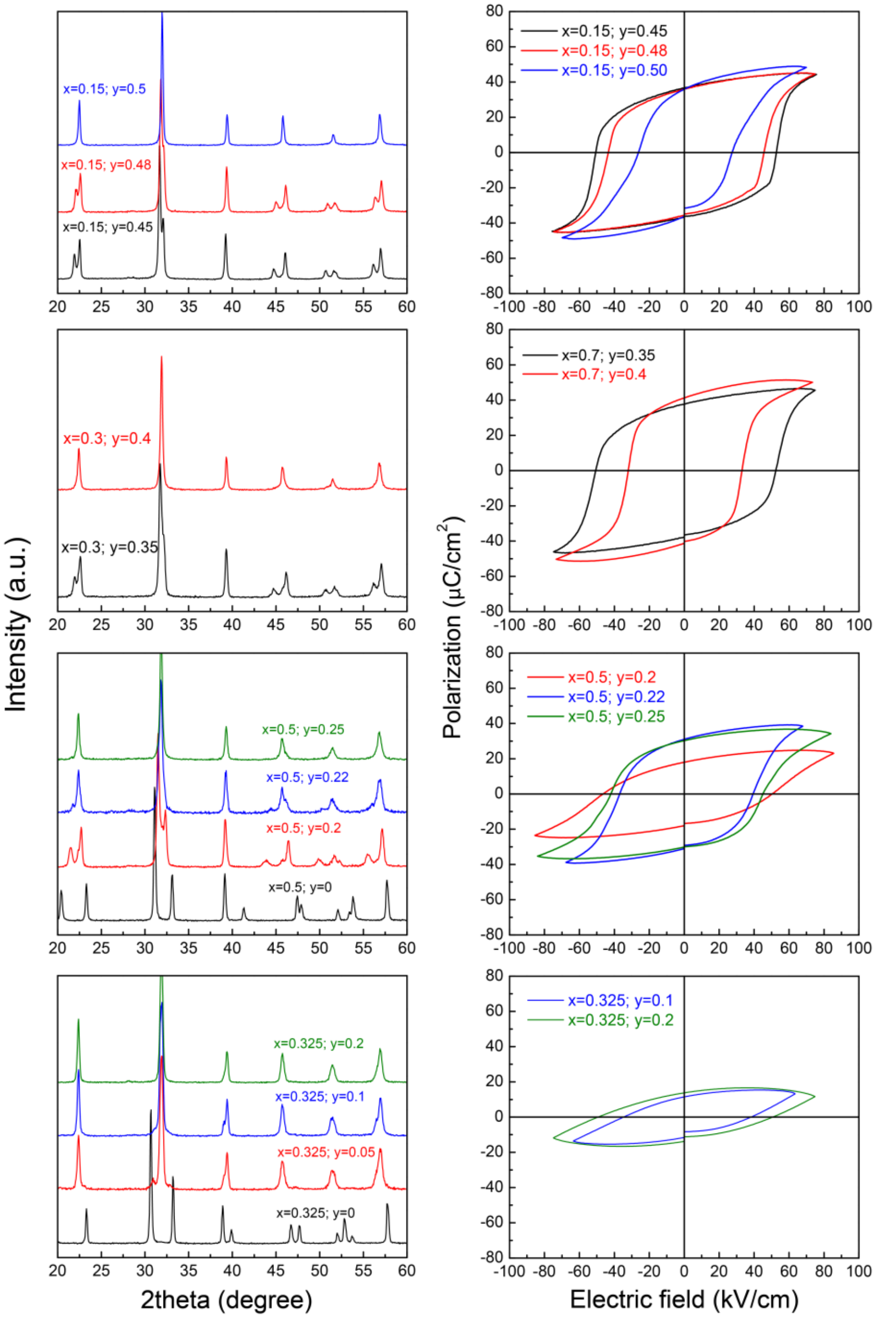

Figure A.6 Evolution of the XRD patterns and ferroelectric hysteresis loops in the (1–y)[(x)PT-(1–x)BF]-(y)BNT system along tie-lines with x = 0.15, 0.3, 0.325 and 0.5; y values are shown in each figure.

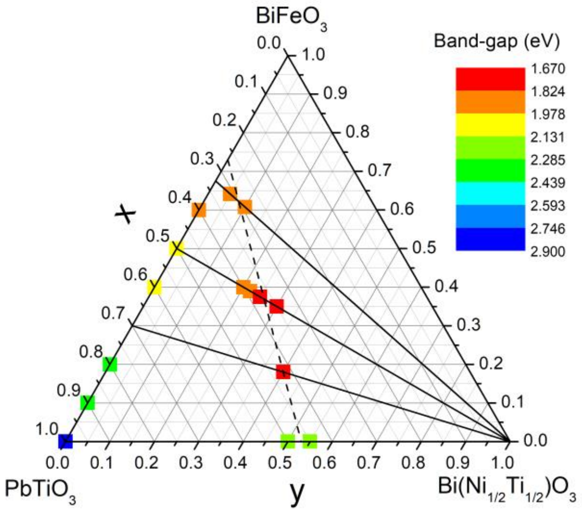

Figure A.7 Color map of the indirect bandgaps for compositions in the (1–*y*)[(*x*)PT-(1–*x*)BF]-(*y*)BNT system.

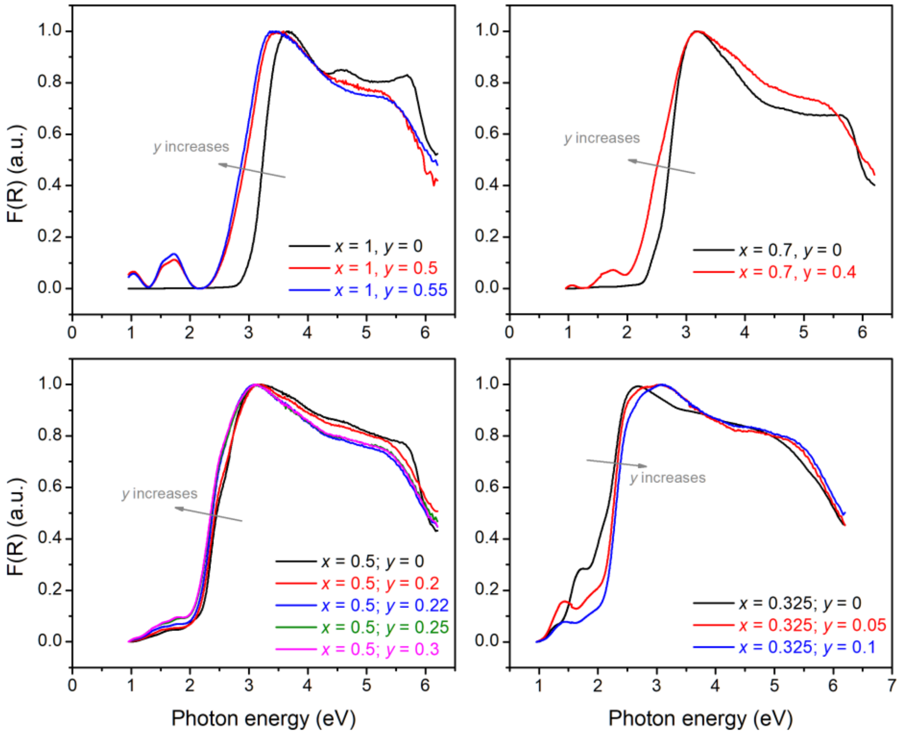

Figure A.8 Kubelka-Munk spectra of (1–*y*)[(*x*)PT-(1–*x*)BF]-(*y*)BNT along tie-lines with *x* = 0.325, 0.5, 0.7 and 1.0; y values are shown in each figure.

For *x* = 1, 0.7, and 0.5 the absorption edge is red-shifted with increasing *y*. For *x* = 0.325 an increase in y produces a blue-shift in the absorption edge and a change in the *d*-*d* transitions due to the tetragonal to rhombohedral phase transition discussed in Figure A.2 and Figure A.3.

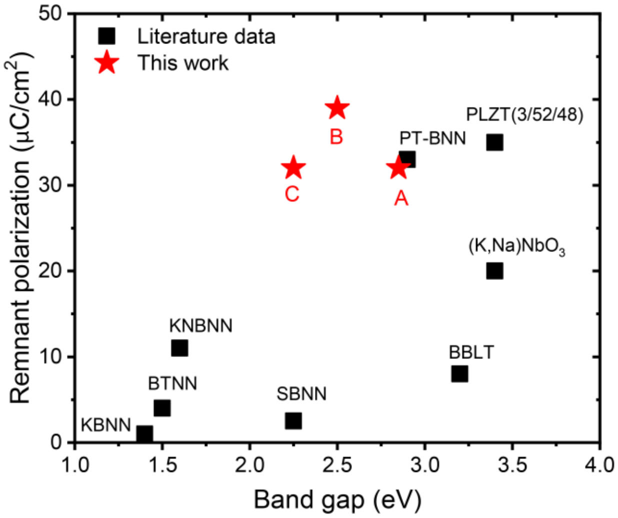

Figure A.9 Comparison of the remnant polarization and bandgap of compositions A, B and C (red stars) in the PT-BNT-BF system to other ferroelectric ceramics (single crystals and thin films are not included) (see Table 1-1 for references).

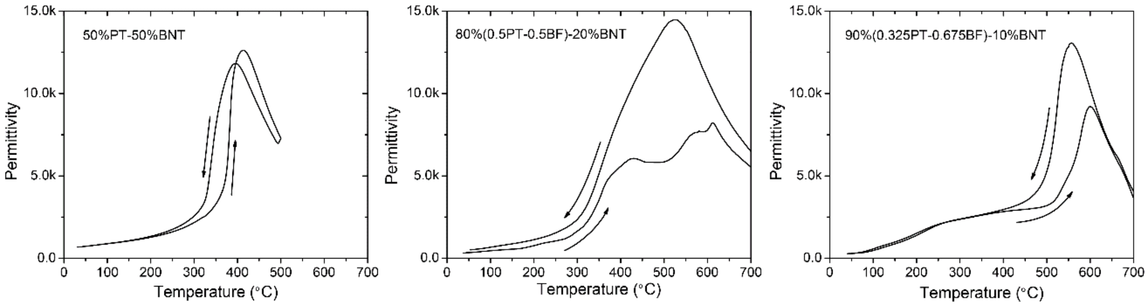

Figure A.10 Dielectric response (at $f = 100$ kHz) of compositions close to the MPB in PT-BNT-BF. Arrows indicate the direction of thermal ramp.

Measurements of the dielectric response as a function of temperature was used to analyze the Curie temperature (T_C) of MPB compositions. The three compositions shown illustrate the evolution of the Curie temperature (T_C) across the ternary. 50%PT-50%BNT shows a single dielectric maximum with a thermal hysteresis with T_C, defined by the median of the maxima, ~ 400 °C. 90%(0.325PT-0.675BF)-10%BNT, located at the other end of MPB close to the PT-BF binary, also shows single dielectric maxima at a higher temperature (T_C ~ 577 °C) and with a slightly larger thermal hysteresis. The 80%(0.5PT-0.5BF)-20%BNT composition, which lies in the center of ternary MPB, shows two dielectric maxima at 425 °C and 600 °C on heating and a broad single maximum (~525 °C) on cooling. These multiple dielectric maxima have been observed in other (Pb, Bi) systems, *e.g.* $PbTiO_3$-$BiFeO_3$-$Bi(Mg_{1/2}Ti_{1/2})O_3$ and $PbTiO_3$-$Bi(Zn_{1/2}Ti_{1/2})O_3$-$Bi(Mg_{1/2}Ti_{1/2})O_3$.[170],[171]

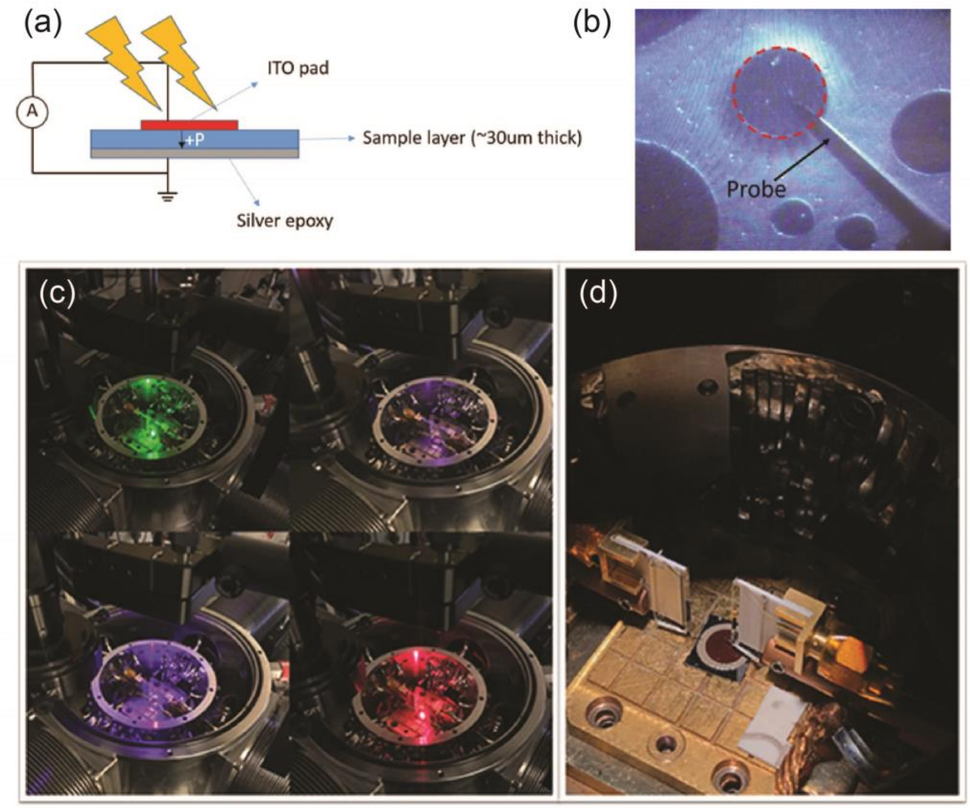

Figure A.11 (a) Schematic of the device structure used for the photovoltaic measurements; (b) optical micrograph of the top surface during poling; the red-circled area is the ITO top electrode (200 µm in diameter), the contrast in the image is altered due to a piezoelectric induced shape change; (c) and (d) are images of the experimental set-up used for photovoltaic measurement in the probe station under monochromatic and AM1.5 G illumination respectively.

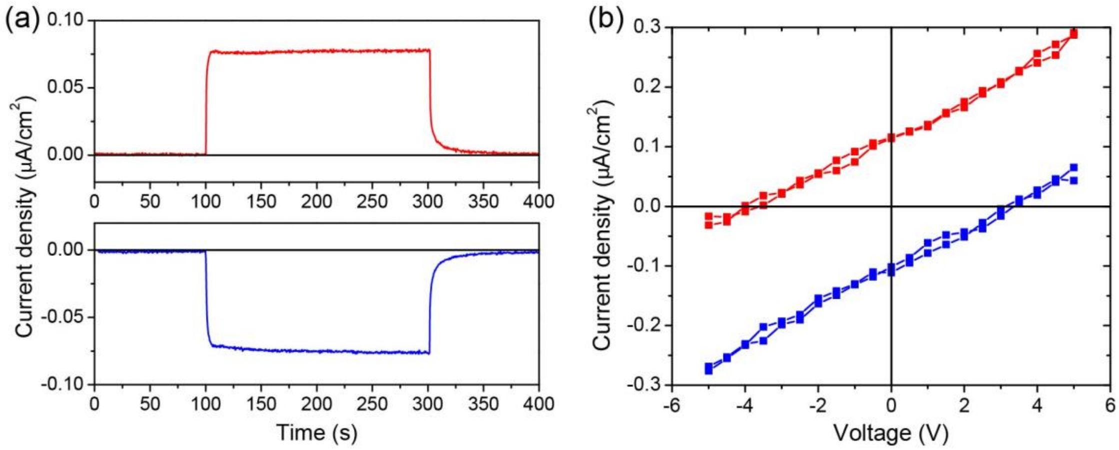

Figure A.12 Photoresponse, switchability and IV characteristics of composition C (x = 0.5, y = 0.4, direct E_g = 2.25 eV) under 532 nm laser illumination. (a) Top: photocurrent of polarization up state for laser on/off; bottom: polarization down state. (b) IV responses of polarization up (red) and down (blue) state under illumination.

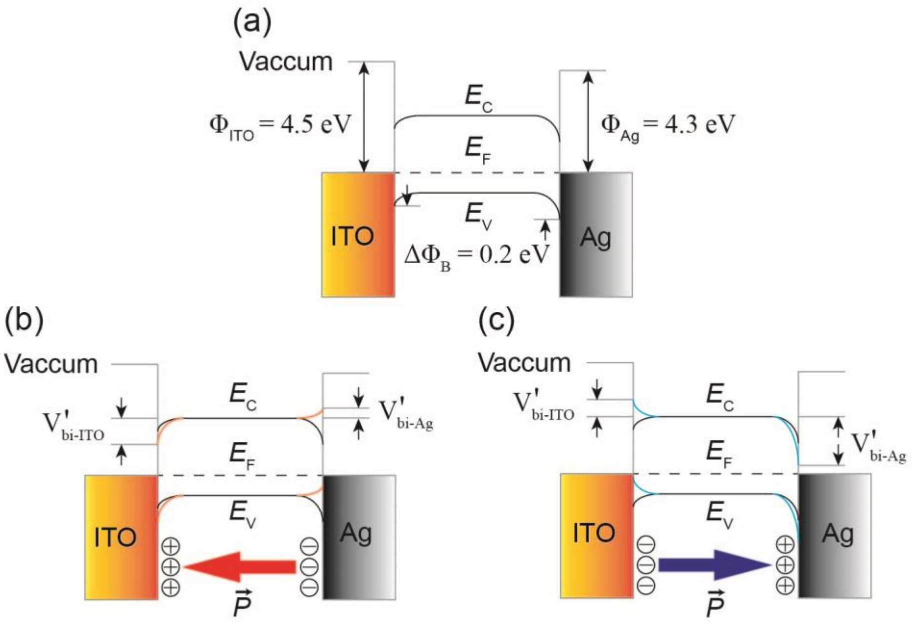

Figure A.13 Schematic illustration of band diagrams of the ITO/FE/Ag device configuration. (a) Band diagram of virgin state (unpoled). (b) Band diagram of polarization up state (red: modulation from polarization; black: original unpoled). (c) Band diagram of polarization down state (blue: modulation from polarization; black: original unpoled).

The (Pb,Bi)-based perovskites are treated as p-type semiconductors due to the presence of A-site vacancies from small levels of Pb and Bi volatilization during higher temperature sintering.[136,172] For the virgin (unpoled) state (Figure A.13a), the difference in the barrier height, $\Delta\Phi_{\mathrm{B}}$, is within 0.2 eV, which is consistent with our observation of negligible steady-state photocurrents before poling. The linear dark *IV* characteristic also indicates the electrode contact is close to ohmic or the barrier height is exceptionally small.

After poling, there is a slightly difference between the j_{sc} of polarization up and down states which could be induced by the modification of the electrode/FE interfaces from the ferroelectric polarization. The original built-in potential $V_{\mathrm{bi}} = \frac{1}{q}(\Phi_{\mathrm{FE}} - \Phi_{\mathrm{M}})$ of each contact is modulated by the polarization surface charge P after poling, where q is positive elementary charge and Φ_{FE} and Φ_M are the work functions of the ferroelectric layer and metal electrode respectively. The modified built-in potential at each contact, according a simple dielectric-gap model,[173] is given by $V'_{\mathrm{bi}} = V_{\mathrm{bi}} + \frac{P\delta}{\varepsilon_0 \varepsilon_{\mathrm{st}}}$ where δ is the distance between the polarization surface charge and the physical interface with the electrode, and $\mathcal{E}_{\mathrm{st}}$ is the static dielectric constant. The sign of P can be positive or negative according to the polarity of the polarization. The resultant modulated $V'_{\mathrm{bi-ITO}}$ and $V'_{\mathrm{bi-Ag}}$ for the polarization up and down states are shown in Figure A.13b and c respectively. This simple band diagram is consistent with the change in the polarity of the photocurrent after the polarization reversal. The slightly larger j_{sc} of the polarization down state observed in **Figure 5.4**b can be explained by the larger built-in potential at the ITO and Ag contacts compared to polarization up state. It should be noted that this model only accounts for the contribution from the interfacial-barrier-controlled conduction. The overall photovoltaic response is due to the combination of the bulk and interfacial contributions; for these thick (>30 μm) ferroelectric ceramic samples, the bulk effect dominates and is responsible for the above-bandgap V_{oc} and linear IV characteristics.

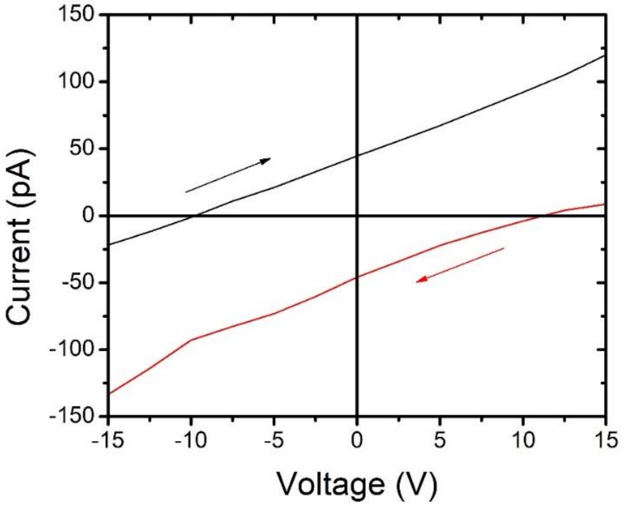

Figure A.14 *IV* response of composition A, poled and measured at 173 K under 450 nm illumination.

Arrows indicate the direction of the voltage sweep.

BIBLIOGRAPHY

[1] IEA: Directorate of Global Energy Economics, *World Energy Outlook 2017*, OECD, **2017**.

[2] International Energy Agency, *Global Energy and CO2 Status Report 2018*, **2019**.

[3] D. Gielen, F. Boshell, D. Saygin, *Nat. Mater.* **2016**, *15*, 117.

[4] NREL, "Best Research-Cell Efficiency Chart," can be found under http://www.nrel.gov/pv/cell-efficiency.html, **n.d.**

[5] W. Shockley, H. J. Queisser, *J. Appl. Phys.* **1961**, *32*, 510.

[6] B. I. Sturman, V. M. Fridkin, *The Photovoltaic and Photorefractive Effects in Noncentrosymmetric Materials*, Gordon And Breach Science Publishers, Philadelphia, **1992**.

[7] S. M. Young, A. M. Rappe, *Phys. Rev. Lett.* **2012**, *109*, 1.

[8] P. Lopez-Varo, L. Bertoluzzi, J. Bisquert, M. Alexe, M. Coll, J. Huang, J. A. Jimenez-Tejada, T. Kirchartz, R. Nechache, F. Rosei, Y. Yuan, *Phys. Rep.* **2016**, *653*, 1.

[9] S. Y. Yang, J. Seidel, S. J. Byrnes, P. Shafer, C.-H. Yang, M. D. Rossell, P. Yu, Y.-H. Chu, J. F. Scott, J. W. Ager, L. W. Martin, R. Ramesh, *Nat. Nanotechnol.* **2010**, *5*, 143.

[10] G. Zhang, H. Wu, G. Li, Q. Huang, C. Yang, F. Huang, F. Liao, J. Lin, *Sci. Rep.* **2013**, *3*, 1265.

[11] M. Yang, A. Bhatnagar, M. Alexe, *Adv. Electron. Mater.* **2015**, *1*, 1500139.

[12] A. Bhatnagar, A. Roy Chaudhuri, Y. Heon Kim, D. Hesse, M. Alexe, *Nat. Commun.* **2013**, *4*, 2835.

[13] M. Alexe, D. Hesse, *Nat. Commun.* **2011**, *2*, 256.

[14] A. Bihari Swain, D. Murali, B. R. K. Nanda, P. Murugavel, *Phys. Rev. Appl.* **2019**, *11*, 044007.

[15] P. Poosanaas, A. Dogan, S. Thakoor, K. Uchino, *J. Appl. Phys.* **1998**, *84*, 1508.

[16] H. Liu, J. Chen, Y. Ren, L. Zhang, Z. Pan, L. Fan, X. Xing, *Adv. Electron. Mater.* **2015**, *1*, 1400051.

[17] Z. Gu, D. Imbrenda, A. L. Bennett-Jackson, M. Falmbigl, A. Podpirka, T. C. Parker, D. Shreiber, M. P. Ivill, V. M. Fridkin, J. E. Spanier, *Phys. Rev. Lett.* **2017**, *118*, 096601.

[18] W. Ji, K. Yao, Y. C. Liang, *Adv. Mater.* **2010**, *22*, 1763.

[19] H. G. Festl, P. Hertel, E. Krätzig, R. von Baltz, *Phys. status solidi* **1982**, *113*, 157.

[20] D. J. Kim, M. Alexe, *Appl. Phys. Lett.* **2017**, *110*, 183902.

[21] R. Inoue, S. Ishikawa, R. Imura, Y. Kitanaka, T. Oguchi, Y. Noguchi, M. Miyayama, *Sci. Rep.* **2015**, *5*, 1.

[22] H. Matsuo, Y. Noguchi, M. Miyayama, *Nat. Commun.* **2017**, *8*, 207.

[23] V. I. Belinicher, B. I. Sturman, *Ferroelectrics* **1988**, *83*, 29.

[24] L. Z. Tan, F. Zheng, S. M. Young, F. Wang, S. Liu, A. M. Rappe, *npj Comput. Mater.* **2016**, *2*, 16026.

[25] B. M. Fregoso, **2018**, 1.

[26] J. E. Spanier, V. M. Fridkin, A. M. Rappe, A. R. Akbashev, A. Polemi, Y. Qi, Z. Gu, S. M. Young, C. J. Hawley, D. Imbrenda, G. Xiao, A. L. Bennett-Jackson, C. L. Johnson, *Nat. Photonics* **2016**, *10*, 611.

[27] V. M. Fridkin, *Crystallogr. Reports* **2001**, *46*, 654.

[28] A. M. Burger, R. Agarwal, A. Aprelev, E. Schruba, A. Gutierrez-Perez, V. M. Fridkin, J. E. Spanier, *Sci. Adv.* **2019**, *5*, eaau5588.

[29] M. Sotome, M. Nakamura, J. Fujioka, M. Ogino, Y. Kaneko, T. Morimoto, Y. Zhang, M. Kawasaki, N. Nagaosa, Y. Tokura, N. Ogawa, *Proc. Natl. Acad. Sci.* **2019**, *116*, 1929.

[30] H. Matsuo, Y. Kitanaka, R. Inoue, Y. Noguchi, M. Miyayama, T. Kiguchi, T. J. Konno, *Phys. Rev. B* **2016**, *94*, 214111.

[31] J. Zhang, X. Su, M. Shen, Z. Dai, L. Zhang, X. He, W. Cheng, M. Cao, G. Zou, *Sci. Rep.* **2013**, *3*, 2109.

[32] D. Cao, C. Wang, F. Zheng, W. Dong, L. Fang, M. Shen, *Nano Lett.* **2012**, *12*, 2803.

[33] F. Liu, I. Fina, D. Gutiérrez, G. Radaelli, R. Bertacco, J. Fontcuberta, *Adv. Electron. Mater.* **2015**, *1*, 1500171.

[34] P. S. Brody, F. Crowne, *J. Electron. Mater.* **1975**, *4*, 955.

[35] J. Park, S. S. Won, C. W. Ahn, I. W. Kim, *J. Am. Ceram. Soc.* **2013**, *96*, 146.

[36] X. He, C. Chen, C. Li, H. Zeng, Z. Yi, *Adv. Funct. Mater.* **2019**, *1900918*, 1900918.

[37] X. Liu, F. Zhang, P. Long, T. Lu, H. Zeng, Y. Liu, R. L. Withers, Y. Li, Z. Yi, *Adv. Mater.* **2018**, *1801619*, 1801619.

[38] M. A. Peña, J. L. G. Fierro, *Chem. Rev.* **2001**, *101*, 1981.

[39] M. E. Lines, A. M. Glass, *Principles and Applications of Ferroelectrics and Related Materials*, Oxford University Press, Oxford, **2001**.

[40] R. Seshadri, N. A. Hill, *Chem. Mater.* **2001**, *13*, 2892.

[41] B. B. Van Aken, T. T. M. Palstra, A. Filippetti, N. A. Spaldin, *Nat. Mater.* **2004**, *3*, 164.

[42] Y. Tokura, S. Seki, *Adv. Mater.* **2010**, *22*, 1554.

[43] N. A. Benedek, C. J. Fennie, *Phys. Rev. Lett.* **2011**, *106*, 107204.

[44] M. J. Pitcher, P. Mandal, M. S. Dyer, J. Alaria, P. Borisov, H. Niu, J. B. Claridge, M. J. Rosseinsky, *Science (80-.).* **2015**, *347*, 420.

[45] D. V. Efremov, J. van den Brink, D. I. Khomskii, *Nat. Mater.* **2004**, *3*, 853.

[46] I. Grinberg, D. V. West, M. Torres, G. Gou, D. M. Stein, L. Wu, G. Chen, E. M. Gallo, A. R. Akbashev, P. K. Davies, J. E. Spanier, A. M. Rappe, *Nature* **2013**, *503*, 509.

[47] W. S. Choi, M. F. Chisholm, D. J. Singh, T. Choi, G. E. Jellison, H. N. Lee, *Nat. Commun.* **2012**, *3*, 689.

[48] M. Wu, X. Lou, T. Li, J. Li, S. Wang, W. Li, B. Peng, G. Gou, *J. Alloys Compd.* **2017**, *724*, 1093.

[49] L. Wu, A. R. Akbashev, A. A. Podpirka, J. E. Spanier, P. K. Davies, *J. Am. Ceram. Soc.* **2019**, *102*, 4188.

[50] T. Qi, I. Grinberg, A. M. Rappe, *Phys. Rev. B* **2011**, *83*, 224108.

[51] R. Nechache, C. Harnagea, S. Li, L. Cardenas, W. Huang, J. Chakrabartty, F. Rosei, *Nat. Photonics* **2015**, *9*, 61.

[52] G. Gou, N. Charles, J. Shi, J. M. Rondinelli, *Inorg. Chem.* **2017**, *56*, 11854.

[53] R. F. Berger, J. B. Neaton, *Phys. Rev. B* **2012**, *86*, 165211.

[54] H. Han, S. Song, J. H. Lee, K. J. Kim, G. W. Kim, T. Park, H. M. Jang, *Chem. Mater.* **2015**, *27*, 7425.

[55] X. Huang, T. R. Paudel, S. Dong, E. Y. Tsymbal, *Phys. Rev. B* **2015**, *92*, 125201.

[56] H. Han, D. Kim, K. Chu, J. Park, S. Y. Nam, S. Heo, C. H. Yang, H. M. Jang, *ACS Appl. Mater. Interfaces* **2018**, *10*, 1846.

[57] G. Zhang, F. Liu, T. Gu, Y. Zhao, N. Li, W. Yang, S. Feng, *Adv. Electron. Mater.* **2017**, *3*, 1600498.

[58] J. W. Bennett, I. Grinberg, A. M. Rappe, *J. Am. Chem. Soc.* **2008**, *130*, 17409.

[59] J. Wang, J. B. Neaton, H. Zheng, V. Nagarajan, S. B. Ogale, B. Liu, D. Viehland, V. Vaithyanathan, D. G. Schlom, U. V Waghmare, N. A. Spaldin, K. M. Rabe, M. Wuttig, R. Ramesh, *Science (80-.).* **2003**, *299*, 1719.

[60] H. T. Yi, T. Choi, S. G. Choi, Y. S. Oh, S.-W. Cheong, *Adv. Mater.* **2011**, *23*, 3403.

[61] X. S. Xu, T. V. Brinzari, S. Lee, Y. H. Chu, L. W. Martin, A. Kumar, S. McGill, R. C. Rai, R. Ramesh, V. Gopalan, S. W. Cheong, J. L. Musfeldt, *Phys. Rev. B* **2009**, *79*, 134425.

[62] J. F. Ihlefeld, N. J. Podraza, Z. K. Liu, R. C. Rai, X. Xu, T. Heeg, Y. B. Chen, J. Li, R. W. Collins, J. L. Musfeldt, X. Q. Pan, J. Schubert, R. Ramesh, D. G. Schlom, *Appl. Phys. Lett.* **2008**, *92*, 142908.

[63] R. S. Weis, T. K. Gaylord, *Appl. Phys. A Solids Surfaces* **1985**, *37*, 191.

[64] L. You, F. Zheng, L. Fang, Y. Zhou, L. Z. Tan, Z. Zhang, G. Ma, D. Schmidt, A. Rusydi, L. Wang, L. Chang, A. M. Rappe, J. Wang, *Sci. Adv.* **2018**, *4*, eaat3438.

[65] P. Machado, M. Scigaj, J. Gazquez, E. Rueda, A. Sánchez-Díaz, I. Fina, M. Gibert-Roca, T. Puig, X. Obradors, M. Campoy-Quiles, M. Coll, *Chem. Mater.* **2019**, *31*, 947.

[66] L. Zhang, J. Chen, L. Fan, Z. Pan, J. Wang, K. Ibrahim, J. Tian, X. Xing, *J. Alloys Compd.* **2018**, *742*, 351.

[67] S. Kooriyattil, R. K. Katiyar, S. P. Pavunny, G. Morell, R. S. Katiyar, *Appl. Phys. Lett.* **2014**, *105*, 072908.

[68] H. An, J. Y. Han, B. Kim, J. Song, S. Y. Jeong, C. Franchini, C. W. Bark, S. Lee, *Sci. Rep.* **2016**, *6*, 28313.

[69] K. Uchino, Y. Miyazawa, S. Nomura, *Jpn. J. Appl. Phys.* **1983**, *22*, 102.

[70] S. Pal, A. B. Swain, P. P. Biswas, D. Murali, A. Pal, B. R. K. Nanda, P. Murugavel, *Sci. Rep.* **2018**, *8*, 8005.

[71] S. Das, S. Ghara, P. Mahadevan, A. Sundaresan, J. Gopalakrishnan, D. D. Sarma, *ACS Energy Lett.* **2018**, *3*, 1176.

[72] C. J. Hawley, L. Wu, G. Xiao, I. Grinberg, A. M. Rappe, P. K. Davies, J. E. Spanier, *Phys. Rev. B* **2017**, *96*, 054117.

[73] Y. Bai, P. Tofel, J. Palosaari, H. Jantunen, J. Juuti, *Adv. Mater.* **2017**, *29*, 1700767.

[74] R. Newman, R. M. Chrenko, *Phys. Rev.* **1959**, *114*, 1507.

[75] S. Piskunov, E. Heifets, R. . Eglitis, G. Borstel, *Comput. Mater. Sci.* **2004**, *29*, 165.

[76] M. W. Lufaso, *Chem. Mater.* **2004**, *16*, 2148.

[77] B. Xu, W. F. Zhang, X.-Y. Liu, J. H. Ye, W. H. Zhang, L. Shi, X. G. Wan, J. Yin, Z. G. Liu, *Phys. Rev. B* **2007**, *76*, 125109.

[78] I.-T. Kim, K. S. Hong, S.-J. Yoon, *J. Mater. Sci.* **1995**, *30*, 514.

[79] H. Wu, P. K. Davies, *J. Am. Ceram. Soc.* **2006**, *89*, 2250.

[80] D. R. Gaskell, *Introduction to The Thermodynamics of Materials*, Taylor & Francis, New York, **2003**.

[81] B. Faust, H. Muller, O. F. Schirmer, *Ferroelectrics* **1994**, *153*, 297.

[82] K.-D. Becker, M. Schrader, H.-S. Kwon, H.-I. Yoo, *Phys. Chem. Chem. Phys.* **2009**, *11*, 3082.

[83] F. Schmidt, A. Riefer, W. G. Schmidt, A. Schindlmayr, M. Imlau, F. Dobener, N. Mengel, S. Chatterjee, S. Sanna, *Phys. Rev. Mater.* **2019**, *3*, 054401.

[84] S. K. Nayak, H. T. Langhammer, W. A. Adeagbo, W. Hergert, T. Müller, R. Böttcher, *Phys. Rev. B* **2015**, *91*, 155105.

[85] I. E. Grey, C. Li, L. M. D. Cranswick, R. S. Roth, T. A. Vanderah, *J. Solid State Chem.* **1998**, *135*, 312.

[86] H. T. Langhammer, T. Müller, K.-H. Felgner, H.-P. Abicht, *J. Am. Ceram. Soc.* **2004**, *83*, 605.

[87] Y. Li, Q. Liu, T. Yao, Z. Pan, Z. Sun, Y. Jiang, H. Zhang, Z. Pan, W. Yan, S. Wei, *Appl. Phys. Lett.* **2010**, *96*, 091905.

[88] G. M. Keith, M. J. Rampling, K. Sarma, N. Mc. Alford, D. C. Sinclair, *J. Eur. Ceram. Soc.* **2004**, *24*, 1721.

[89] R. Böttcher, H. T. Langhammer, T. Müller, *J. Phys. Condens. Matter* **2011**, *23*, 115903.

[90] T. Qi, M. Curnan, S. Kim, J. Bennett, I. Grinberg, A. Rappe, *Phys. Rev. B* **2011**, *84*, 1.

[91] G. Y. Gou, J. W. Bennett, H. Takenaka, A. M. Rappe, *Phys. Rev. B* **2011**, *83*, 205115.

[92] G. H. JONKER, *J. Am. Ceram. Soc.* **1972**, *55*, 57.

[93] L. Zhang, W. Liu, W. Chen, X. Ren, J. Sun, E. A. Gurdal, S. O. Ural, K. Uchino, *Appl. Phys. Lett.* **2012**, *101*, 242903.

[94] D. Hu, S. Yang, C. Zhou, L. Zhang, W. Liu, W. Chen, X. Ren, *RSC Adv.* **2016**, *6*, 109030.

[95] L. Jin, F. Li, S. Zhang, *J. Am. Ceram. Soc.* **2014**, *97*, 1.

[96] W. L. Warren, D. Dimos, R. M. Waser, *MRS Bull.* **1996**, *21*, 40.

[97] R. Waser, T. Baiatu, K.-H. Hardtl, *J. Am. Ceram. Soc.* **1990**, *73*, 1645.

[98] S. Yoon, C. a. Randall, K. Hur, *J. Appl. Phys.* **2010**, *108*, 064101.

[99] F. Urbach, *Phys. Rev.* **1953**, *92*, 1324.

[100] C. Tian, Z. Yue, Y. Zhou, L. Li, *J. Solid State Chem.* **2013**, *197*, 242.

[101] Y. Yuan, T. Li, Q. Wang, J. Xing, A. Gruverman, J. Huang, *Sci. Adv.* **2017**, *3*, e1602164.

[102] P. S. Brody, *J. Solid State Chem.* **1975**, *12*, 193.

[103] R. Inoue, S. Ishikawa, Y. Kitanaka, T. Oguchi, Y. Noguchi, M. Miyayama, *Jpn. J. Appl. Phys.* **2013**, *52*, 09KF03.

[104] M. R. Suchomel, P. K. Davies, *Appl. Phys. Lett.* **2005**, *86*, 262905.

[105] D. M. Stein, M. R. Suchomel, P. K. Davies, *Appl. Phys. Lett.* **2006**, *89*, 132907.

[106] I. Grinberg, M. R. Suchomel, P. K. Davies, A. M. Rappe, *J. Appl. Phys.* **2005**, *98*, 094111.

[107] Z. Pan, J. Chen, R. Yu, L. Patra, P. Ravindran, A. Sanson, R. Milazzo, A. Carnera, L. Hu, L. Wang, H. Yamamoto, Y. Ren, Q. Huang, Y. Sakai, T. Nishikubo, T. Ogata, X. Fan, Y. Li, G. Li, H. Hojo, M. Azuma, X. Xing, *Chem. Mater.* **2019**, *31*, 1296.

[108] B. Narayan, S. Adhikari, G. Madras, R. Ranjan, *Phys. Rev. Appl.* **2017**, *7*, 024018.

[109] M. R. Suchomel, *UPenn Diss.* **2005**, 1.

[110] J. Zhu, S. Feng, Q. Liu, J. Zhang, H. Xu, Y. Li, X. Li, J. Liu, Q. Huang, Y. Zhao, C. Jin, *J. Appl. Phys.* **2013**, *113*, 143514.

[111] T. Takenaka, M. Yamada, *Jpn. J. Appl. Phys.* **1993**, *32*, 4218.

[112] S. M. Choi, C. J. Stringer, T. R. Shrout, C. a. Randall, *J. Appl. Phys.* **2005**, *98*, 034108.

[113] Q. Zhang, M. Jiang, Z. Li, *J. Electroceramics* **2012**, *29*, 179.

[114] P. Hu, J. Chen, J. Deng, X. Xing, *J. Am. Chem. Soc.* **2010**, *132*, 1925.

[115] T. P. Comyn, T. Stevenson, M. Al-Jawad, S. L. Turner, R. I. Smith, W. G. Marshall, A. J. Bell, R. Cywinski, *Appl. Phys. Lett.* **2008**, *93*, 91.

[116] V. Kothai, B. Narayan, K. Brajesh, S. D. Kaushik, V. Siruguri, R. Ranjan, *Phys. Rev. B* **2014**, *90*, 155115.

[117] V. Kothai, R. Prasath Babu, R. Ranjan, *J. Appl. Phys.* **2013**, *114*, 114102.

[118] M. O. Ramirez, A. Kumar, S. A. Denev, N. J. Podraza, X. S. Xu, R. C. Rai, Y. H. Chu, J. Seidel, L. W. Martin, S.-Y. Yang, E. Saiz, J. F. Ihlefeld, S. Lee, J. Klug, S. W. Cheong, M. J. Bedzyk, O. Auciello, D. G. Schlom, R. Ramesh, J. Orenstein, J. L. Musfeldt, V. Gopalan, *Phys. Rev. B* **2009**, *79*, 224106.

[119] R. V Pisarev, A. S. Moskvin, A. M. Kalashnikova, T. Rasing, *Phys. Rev. B* **2009**, *79*, 235128.

[120] M. D. Scafetta, A. M. Cordi, J. M. Rondinelli, S. J. May, *J. Phys. Condens. Matter* **2014**, *26*, 505502.

[121] E. González, A. Rodrigue-Witchel, C. Reber, *Coord. Chem. Rev.* **2007**, *251*, 351.

[122] C. M. Fernández-Posada, A. Castro, J.-M. Kiat, F. Porcher, O. Peña, M. Algueró, H. Amorín,

Nat. Commun. **2016**, *7*, 12772.

[123] H. Amorín, C. Correas, C. M. Fernández-Posada, O. Peña, A. Castro, M. Algueró, *J. Appl. Phys.* **2014**, *115*, DOI 10.1063/1.4868319.

[124] H. Amorín, C. Correas, P. Ramos, T. Hungría, A. Castro, M. Algueró, *Appl. Phys. Lett.* **2012**, *101*, 172908.

[125] J. H. Noh, S. H. Im, J. H. Heo, T. N. Mandal, S. Il Seok, *Nano Lett.* **2013**, *13*, 1764.

[126] G. E. Eperon, S. D. Stranks, C. Menelaou, M. B. Johnston, L. M. Herz, H. J. Snaith, *Energy Environ. Sci.* **2014**, *7*, 982.

[127] C. A. Niedermeier, M. Råsander, S. Rhode, V. Kachkanov, B. Zou, N. Alford, M. A. Moram, *Sci. Rep.* **2016**, *6*, 31230.

[128] P. Hu, H. Kang, J. Chen, J. Deng, X. Xing, *J. Mater. Chem.* **2011**, *21*, 16205.

[129] M. Cherry, M. S. Islam, C. R. A. Catlow, *J. Solid State Chem.* **1995**, *118*, 125.

[130] J. M. Azpiroz, E. Mosconi, J. Bisquert, F. De Angelis, *Energy Environ. Sci.* **2015**, *8*, 2118.

[131] A. G. Chynoweth, *Phys. Rev.* **1956**, *102*, 705.

[132] L. M. Peter, *J. Solid State Electrochem.* **2013**, *17*, 315.

[133] M. Alexe, *Nano Lett.* **2012**, *12*, 2193.

[134] R. H. Bube, *Photoconductivity of Solids*, Wiley, New York, **1960**.

[135] C. Ge, K. J. Jin, Q. H. Zhang, J. Y. Du, L. Gu, H. Z. Guo, J. T. Yang, J. X. Gu, M. He, J. Xing, C. Wang, H. Bin Lu, G. Z. Yang, *ACS Appl. Mater. Interfaces* **2016**, *8*, 34590.

[136] L. Pintilie, I. Vrejoiu, G. Le Rhun, M. Alexe, *J. Appl. Phys.* **2007**, *101*, 064109.

[137] H. Xiao, W. Dong, Y. Guo, Y. Wang, H. Zhong, Q. Li, M.-M. Yang, *Adv. Mater.* **2018**, *1805802*, 1805802.

[138] K. Chu, B.-K. Jang, J. H. Sung, Y. A. Shin, E.-S. Lee, K. Song, J. H. Lee, C.-S. Woo, S. J. Kim, S.-Y. Choi, T. Y. Koo, Y.-H. Kim, S.-H. Oh, M.-H. Jo, C.-H. Yang, *Nat. Nanotechnol.* **2015**, *10*, 972.

[139] M. Yang, D. J. Kim, M. Alexe, *Science (80-.).* **2018**, *360*, 904.

[140] R. E. Eitel, S. J. Zhang, T. R. Shrout, C. A. Randall, I. Levin, *J. Appl. Phys.* **2004**, *96*, 2828.

[141] R. Pandey, A. K. Singh, *Appl. Phys. Lett.* **2014**, *105*, 162901.

[142] R. Pandey, B. Narayan, D. K. Khatua, S. Tyagi, A. Mostaed, M. Abebe, V. Sathe, I. M. Reaney, R. Ranjan, *Phys. Rev. B* **2018**, *97*, 224109.

[143] B. Narayan, J. S. Malhotra, R. Pandey, K. Yaddanapudi, P. Nukala, B. Dkhil, A. Senyshyn, R.

Ranjan, *Nat. Mater.* **2018**, *17*, 427.

[144] W. Zhao, R. Zuo, J. Fu, M. Shi, *J. Eur. Ceram. Soc.* **2014**, *34*, 2299.

[145] G. Tutuncu, L. Fan, J. Chen, X. Xing, J. L. Jones, *Appl. Phys. Lett.* **2014**, *104*, 0.

[146] J. C. C. Fan, *Sol. Cells* **1986**, *17*, 309.

[147] C. Elissalde, J. Ravez, *J. Mater. Chem.* **2001**, *11*, 1957.

[148] C. Stock, L. Van Eijck, P. Fouquet, M. Maccarini, P. M. Gehring, G. Xu, H. Luo, X. Zhao, J.-F. Li, D. Viehland, *Phys. Rev. B* **2010**, *81*, 144127.

[149] M. Algueró, R. Jiménez, H. Amorín, E. Vila, A. Castro, *Appl. Phys. Lett.* **2011**, *98*, 202904.

[150] F. Li, S. Zhang, Z. Xu, L.-Q. Chen, *Adv. Funct. Mater.* **2017**, *27*, 1700310.

[151] F. Li, S. Zhang, T. Yang, Z. Xu, N. Zhang, G. Liu, J. Wang, J. Wang, Z. Cheng, Z.-G. Ye, J. Luo, T. R. Shrout, L.-Q. Chen, *Nat. Commun.* **2016**, *7*, 13807.

[152] C. Ang, Z. Yu, L. E. Cross, *Phys. Rev. B* **2000**, *62*, 228.

[153] D. M. Smyth, *Prog. Solid State Chem.* **1984**, *15*, 145.

[154] Y. Q. Lin, X. M. Chen, *Appl. Phys. Lett.* **2010**, *96*, 142902.

[155] D. D. Khalyavin, J. Han, A. M. . Senos, P. Q. Mantas, *J. Mater. Res.* **2003**, *18*, 2600.

[156] L. Murawski, R. J. Barczyński, D. Samatowicz, O. Gzowski, *J. Alloys Compd.* **1994**, *211–212*, 344.

[157] X. P. Wang, Q. F. Fang, *Phys. Rev. B* **2002**, *65*, 064304.

[158] E. Iguchi, N. Kubota, T. Nakamori, N. Yamamoto, K. J. Lee, *Phys. Rev. B* **1991**, *43*, 8646.

[159] I. G. Austin, N. F. Mott, *Adv. Phys.* **1969**, *18*, 41.

[160] G. K. Knopf, K. Uchino, *Light Driven Micromachines*, CRC Press, Boca Raton, **2018**.

[161] K. Takagi, S. Kikuchi, J. Li, H. Okamura, R. Watanabe, A. Kawasaki, *J. Am. Ceram. Soc.* **2004**, *87*, 1477.

[162] B. Kundys, M. Viret, C. Meny, V. Da Costa, D. Colson, B. Doudin, *Phys. Rev. B* **2012**, *85*, 092301.

[163] M. V. Raymond, D. M. Smyth, *Integr. Ferroelectr.* **1994**, *4*, 145.

[164] H. J. Fan, M. H. Kuok, S. C. Ng, **2003**, *2262*, DOI 10.1063/1.1433183.

[165] P. V. Balachandran, J. M. Rondinelli, *Nat. Commun.* **2015**, *6*, 1.

[166] B. Ramachandran, A. Dixit, R. Naik, G. Lawes, M. S. R. Rao, *Phys. Rev. B* **2010**, *82*, 012102.

[167] G. Catalan, J. F. Scott, *Adv. Mater.* **2009**, *21*, 2463.

[168] J. H. Jung, M. Matsubara, T. Arima, J. P. He, Y. Kaneko, Y. Tokura, *Phys. Rev. Lett.* **2004**, *93*, 037403.

[169] Y. Ogawa, Y. Kaneko, J. P. He, X. Z. Yu, T. Arima, Y. Tokura, *Phys. Rev. Lett.* **2004**, *92*, 047401.

[170] D. M. Stein, I. Grinberg, A. M. Rappe, P. K. Davies, *J. Appl. Phys.* **2011**, *110*, 074110.

[171] D. M. Stein, P. K. Davies, *Appl. Phys. Lett.* **2011**, *99*, 182907.

[172] D. Lee, S. H. Baek, T. H. Kim, J.-G. Yoon, C. M. Folkman, C. B. Eom, T. W. Noh, *Phys. Rev. B* **2011**, *84*, 125305.

[173] L. Pintilie, M. Alexe, *J. Appl. Phys.* **2005**, *98*, 124103.